Lawrence Berkeley National Laboratory
Recent Work

Title
DEGRADATION PHENOMENA IN SOLID ELECTROLYTES

Permalink
https://escholarship.org/uc/item/8580j40s

Author
Hitchcock, D.C.

Publication Date
1984-11-01

eScholarship.org Powered by the California Digital Library
University of California

LBL-18710

Lawrence Berkeley Laboratory
UNIVERSITY OF CALIFORNIA

Materials & Molecular Research Division

RECEIVED
LAWRENCE
BERKELEY LABORATORY
FEB 11 1985
LIBRARY AND
DOCUMENTS SECTION

DEGRADATION PHENOMENA IN SOLID ELECTROLYTES

D.C. Hitchcock
(Ph.D. Thesis)

November 1984

TWO-WEEK LOAN COPY
This is a Library Circulating Copy
which may be borrowed for two weeks.

Prepared for the U.S. Department of Energy under Contract DE-AC03-76SF00098

LBL-18710

DISCLAIMER

This document was prepared as an account of work sponsored by the United States Government. While this document is believed to contain correct information, neither the United States Government nor any agency thereof, nor the Regents of the University of California, nor any of their employees, makes any warranty, express or implied, or assumes any legal responsibility for the accuracy, completeness, or usefulness of any information, apparatus, product, or process disclosed, or represents that its use would not infringe privately owned rights. Reference herein to any specific commercial product, process, or service by its trade name, trademark, manufacturer, or otherwise, does not necessarily constitute or imply its endorsement, recommendation, or favoring by the United States Government or any agency thereof, or the Regents of the University of California. The views and opinions of authors expressed herein do not necessarily state or reflect those of the United States Government or any agency thereof or the Regents of the University of California.

LBL-18710

DEGRADATION PHENOMENA IN SOLID ELECTROLYTES

David Charles Hitchcock

Materials and Molecular Research Division
Materials Science and Mineral Engineering
Lawrence Berkeley Laboratory
University of California
Berkeley, California 94720

This work was supported by the U.S. Department of Energy
under Contract No. DE-AC03-76SF00098.

TABLE OF CONTENTS

DEGRADATION PHENOMENA IN SOLID ELECTROLYTES

David Charles Hitchcock

Materials and Molecular Research Division
Materials Science and Mineral Engineering
Lawrence Berkeley Laboratory
University of California
Berkeley, California 94720

ABSTRACT

The critical current density above which degradation occurs in beta"-alumina has been determined by means of acoustic emissions tests on sodium/sodium cells. Cells were tested by passing a current which increased linearly with time, as the stress or strain is increased in mechanical testing. The critical current density was found to depend on the rate of increase of the current density, indicating that some type of time dependent degradation is occurring.

Microstructural investigation of used electrolytes showed some dissolution of electrolyte from inside cracks, and some used electrolytes had a degraded layer on the sodium exit surface, again indicating some type of time dependent attack.

The degradation is attributed to mechanical cracking due to Poiseuille pressure as sodium flows out of surface flaws during charging at high current density. At low current density, long time chemical attack due to changes in the composition of the sodium electrode becomes important. Crack velocity as a function of crack length and current density is estimated for this stress corrosion.

1. INTRODUCTION

1.1 The Sodium/Sulfur Battery

Consumption of electricity varies over the course of the day, being highest during the afternoon, and lowest at night. Also, power consumption is less on weekends and higher during the summer when air conditioners are in use.

The constant portion of the power produced by an electric utility is the base load, and it is usually supplied by nuclear power plants, or by large coal fired plants. The capital cost of a coal fired power plant was about $1200/kilowatt in 1976, and the efficiency of such a plant is about 38% (Bi 76). However, this efficiency can only be achieved if the plant is operated steadily at its designed output. If the plant is started and stopped frequently to meet variations in the demand for electric power, the life is reduced and maintenance costs are increased.

In order to reduce capital costs and to meet variations in the load, gas turbines that can burn oil or natural gas are used at peak power demand. These units are small and can be started and stopped in about a minute, compared to about two hours for a steam plant, and their capital cost is low, $125/kilowatt in 1976, but the efficiency is only 24% (Bi 76). In order to save fuel, and to substitute coal, inexpensive and abundant in the United States, for oil which must be imported from politically unstable areas, it would be desirable to generate more electricity with nuclear or coal fired plants, and to store the excess produced during the night for use during the day.

Use of renewable resources, such as wind or solar power, for generation of energy would also create a need for energy storage systems. The amount of wind-generated electricity purchased by Pacific Gas and Electric Company varied from 0.49 million kilowatt-hours in December 1983 to 7 million kilowatt-hours in April 1984 due to variations in the wind (Fl 84).

Pumped hydro storage, in which water is pumped into a high reservoir when demand for electricity is low, and then used to turn a turbine and generate electricity when demand is high, is already in use, but there is a lack of suitable reservoirs or sites for reservoirs, so little increase in pumped hydro storage is possible (Bi 76).

Improved batteries would be desirable for load levelling because they can be produced in modules of convenient size, switched on and off rapidly, and operated at powers lower than their designed power without sacrificing efficiency (Bi 76).

Another application for high energy density batteries would be electric vehicles. Electricity generated from coal or nuclear energy could be substituted for oil now burned in internal combustion engine vehicles, and air pollution and noise in urban areas could be reduced. Long Island Lighting Company operated electric vehicles for 2.4 cents per mile compared to 6 cents per mile for gasoline powered vehicles, but for long distances or high speeds the necessary weight of batteries is prohibitive (Wa 79). Lighter batteries must be developed before electric vehicles can find widespread use.

One of several high energy density batteries under investigation is the sodium/sulfur battery, first proposed by Weber and Kummer in 1967

(We 67). It has a specific energy of 130 watt-hours/kg and a power density of 110 watts/kg, compared to 40 watt-hours/kg and 70 watts/kg for lead-acid batteries (Fi 81). Sodium/sulfur cells consist of a molten sodium negative electrode separated from a molten sodium polysulfide positive electrode by a tube of solid electrolyte, which must conduct sodium ions but not electrons. Potential electrolyte materials are beta-alumina and beta"-alumina, nasicon, a ceramic of composition $Na_{1+x}Zr_2Si_xP_{3-x}O_{12}$, and sodium ion conducting glass. The electrolyte is usually in the form of a tube, with one electrode inside the tube and the other on the outside. Most cells have the sodium inside the tube, to allow more volume for the sulfide and thus a higher energy density, but in some cases the sulfide is put in the tube because it attacks most metals, which would be useful as materials for the container, much more than sodium. When the sulfide is inside the tube it need not contact the container, so this corrosion problem is avoided.

Application of sodium/sulfur batteries is currently limited by reliability. Causes of failure include corrosion or cracking of the seals between the electrolyte and the container, polarization in the polysulfide positive electrode, and degradation of the electrolyte.

The stresses in the seals can be minimized by using the proper geometry (Tr 81).

Sodium polysulfide is not an electronic conductor, so either graphite or some metal must be used as a current collector in the polysulfide electrode. Most electronic conductors are subject to corrosion by the polysulfide, but graphite felt was found to be suitable (Fa 73).

All the potential electrolytes are subject to degradation in sodium/sulfur batteries. Nasicon lacks sufficient chemical stability when exposed to molten sodium (Ca 82). Glasses can be readily formed into fine capillary tubes, and cells of low internal resistance can be constructed, but the lifetime of the cells is often short, and the failure mechanisms are not well understood (Le 80). The best candidates for the solid electrolyte are beta-alumina and beta"-alumina. Beta" is usually preferred because of its higher conductivity, but it is sometimes claimed that beta is more resistant to degradation although the reasons are not clear. The behavior of these two materials is in many ways similar, and they are both subject to degradation by the reactants in sodium/sulfur cells. The degradation by sodium is more severe, and has been studied much more, but as the lifetime of cells has improved sulfur side degradation has become more noticeable in used electrolyte from the cells. Sulfur side corrosion is therefore currently being studied at this laboratory (Li 84). The remainder of this thesis will deal with the degradation occurring at the beta"-alumina/sodium interface, and with the properties of beta"-alumina and sodium that are relevant to this degradation. Much research has been done on beta"-alumina, and the in remainder of the introduction some of the results from the literature will be summarized.

1.2 Crystal Structure of Beta"-Alumina Solid Electrolyte

Sodium beta-alumina was produced unintentionally by the Norton company by fusing Bayer process alumina, which contained soda. It was thought to be a polytype of alumina (Ra 16) until Bragg et al. proposed a structure containing half the correct amount of sodium, because this

was the amount detected by a chemical analysis, and suggested the ideal formula $NaAl_{11}O_{17}$ (Br 31). Comparison of the actual to the x-ray density confirmed this formula (Be 36), and attempts to produce beta alumina from higher purity alumina failed, while improved analytic techniques detected about 90% of the soda of the ideal formula (Ri 36). Ridgway et al. also made potassium beta-alumina by melting alumina with potassium oxide (Ri 36), and Beevers and Ross determined that sodium and potassium beta-aluminas were isomorphous (Be 37).

Sodium beta"-alumina was produced by solid state reactions at about 1050°C by Thery and Briancon (Th 62) and was given the formula $NaAl_5O_8$. It had been reported, and the unit cell determined, by Yamaguchi in 1943 in the Japanese literature, and the structure was determined by Yamaguchi and Suzuki (Ya 68). Beta" electrolytes are normally made with a divalent or monovalent ion substituted for some of the aluminum, and $Na_2O \cdot MgO \cdot 5Al_2O_3$ was determined to have the same structure as pure beta"-alumina (Be 69).

The crystal structures of beta and beta" alumina are both made up of alternating layers of two types, "spinel blocks" and "conduction planes," Figure 1.1. Each spinel block contains four cubic close packed layers of oxygen ions, with aluminum ions arranged on both the octahedral and the tetrahedral cation sites of spinel. Between the spinel blocks, the conduction planes have a low density of oxygen ions bonding the adjacent spinel blocks together and mobile sodium ions. In beta-alumina, the conduction planes are mirror planes, and there are two spinel blocks and two conduction planes to a unit cell. The structure is hexagonal, with the space group $P6_3/mmc$, and the lattice parameters

are a = 5.594 angstroms, c = 22.53 angstroms (Pe 71). The spinel blocks in beta" are related by a threefold screw axis, and the sodium ion positions are slightly out of the conduction planes. The space group is $R\bar{3}m$, and the lattice parameters are a = 5.614 angstroms, c = 33.85 angstroms for a crystal of composition $Na_2O \cdot MgO \cdot 5Al_2O_3$ (Be 69).

1.3 Defects and Electrical Conductivity in Beta- and Beta"- Alumina

A variety of point defects in beta and beta"-alumina influence the ionic and electronic conductivity. Grain boundaries also influence the electrical behavior.

1.3.1 Point Defects

The phase diagram Figure 1.2 shows that beta and beta"-alumina exist over a range of compositions from about $Na_2O 5.3Al_2O_3$ to $Na_2O 8.5Al_2O_3$, while the ideal formulae are $Na_2O 11Al_2O_3$ for beta-alumina and $Na_2O 5Al_2O_3$ for beta"-alumina. Thus beta-alumina exists with a large excess of sodium, and beta" with less than the ideal sodium concentration, and a large density of defects must be present to compensate.

Figure 1.3 shows the conduction plane of a unit cell of beta-alumina, containing a column oxygen and various sites which can be occupied by the mobile sodium ions, the Beevers-Ross (BR), anti-Beevers-Ross (aBR), and mid-oxygen, (mO). In a neutron diffraction study by Roth et al., defects consisting of an oxygen interstitial in the conduction plane, with two extra sodiums to preserve electroneutrality, and aluminum ions above and below the oxygen interstitial shifted toward the oxygen onto interstitial sites, leaving aluminum vacancies in the spinel block, were detected. Figure 1.4 is a side view of such a defect, known

as a "Roth defect," and the arrangement of ions in the conduction plane around such a defect is shown in Figure 1.3, where two BR sites are vacant, and there are four sodiums on or near mO sites close to the oxygen interstitial. At 350°C, 59% of the sodium ions were in BR sites, 36% in mO, and 5% in aBR (Ro 76). Calculation of potential energy of ions in beta-alumina shows that "Roth defects" can exist, and that the potential of a sodium ion near such a defect would vary little with position, so that the sodium ions would be mobile (Wa 80). The diffusion mechanism in beta alumina is probably hopping of individual ions, and the difficult portion of an ion's hopping from one BR site to the next is passing through the mO site, where it must squeeze between oxygen ions above and below the site (Ku 72).

An x-ray diffraction and diffuse scattering study of magnesium-stabilized beta"-alumina by Boilot et al. showed that the formula could be written $Na_{1+y}Mg_yAl_{11-y}O_{17}$, so the variation in sodium concentration could be attributed solely to the substitution of Mg^{2+} for Al^{3+} in the spinel blocks. In the $R\bar{3}m$ space group of beta"-alumina, the BR and aBR sites are equivalent, but for simplicity the nomenclature BR and aBR will be retained. There is a superlattice due to local ordering of the distribution of sodium on a fraction of the total sites in the conduction plane, as shown in Figure 1.5, with sodium ions missing from one third of the aBR sites, and the sodiums on the BR sites shifted onto the mO sites, toward the vacant aBR sites. The coherence length for this order is 70 angstroms at room temperature. In other regions, the vacancies would be on the BR sites, and the sodiums from the aBR sites would be shifted onto the mO sites surrounding the vacancies. Intensity data

showed that about 39% of the sodium was on BR and aBR sites, with 61% on mO sites. This is in good agreement with the model, which predicts 40% on BR and aBR sites, and 60% on mO(Bo 80). The activation energy for the conduction by the motion of a single sodium vacancy, obtained from potential energy calculations, is 0.02 eV, which is about an order of magnitude lower than the activation energy from an Arrhenius plot (Wa 81). This discrepancy is attributed to ordering of interacting vacancies and to interactions with the magnesium ions used to stabilize the beta" phase. Thus the transport mechanism appears to be collective motion of vacancies.

When beta- and beta"-alumina are exposed to molten sodium, they are discolored due to the introduction of oxygen vacancies. The darkening propagates as a layer by diffusion, and the diffusion coefficient increases as the vacancy concentration increases (De 82a). From measurements of the darkening rate for beta" specimens with different grain sizes, the diffusion was found to occur mainly along the grain boundaries, and the diffusion coefficients in the lattice, D_L, and the grain boundary, D_B, are:

$$D_L < 1 \times 10^{-10} \text{ cm}^2\text{sec}^{-1}$$

$$D_B = 9.8 \times 10^{-7} \text{ cm}^2\text{sec}^{-1}$$

with a grain boundary thickness of 10 angstroms (De 82a).

The electronic conductivity should depend on both oxygen partial pressure and temperature, and for silver beta alumina the electronic conductivity increases as the oxygen partial pressure is reduced from 0.2 atm to 1.2×10^{-15} atm, but when pressure is further reduced to 8.1

$\times 10^{-20}$ atm no further change in conductivity is observed (Wh 71). In this case, the oxygen partial pressure at one electrode was varied, while the partial pressure at the other electrode was held at a low value by means of a large silver activity. Part of the observed electronic conductivity might actually be due to oxygen migration, either of oxygen vacancies or of interstitial oxygen in the conduction plane.

The electronic conductivity of sodium beta-alumina has been measured in a cells of the type.

Porous metal, sodium vapor/beta"-alumina/sodium

by making the sodium the negative electrode and passing a current larger than the number of sodium atoms available from the vapor phase at the positive electrode. Then the excess current is due to species other than sodium, such as oxygen ions, electrons, and holes. This type of measurement was proposed by Wagner (Wa 57), High temperature measurements made by Weber follow a straight line for log conductivity vs. 1/T at high temperature, but a deviation from linearity below 450°C was attributed to a failure of the electrolyte to reach equilibrium. Measurements at lower temperature made by Takikawa et al. (Ta 82) on beta-alumina were about five times higher than Weber's results, with an electronic conductivity of 6×10^{-6} $(ohm.cm)^{-1}$ at 340°C, and activation energy of 1.0 eV. There do not appear to be any data on the electronic conductivity of beta"-alumina in the literature.

1.3.2 Grain Boundaries

Grains of beta- and beta"-alumina tend to grow with facets parallel to the basal plane, and because sodium ions cannot move perpendicular to

the basal plane, such grain boundaries block the flow of current. Degradation occurs above some critical current density (Te 75), and such blocking grain boundaries could create high local current densities when the average current density is low.

Low angle tilt boundaries within grains of beta alumina which could create local high current densities have also been observed (De 76). In a grain boundary such as that of Figure 1.6, where the conduction planes of the two subgrains join the boundary, the ions moving along the conduction planes all flow into the grain boundary, creating a high local current density.

1.4 Phase Equilibria and Thermodynamics

The phase diagram of Figure 1.2, of the alumina rich portion of the soda-alumina system, after Le Cars et al. (Le 72), makes use of cooling curve data from Rolin and Thanh (Ro 65) for the liquidus and solidus lines. The compositional range of beta and of beta", which is metastable in the system soda-alumina, is $5.33Al_2O_3 \cdot Na_2O$ to $8.5Al_2O_3 \cdot Na_2O$. Determination of the stability fields of the various solid phases is complicated, as the kinetics of the formation of beta and beta" from solid oxides or melts are very different, and solid state phase transformations go slowly (De 69). It is difficult to form beta below 1650°C, and beta" can be formed below 1600°C, with both phases existing over a range of compositions (De 69). Cooling of melts with the composition of the $NaAlO_2$-Al_2O_3 eutectic produced more beta" at higher cooling rates than at lower cooling rates, where beta was favored. Also, when quenched specimens were annealed at 1530°C and 1400°C, the beta" content dropped with time. This was taken as proof that beta" was metastable, although

the transformation to beta was slow at 1400°C, and beta" can exist indefinitely at room temperature (Ho 83). However, practical electrolytes are ternary systems, containing a small amount of a cation of lower valence substituted for aluminum, in order to increase the sodium ion concentration, and thus the conductivity. The beta" phase is stable in the ternary system soda-alumina-magnesia (Ku 72), and is probably also thermodynamically stable in soda-alumina-lithia and several other systems.

If beta"-alumina is to serve as an electrolyte, it must be stable in the presence of sodium sulfides and sodium. Phase diagrams of these systems are not available, but the literature contains some information on the stability of beta"- and beta-alumina in various aggressive environments.

The free energy of formation of beta-alumina from $NaAlO_2$ and Al_2O_3 was determined electrochemically at temperatures from 1000 to 1600°C (Ku 72). These results were extrapolated to lower temperature, where the kinetics of the reaction would have been too slow to permit measurement, and along with existing data from the JANAF Thermochemical Tables, the free energy for the reaction:

$$21/50\ Na + 1/25\ Na_2O{\cdot}8Al_2O_3 = 1/2\ NaAlO_2 + 7/50\ Al$$

was calculated to be negative by a few kcal below 915°C, but the reaction was not observed for samples of beta"-alumina in contact with molten sodium for several weeks at 400°C (We 74).

Pitting has been observed on the sodium surface of beta and beta" electrolyte which has been cycled in sodium/sodium or sodium/sulfur

cells for about 200 Ah/cm^2, and initially sharp, angular grains appear to be smooth and rounded after 100 Ah/cm^2 (Iw 80).

X-ray diffraction intensities for crystals of beta-alumina from the center of a block used as a glass tank refractory indicated that only 82% of the oxygen sites in the conduction planes were occupied, and there had also been some soda loss.

1.5 Impurities

Beta"-alumina can be contaminated with impurities from the raw materials used to make it, or a variety of impurities from the environment can enter the conduction plane. These impurities can reduce the electrical conductivity and can cause degradation of the electrolyte.

Beta"-alumina made from impure aluminas, containing more than 100 ppm of calcium were found to undergo degradation during electrolysis in sodium/sodium cells at current densities greater than 1 A/cm^2, while electrolytes made from aluminas containing 52 ppm of calcium survived such a test (Mi 79). The addition of about 1 wt.% of calcia to beta-alumina changed the fracture from transgranular to intergranular, lowering the strength (Un 77). On the exposed grain boundaries on the fracture surface of the calcia-containing electrolyte, the calcia concentration was about ten times the bulk concentration. Second phases at the grain boundaries of calcia containing beta alumina were identified as $CaO \cdot 6Al_2O_3$ and 3 $CaO \cdot 2Na_2O \cdot 5Al_2O_3$ (Bu 79). The presence of the calcia was found to promote exaggerated grain growth, probably due to transport through the liquid, and the resistivity increased exponentially as the calcia content increased, due to the high resistivity of the grain boun-

dary phases. Addition of silica to beta-alumina produced a glassy phase which was found mostly at triple points, and occasionally in grain boundaries, and resistivity again increased exponentially with increasing silica content (Hs 78).

Water cannot be present in a sodium containing system, as it will react quickly with the sodium, but beta- or beta"-alumina will hydrate when exposed to the atmosphere. When sintered polycrystalline beta" alumina was exposed to the atmosphere for a few weeks, the "c" lattice parameter expanded from 3.352 nm to 3.366 nm to a depth of about 5 micrometers. Repolishing to remove the surface layer or heating to 1000°C restored the lattice parameter to its original value, and storage in vacuum prevented any change (He 82). Moisture reduces the intergranular conductivity and increases the activation energy (Ga 81). Heating of hydrated electrolyte caused a weight loss of about 2%, and both water vapor and carbon dioxide were evolved (Du 81). It is likely that water enters the conduction plane as hydronium, and the sodium then forms sodium hydroxide on the surface which can combine with carbon dioxide from the air (De 77). Heating would then drive off the carbon dioxide, while the hydroxide and hydronium ions would form water, which could also evaporate, and the sodium ions would return to the conduction planes. Moisture produces a time-dependent, non-ohmic polarization at the beta alumina/propylene carbonate interface. The reduction in the polarization that was observed as current was passed was attributed to the flow of hydronium ions out of the lattice along with the sodium ions (Fa 76). Both the change in the "c" lattice parameter, which would cause stress, and the polarization at the interface could contribute to degra-

dation of the ceramic during electrolysis.

Toropov and Stukalova noted that the sodium ions in beta-alumina could be replaced with various other alkali or alkaline earth ions by immersing the beta-alumina crystals in molten salts of the desired cations (To 39, To 40). During operation of a sodium/sulfur battery, impurities in the sodium or the sodium polysulfide can enter the electrolyte in a similar manner. Such impurities often come from corrosion of the container or seals. Lazennec et al. observed a rise in resistance, followed by failure of the electrolyte, when potassium and silicon from the glass parts of the cell entered the electrolyte. The rise in resistance was equally rapid for cells through which current was passed as for cells through which no current was passed. Transition metals, which might come from an alloy container, do not enter the lattice. Five weight per cent of iron, nickel, cobalt, or chromium dissolved in the polysulfide had no effect on cells (Li 84). Potassium and calcium are common impurities in sodium, or could be leached from glass parts of a cell, and both can enter the beta"-alumina lattice. Yasui and Hattori found that calcium greatly decreases the grain boundary conductivity, and potassium slightly decreases the grain boundary conductivity, but noted no effect on the bulk conductivity from either ion (Ya 80). Ni et al. found that the replacement of as little as a tenth of the sodium in a single crystal of beta"-alumina with calcium decreased the conductivity by two orders of magnitude at 300°C, and suggested that in the polycrystals tested by Yasui and Hattori the calcium might have segregated at the grain boundaries (Ni 81). Table 1.1 shows the effects of calcium and potassium substitution on the lattice parameters of

polycrystalline beta"-alumina of the same type used for this thesis, and on single crystals. The polycrystalline material was crushed and passed through a 200 mesh before determination of the lattice parameters by x-ray diffraction (He 83). Calcium slightly decreases the "c" lattice parameter, while potassium increases the "c" lattice parameter more substantially. The effects are similar in polycrystals and single crystals. Both the decrease in ionic conductivity and the change in lattice parameter, which would cause stress in a polycrystalline electrolyte, can contribute to degradation of the electrolyte. The decrease in conductivity promotes mode II degradation, in which sodium metal is formed inside the electrolyte (De 82b), while the stress will promote the propagation of mode I cracks.

1.6 Fabrication

Beta- and beta"-alumina can be fabricated by a variety of processes. A good electrolyte must generally be relatively pure, contain no other phases than beta- and beta"-alumina, and have high density and good mechanical strength, with moderate grain size.

About one weight per cent of additives such as lithia and magnesia is used in practical electrolytes to increase the conductivity, and it is necessary to achieve a uniform distribution of these minor components in order to produce a homogeneous ceramic. Simply milling the proper proportions of oxides together to form beta" yielded, after sintering, a ceramic containing beta- and beta"-alumina and $NaAlO_2$ (Li 79). Single phase lithia-stabilized beta"-alumina could be produced by the "zeta process" in which lithia and alumina are combined and calcined to form $Li_2O{\cdot}5Al_2O_3$, zeta lithium aluminate, while the soda and the remaining

alumina are also combined and calcined. Then the lithium containing component is a larger fraction of the final composition, so that when the two powders are combined it is easier to achieve a uniform distribution of all the constituents (Mi 79). With a highly dispersed alumina raw material, single phase beta"-alumina was formed, but with less active alumina beta-alumina and $NaAlO_2$ were also present (Kv 81). In some cases these multiphase materials could be converted to single phase beta" alumina with good properties by a post-sintering heat treatment, but in other cases the transformation to beta" was slower, and exaggerated grain growth occurred before the transformation was complete.

Such a heat treatment can also increase the conductivity of the electrolyte (Wh 74), because grain boundaries in a fine grain size material make a substantial contribution to the resistivity, but a large grain size electrolyte is more subject to electrolytic degradation than is a small grain size material(Bu 83). The ionic conductivity depends mainly on the average grain size, while electrolytic degradation can occur at a single large grain at the surface of the electrolyte, so a better compromise between conductivity and degradation resistance might be achieved if material with a uniform, moderate grain size could be produced. The microstructure normally observed is a few very large grains in a matrix of small grains, as in Figure 2.1. Addition of tetragonal zirconia to beta" alumina not only increases the fracture toughness, but also prevents grain growth (Gr 84), yielding materials with high strength, but somewhat higher resistivity than pure beta" alumina.

1.7 Properties of Sodium

The sodium electrode is likely to contain dissolved oxygen, so the oxygen partial pressure in the electrode will be established by the sodium-sodium oxide equilibrium. At 300°C, the oxygen pressure is about 10^{-62} atm. The solubility of oxygen in sodium follows the equation:

$$\log(\text{wt \% sodium monoxide oxygen} \times 10^3) = -0.0535 + 0.00351T$$

where T is the temperature in degrees centigrade (Wi 59), giving about 100 ppm of oxygen at 300°C. The sodium is likely to be saturated with oxygen, and when a cell is discharged, any oxygen in the sodium would be left at the interface with the electrolyte as the sodium metal is converted to ions which are transported through the electrolyte. Sodium oxide could precipitate at the interface and might cause poor wetting or otherwise interfere with the operation of the cell.

Wetting of the electrolyte by the liquid sodium electrode is necessary to minimize the resistance of the cell, and perhaps to avoid high localized current densities at the edge of unwetted regions which may cause degradation (Vi 80). A sessile drop study of the wetting of polycrystalline beta"-alumina by molten sodium showed that the contact angle was lower at low temperature and could be substantially lowered by baking cells in vacuum to remove moisture. Cells exposed to a moist atmosphere before testing had poor wetting. When the temperature is lowered, the contact angle does not increase, so the wetting is irreversible. When cells were baked to assure good wetting, they survived the passage of current while cells that had not been baked failed quickly (Vi 82).

2. EXPERIMENTAL

2.1 Materials

Beta"-alumina disks were prepared by Ceramatec, Inc., Salt Lake City, Utah by the process described by Miller et al. for the manufacture of tubes (Mi 79), except that the disks were formed by cold pressing. The microstructure of electrolyte polished to a one micron diamond finish, and then thermally etched for 15 minutes at 1450°C, Figure 2.1, is bimodal, with a few large, tabular grains in a matrix of fine grains. Most experiments were performed on the fine grain size material, Figure 2.1A, with a grain size of about one micrometer for the fine grain fraction, and the grain size of the large grains was about 10 microns. A few tests used material which had been heat treated to allow grain growth, with the large grains up to 300 micrometers in length, Figure 2.1B. Figure 2.2 shows the surface of a sintered disc. The main irregularities noted in the surface were large pores. A large processing flaw, probably due to a hair in the green compact, is visible in the surface of a disc in Figure 2.3A, and in Figure 2.3B the hair extends into the disc. Surface pores, flaws due to foreign matter in the green compact, and the large grains noted in Figure 2.1 might serve as sites for the initiation of degradation. The chemical composition given by the manufacturer was: 8.85 wt% Na_2O; 0.75 wt% Li_2O; balance Al_2O_3. The electrolytes were stored in an oxygen and water free(<1 ppm) glove box (Vacuum Atmospheres Company, Los Angeles, California; HE 93-2 Dry Lab with MO 40-1 inert gas purifier).

The sodium was S-135, Certified ACS from Fisher Scientific Company, Santa Clara, California.

Large single crystals of sodium-beta alumina were obtained from Union Carbide, Linde Division, San Diego, California. These crystals tended to cleave along the basal planes. Most of the spontaneous cleavage cracks could be healed by annealing the crystals at 1600°C in air for 2 hours, packed in coarse sodium-beta alumina powder to avoid soda loss.

2.2. Microstructural Investigation of Used Electrolytes

Used electrolytes from sodium/sodium cells tested under various conditions, and electrolytes from sodium/sodium and sodium/sulfur cells tested at other laboratories were investigated by means of optical and scanning electron microscopy.

Specimens for the optical microscope were sectioned with a diamond saw, ground with silicon carbide abrasive, and polished to a one micron diamond finish. They were then stained in a saturated solution of silver nitrate at about 80°C for about 20 minutes. Staining the electrolytes in this manner deposits metallic silver in degraded regions and cracks, rendering than dark against a light background when viewed with crossed polarizers (De 80).

For the SEM, the specimens were not stained, but in some cases were thermally etched at 1450°C to reveal the microstructure. In order to study weak, degraded surface layers, some specimens were sectioned and mounted carefully to minimize the amount of grinding needed, then ground gently by hand on silicon carbide paper, and polished with one micron diamond paste on a tin plate. With this procedure flat, well polished specimens with good edge retention could be prepared.

2.3. Sodium/Sodium Cells

Sodium/sodium cells were made from Al_2O_3 tubes, (AD998, Coors Porcelain Co., Golden, Colo.), joined to disks of beta"-alumina with glass seals (SBW glass, Schott America, New York, N.Y.). Using the test rig shown in Figure 2.4, the cells were heated to 350°C for 30 minutes to promote wetting of the beta"-alumina by the Na, and then the furnace was adjusted to the desired operating temperature. A Mo rod was inserted into the cell, making contact with the electrolyte, and Na was plated onto it to form the working electrode. Forming the electrode in this manner insured good wetting, and most impurities are unable to pass through the electrolyte, so contamination was prevented. The plating process was carried out at low current density and was monitored with the acoustic emission system as described below in order to avoid degradation of the electrolyte.

2.4. Acoustic Emissions Detection

When electrolytes fail by the initiation and propagation of cracks, stress waves are generated as a result of stored energy release. These stress waves or acoustic emissions can be monitored by a sensitive transducer, and various parameters of the wave form, such as peak amplitude, rise time, and duration of the acoustic event can be recorded.

Acoustic emission tests were performed on cells of the type shown in Figure 2.4. An AET 5000 computerized acoustic emission system, manufactured by Acoustic Emission Technology, Sacramento, California, was used to detect the acoustic emissions and to discriminate between signals arising from cracking of the electrolyte and those from electri-

cal noise or mechanical vibrations. The shapes of the signals, as indicated by their rise time, event duration, and peak amplitude, were used to determine the source of the signals. This was necessary because the acoustic emissions that accompanied the onset of breakdown were not very pronounced. Also, measurements generally had to be made at night or on week ends, when the background noise from the power lines was lower. Cells were tested with a current ramp generated by a Priceton Applied Research model 175 programmer and model 371 galvanostat, analogous to an increasing stress in a mechanical test.

Another study of electrolyte degradation by means of acoustic emissions was performed by Worrell and Redfern (Wo 78).

2.5. Fracture Toughness of Single Crystals and Polycrystals

Beta- and beta"-alumina cleave easily on the 00.1 conduction planes. The fracture toughness for cracks on 00.1 planes and perpendicular to these planes was measured for single crystals of sodium beta-alumina. The microhardness indenter fracture toughness method (Ev 76, An 81, Ma 82) had to be used since only small crystals were available. Single crystals of beta"-alumina available to date are too small even for this method. Polycrystalline beta"-alumina was tested for comparison.

A single crystal of beta-alumina and polycrystalline beta"-alumina were heated for 24 h at 900°C in beta-alumina packing powder and were then mechanically polished. Polishing was necessary to enable accurate measurement of the crack length in the polycrystalline specimen after indentation. The prismatic planes of the single crystal could only tolerate minimum preparation since 00.1 cleavage cracks were produced

even by careful sanding. These cracks did not interfere with the measurements since indents could be made on unflawed prismatic plane regions and the resulting cracks could be viewed with transmitted light, so a polished surface was not needed. The specimens were then annealed in packing powder of the appropriate alumina-soda composition for 3 h in air at 1500°C. This treatment healed many cracks in the single crystal. The polycrystals showed considerable thermal etching, but the indent cracks could still be measured with accuracy under oblique illumination in the optical microscope. Indentations were made with a Vickers diamond indenter, with loads between 19.6 and 49.0 N. For indents on the prism planes, one diagonal of the indenter was aligned to within 0.2° with the basal planes of the crystal. This alignment produced a basal-plane crack and a crack normal to the basal plane, for prismatic-plane indents as shown in Figure 2.5. During indentation the surfaces were covered with immersion oil to prevent subcritical crack growth resulting from ambient moisture. After indentation, the oil was removed with acetone and the cracks were measured immediately. The cracks were viewed again several days later, and the basal-plane cracks had grown in some cases to the edge of the crystal, while the cracks normal to the basal plane and in the polycrystalline specimens had not grown.

Knoop indents were also made in the single crystal and used to determine the elastic modulus in the basal plane and perpendicular to the basal plane (Ma 82).

2.6. Charge Transfer Resistance Measurement

A charge transfer resistance which was probably due to an impurity was measured using a sodium/sodium cell with a reference electrode

placed as shown in Figure 2.6 in a small alumina tube sealed to the electrolyte disk. Because Na^+ is the only mobile species, no concentration gradient will exist in beta" alumina. Therefore the only overpotentials present will be the ohmic overpotential due to the resistance of the electrolyte and the surface overpotential.

The cell and a 1 ohm standard resistor were connected in series to a sine wave generator, General Radio type 1311-A. A digital voltmeter, Data Precision 3500, was used to measure the potential of the reference electrode, and it was also used to measure the current by measuring the voltage drop across the resistor. The ratio of reference electrode potential to current was constant for frequencies from 25 to 200 Hz, so the potential for alternating current was assumed to be due only to the bulk resistance, not the interface resistance. Then the sine wave generator was replaced with a galvanostat, Princeton Applied Research model 371, and the reference electrode potential was measured as a function of current for direct current. The surface overpotential was obtained by subtracting the reference electrode potential for an alternating current from that for a direct current of the same magnitude. Then the slope of a plot of potential vs. current gave the charge transfer resistance.

A second measurement of a charge transfer resistance, due to an oxide film on the electrolyte surface, was made on two cells of the type shown in Figure 2.4, one with an electrolyte thickness of 0.274 centimeters, and the other with a thickness of 0.108 centimeter. The area of the electrolyte was approximately 0.77 centimeters squared for both cells. The cells were placed in the sodium at about 105°C, with about one centimeter cubed of sodium inside the tubes. The tubes were heated

to 400°C for thirty minutes to promote wetting of the electrolyte by the molten sodium. The cell was connected to a galvanostat, and the current was linearly swept from 0 mA to 100 mA with the sodium passing into the tube, then to 100 mA in the opposite direction, with the tube emptying, and finally back to 0. The voltage vs. the current was recorded, and the slope of this plot gave the resistance. The temperature was lowered 50 degrees, allowed to stabilize for about 15 minutes, and the resistance was again measured by the same procedure. This process was repeated for temperatures from 400°C to 200°C, The cell was then reheated to 400°C and manganese was added. The resistance of the cell decreased, and after about 30 minutes it stabilized. Then the resistance measurements were again made from 400°C to 200°C in 50 degree intervals. The cell was reheated, vanadium was added, and the resistance dropped slightly. Measurements were again made. The cell was reheated, and titanium was added, and the resistance again dropped slightly. The measurements were performed on two cells of different electrolyte thicknesses. The log of the cell resistance was plotted vs. 1/T.

3. FAILURE ANALYSIS OF CYCLED ELECTROLYTES

Used electrolytes from sodium/sodium and sodium/sulfur cells tested at several laboratories and companies were examined for evidence of degradation. In all the used electrolytes, a darkened layer at the surface in contact with sodium due to chemical reduction of the electrolyte was observed, and in some cases cracks and degraded layers at the sodium surfaces were observed. Specimens were stained in silver nitrate solution to render the degradation visible in the optical microscope (De 80).

3.1. Data on Used Electrolytes

Electrolytes from Brown Boveri sodium/sulfur cells had a composition 8.9 wt% Na_2O, 2.25% MgO, complement Al_2O_3, and had been cycled at 350°C with current densities of 150 mA/cm^2 during discharging and 75 mA/cm^2 during charging.

Two types of electrolyte from sodium/sulfur cells tested by General Electric were examined. The new material, RS-1, has lower resistivity and resistance rise during cycling, and higher projected stability than the older G8 electrolyte.

Electrolytes from the British Railways Research and Development Division, Derby, U.K., from sodium/sulfur cells, had a composition 8.9 wt% Na_2O, 0.7 wt% Li_2O, balance Al_2O_3, and were more than 90% beta", with a small amount of beta-alumina. The tubes were fabricated by isostatic pressing and were sintered in closed crucibles of high thermal capacity in an electric kiln (Ar 80). These cells were subjected to an average current density of 50 mA/cm^2, with current density as high as

100 mA/cm^2 on some discharge cycles. The British Railways cells had the Na electrode outside the electrolyte tube, with the sodium polysulfide electrode inside the tube.

Sodium/sodium cells from Compagnie General d'Electricite (CGE) had been tested for 1,000 hours at 100 mA/cm^2, for a total unidirectional charge passed of 100 Ah/cm^2. The tubes were operated with the inside as the sodium entrance surface and the outside as the sodium exit surface.

Sodium/sodium cells from Brown Boveri were tested with a maximum current density of 0.77 A/cm^2 and a maximum temperature of 400°C, and the reported charge passed is the total for forward and backward operation. After testing the cells were cleaned in ethanol, then water, then baked at 800°C for two hours. This baking removes the oxygen vacancies from the electrolyte, so no darkened layers are visible in these tubes. The silver nitrate still stains cracks in the electrolyte. The composition of the B cells is 8.7 wt% Na_2O, 2.25% MgO, balance Al_2O_3, and Alcoa A-16SG alumina was used. These cells had asymmetric resistances in the later stages of testing. They had been cleaned and re-assembled during testing, and similar cells that had not undergone this cleaning had no asymmetric resistance. The C, D, and E cells had higher MgO contents. Figure 3.1 is a polished and thermally etched specimen of electrolyte v69-F206. The grains are tabular with a large variation in size.

Ford Motor Company sodium/sulfur cells were charged at a current density of 75 mA/cm^2, and discharged at 100 mA/cm^2.

3.2. Observations

A sectioned, polished and stained electrolyte from a CGE sodium/sodium cell, Figure 3.2, shows the three features observed in this study. At both the sodium entrance and sodium exit sides of the cell, a darkened layer at the Na interface is visible.This darkened layer is due to diffusion of oxygen vacancies into the electrolyte during exposure to molten Na, as described in (De 82a) and summarized in section 1.3 of this thesis. No cracking of the electrolyte has been found associated with this chemical darkening, even in the transmission electron microscope (De 82a).

A second feature appearing in most if not all the electrolytes is the more intensely darkened layer at the sodium exit interface. This layer is not as thick as the chemically darkened layer, and after staining it is black in the optical microscope. This blackened layer is only observed after the passage of current.

A mode I crack, which penetrates into the electrolyte from the sodium exit interface, is visible in this specimen. These cracks are filled with sodium, so when they penetrate through the electrolyte they form a short circuit path for electrons and allow the cell to discharge. When the number and size of the cracks becomes large enough to introduce significant electronic conductivity, the useful life of the cell ends. This form of degradation is therefore the most serious for the operation of cells, and it will be described first.

3.2.1. Mode I Cracks

Mode I cracks are typically narrow, and are sometimes called dendrites or filaments. When sodium/sodium cells are operated, sodium is formed by electrolysis on the negative surface of the electrolyte, as it is on the sodium surface of the electrolyte in a sodium/sulfur cell during charging. Sodium will also form in surface flaws, such as cracks and pores. As this sodium flows out of the surface flaws, it produces a Poiseuille pressure. Then if the rate of flow of sodium, which is proportional to the current flowing into the crack, is great enough, the Poiseuille pressure would cause the crack to propagate. This model was first proposed by Armstrong et al. (Ar 74) and has been further developed by many others (Br 80a, Fe 82, Vi 83). The critical current density for propagation of the crack as calculated by Feldman and De Jonghe is:

$$j_{crit} \propto K_{Ic}^4/l \qquad (3.1)$$

where K_{Ic} is the fracture toughness of the electrolyte and l is the crack length.

Mode I cracks appear to follow the path of least resistance through the electrolyte, and in Figure 3.3, a thermally etched section of a degraded specimen from a Brown Boveri sodium/sodium cell the cracking is along grain boundaries and the basal plane of the grains, which is an easy cleavage plane. This is in accord with the mechanical cracking model presented above.

Sometimes, as in Figure 3.2, cracks appear to extend only part way through the electrolyte, but when such specimens from CGE sodium/sodium

cells were ground, polished, and photographed repeatedly, cracks were found to extend on through the electrolyte. The diffuse, upper crack in section 1 of Figure 3.4 appears to only extend about half way through the electrolyte, but in section 4 it goes significantly farther, and may connect to the through crack in the lower portion of the micrographs. The crack on the right in Figure 3.5, from another CGE sodium/sodium cell, clearly extends through the electrolyte, while in the middle of the picture what appears to be the ends of such a crack can be seen, and the middle of the crack is presumably not in the plane of sectioning. The critical current density is inversely proportional to the crack length in equation (3.1), so once a crack begins to propagate it should rapidly penetrate through the electrolyte. Therefore cracks penetrating only part way through the electrolyte are not expected from the Poiseuille pressure model.

The crack of Figure 3.6, in a specimen from a Brown Boveri sodium/sulfur cell, has a chemically darkened layer around it. This darkened layer is broadest at the sodium side, where mode I cracks originate, and the width decreases as the distance from the sodium side increases. Because the rate of formation of this darkened layer is known, from the thickness of the crack at any point, the age of that part of the crack, and thus the crack growth rate, can be determined. This method of determining crack velocity can only be used inside the electrolyte, away from the darkened layer at the sodium surface, because this darkened layer interferes with measurement of the darkened layer produced by the sodium in the crack. The crack growth rate vs. crack length, shown in Figure 3.7, varies along the length of the crack, and

it is on the order of 10^{-9} m/sec, compared to a predicted velocity for the Poiseuille pressure model of 10^{-5} to 10^{-6} m/sec for a crack length of 10^{-7} m (Br 80a). This observation of a crack velocity much slower than expected, and variations in velocity, could both be explained by slow crack growth. When the crack was advancing through an easy cleavage plane or a weak grain boundary, critical crack growth could occur, so that the crack growth rate would be high, and when the crack reached a grain with its easy cleavage plane perpendicular to the crack, it would proceed more slowly.

In order to investigate further the possibility of slow crack growth in beta"-alumina during electrolysis, crack morphologies were studied. In Figure 3.8, a crack intersects the plane of sectioning of a specimen of CGE electrolyte. In an SEM micrograph of this same crack, Figure 3.9, some but not all parts of the crack have some material missing. It must either have been dissolved in the sodium in the crack, or else weakened by exposure to the sodium so that it crumbled during polishing. The lower end of the crack of Figure 3.9 is shown at a higher magnification in Figure 3.10, and the surfaces appear to be smooth, so that some sort of dissolution may be indicated rather than weakening. Cross sections of cracks in other CGE material reveal greater amounts of material removed from the inside of the cracks. In the SEM micrograph of Figure 3.11A, it is again not very clear whether the material was pulled out during polishing or dissolved away, but a higher magnification of the end of the crack in Figure 3.11B shows some smoothing and rounding of the edges, suggesting that some type of corrosion occurred. Optical and scanning electron micrographs of another crack are shown in Figure

3.12 A and B, respectively, and this crack is shown at higher magnifications in the SEM in Figures 3.13 A and B. There is clearly some sort of chemical or electrochemical corrosion in this specimen, and in the lower part of the crack it appears that some second phase may have been removed. No difference in composition could be found near this crack with x-ray analysis in the SEM.

It seems likely that at high crack velocity mode I cracking is primarily mechanical fracture due to Poiseuille pressure, while at lower velocity some type of stress corrosion becomes important. In order to test this hypothesis, a mode I crack surface was compared to a mechanical fracture surface. Because mode I cracks are usually small, it is difficult to break a specimen of electrolyte at a mode I crack and to distinguish the mode I crack from the surrounding fracture surface. For this experiment, a sodium/sodium cell was constructed and operated in the manner described in section 2.3, except that no sodium was plated onto the molybdenum rod, which formed a point contact with the electrolyte. This allowed a high current density to be passed through the electrolyte in a small spot. The current density was increased until the terminal voltage dropped drastically, accompanied by much acoustic activity. A large crack was thus produced. The electrolyte was left in the molten sodium for several days, so the exposed crack surface was darkened. It was then stained in silver nitrate solution, coloring the surface that had been exposed to Na dark brown. Then the electrolyte was broken, revealing stained surface that had been produced by mode I degradation and unstained surface produced by mechanical fracture. In both Figure 3.14A, the mode I crack, and 3.14B, the mechanical fracture

surface, fracture is largely intergranular or follows the 00.1 conduction planes of the grains, and the surface produced by mode I degradation at high current density does not differ from that produced by mechanical fracture. Thus mode I cracks can propagate by mechanical fracture due to Poiseuille pressure at high current density and high crack velocity, or by stress corrosion at low current density and low crack velocity.

A model based on stress corrosion has been proposed by Richman and Tennenhouse (Ri 75) to explain mode I cracking, but in mechanical strength tests of beta- (Da 79a) and beta"-alumina (Sh 77) in molten sodium, no slow crack growth was found. Because slow crack growth is observed during electrolysis but not during mechanical testing in molten sodium, some sort of electrochemical corrosion is indicated. Possible models are developed in section 6 on slow crack growth.

Not all used electrolytes showed evidence of mode I degradation. Electrolytes in which mode I degradation was not observed were those tested by Ford Motor Company, with a specimen cycled to 592 AH/cm^2 in Figure 3.15 and another specimen cycled to 602 AH/cm^2 in Figure 3.16, and those tested by General Electric shown in Figures 3.36 and 3.37. In both cases, the only effect of cycling on the electrolytes observed on the sodium side was the formation of the darkened layers, visible in Figures 3.15 and 3.16.

3.2.2. Surface Layer

The second important feature observed in Figure 3.2 was a surface layer which appeared black in the optical microscope after staining,

indicating that a large amount of silver had been deposited. An SEM micrograph of this surface layer, Figure 3.17, shows many voids due to pulling out of grains during grinding and polishing. Either cracks formed at the grain boundaries during testing of the cell, or the grain boundaries were weakened so that they cracked during polishing. Careful specimen preparation is necessary to prevent spalling of this layer, and the layer is beginning to spall off in Figure 3.17. The electrolyte of Figure 3.18, from a British Railway sodium/sulfur cell cycled to 539 Ah/cm^2, was ground by hand using much pressure, and then polished automatically on a polishing cloth with diamond paste. It shows much damage, while another specimen from the same tube which was ground carefully by hand, and then polished on a block of tin with one micron diamond paste, Figure 3.19, has good edge retention and shows only a few pull outs even at high magnification. Specimen preparation therefore determines what is observed in the following micrographs, and unless otherwise noted, all the subsequent specimens received the second treatment, being polished by hand on a metal plate with one micron diamond paste. The surface degradation is not entirely an artifact of specimen preparation, because during sawing of specimens from electrolyte tubes, the saw would cut rapidly through the degraded layer, and when it reached material in good condition in the bulk of the electrolyte the saw cut slowly and the sound of the sawing changed.

If specimens were cut on the sodium entrance side of sodium/sodium cells, or on the sulfur side of sodium/sulfur cells first, when all the good material was sawed through the specimen would break, but if the sodium exit or the sodium side was sawed first, the specimens could be

sawed all the way through without breaking. This indicates that the degradation occurs when sodium ions are reduced to sodium metal at the interface, and not when sodium metal is oxidized to from sodium ions. Figure 3.20, a CGE electrolyte polished on a polishing cloth, shows much more extensive degradation at the sodium exit surface than the sodium entrance surface. Figure 3.8, an optical micrograph of a CGE electrolyte, also shows a blackened, degraded layer at the sodium exit side, but not at the sodium entrance side. Figure 3.12, however, shows almost as much degradation on the sodium entrance side as on the sodium exit side, in both optical and SEM micrographs.

The mechanisms by which the degraded layers form are probably the same as those responsible for slow crack growth, and will be developed in section 6 on time dependent degradation. In the remainder of this section, degraded layers in electrolytes tested under various conditions will be examined in order to determine the important factors in the formation of the degraded layers.

In order to study the formation of this degraded layer under controlled conditions, and to determine whether it is confined to the sodium exit side if the electrolyte, a sodium/sodium cell of the type shown in Figure 2.4 was made from a specimen of large grain size electrolyte, Figure 2.1B, which had been ground and polished with one micron diamond paste on both sides. This cell was operated in only one direction, with the inside electrode always acting as the cathode. It was operated at 300°C with a current density of 100 mA/cm^2 for 152.5 hours,

then removed from the Na and cleaned in ethanol. The electrolyte was stained in silver nitrate solution so that any cracks that might have formed during testing would be visible under the optical microscope. No signs of degradation were seen on the anode surface, where sodium metal was oxidized, but on the cathode side, where sodium ions were reduced, the cracks of Figure 3.21 at the boundaries of large grains were observed. A cross-section of the electrolyte has a chemically darkened layer at both the anode, Figure 3.22A, and the cathode, Figure 3.22B, but only the cathode has a thin, extremely dark layer with a high density of microcracks.

An electrolyte from a British Railway sodium/sulfur cell cycled to 414 Ah/cm^2 of charge transfer, Figure 3.23, shows an annular crack running parallel to the sodium interface, with the material on the sodium side of the crack darkened, while the material on the sulfur side of the crack is not darkened. This specimen was rough ground on a belt grinder. In the degraded layer at the sodium interface, shown at a higher magnification in Figure 3.24, a crack runs parallel to the interface, and only in a few places does it meet the interface. It does not seem to be a typical mode I crack. An Auger study of the composition near the surface detected almost two atomic per cent calcium, with the calcium concentration falling off rapidly as the distance from the interface increases, as shown in Figure 3.25 along with a SEM micrograph of the sodium surface. The crack parallel to the interface is again visible. There was also about one per cent silicon in this specimen. These impurities, particularly the calcium, create a layer of high ionic

resistivity and contribute to mode II degradation, where sodium ions are reduced to metallic sodium inside the electrolyte, creating a stress which can produce internal cracks in the electrolyte. The cracks are found, as expected, at the end of the layer containing impurities. A specimen of the same electrolyte ground by hand, Figure 3.26, has some surface degradation, but does not have the crack parallel to the surface, so the impurity weakened the electrolyte so that the crack would form easily, but did not actually crack the electrolyte.

Exposure of the electrolyte to moisture contributes to the formation of the degraded layer. The British Railway electrolyte of Figure 3.27 was removed from the sodium and exposed to 100% relative humidity for 984 hours early in its testing. After 567 Ah/cm^2 of charge transfer, it has substantially more surface degradation than the cell of Figure 3.19, which was cycled to 539 Ah/cm^2, but was not exposed to moisture.

Asymmetric polarization of sodium/sodium cells has been associated with short electrolyte life, and cracking and crumbling of the electrolyte (Br 80b). Brown Boveri cell E6123, Figure 3.28, had increasingly asymmetric resistance during operation. It was operated for a total of 1140 Ah/cm^2, and at the end of operation, the resistance during emptying was 70% higher than the resistance during filling. There is some darkening at the surfaces, indicating degradation. Figure 3.29 shows surface degradation in the SEM. The degradation on the inside and outside surfaces does not appear to differ greatly.

After a charge transfer of 690 Ah/cm^2, many cracks through the electrolyte are visible in cell V69 F206, Figure 3.30. This electrolyte

was operated at a current density of 0.9 A/cm^2, compared to 0.77 A/cm^2 for most of the Brown Boveri specimens. A polished and thermally etched specimen shows microcracks near the surface, Figure 3.31. In Figure 3.32, another specimen that was not so carefully polished shows the usual surface degradation.

Cell E3307 had been pretreated for two hours in cold concentrated HCl and had a high resistance. After only 90 Ah/cm^2, it has through cracks similar to cell V69 F206 and visible in Figure 3.33. Figures 3.34 and 3.35 show some surface degradation.

Electrolytes from recent General Electric cells have no mode I cracks and also show little or no evidence of a degraded layer at the surface. An optical micrograph of a cell cycled to 1433 Ah/cm^2, Figure 3.36, has several distinct bands of varying shades of brown after staining with silver nitrate solution, but there is no evidence of degradation at the sodium interface, Figure 3.37. The formation of the degraded layer depends on the ceramic, and since it involves grain boundary cracking and grain boundaries are easy diffusion paths for oxygen vacancies, it is likely that the grain boundary structure is important. Lattice images of the Ceramatec electrolyte used in this thesis, however, show no second phase at the grain boundaries (De 82c).

3.2.3. Processing Flaws

Finally, a few processing flaws have been observed, and some of these clearly contribute to electrolyte degradation.

Regions of high porosity, such as Figure 3.38, were found in CGE cell 5/40 in the SEM. It was not possible to correlate these regions with degradation of the electrolyte.

Figure 3.39 shows an uneven darkened layer in the electrolyte from CGE cell 5/73. The darkened layer did not penetrate as far in one spot on the sodium exit side, and in this spot are some large grains and a void, which can be seen more clearly in the SEM, Figure 3.40. The large grains may have grown from this void, which could have contained some compositional inhomogenity. Table 3.1 gives the results of analysis in the SEM in the region of this flaw. The silver is probably from ion exchange during staining, and it is interesting to note that the two large grain analyses have 7.35 and 5.01 atomic per cent silver, which would correspond to silver beta-alumina, while the total of silver and sodium for the fine grain regions is 21.90 and 17.92, a mixed sodium and silver beta"-alumina. The crack penetrating through the electrolyte has no darkened layer around it, meaning that it was not exposed to molten sodium, but was formed during sectioning or grinding of the electrolyte. Thus this region is a preferential site for mode I degradation and for mechanical cracking.

Figure 3.41 shows a silicon rich inclusion in cell 5/37, and analyses of the inclusion, the light colored ring around it, and the bulk of the electrolyte are given in Table 3.2. The region around the inclusion contains no silver. Also there are cracks in this region. This

inclusion did not appear to cause degradation of the electrolyte, but a similar inclusion at the surface might have.

Brown Boveri cell E3307 had several flaws similar to the one shown in Figure 3.42. Probably these flaws are due to an agglomerate in the raw material which densified rapidly and pulled away from the surrounding electrolyte. Such a flaw at the surface, Figure 3.43, allows the sodium to penetrate into the electrolyte, so that the degraded layer is about twice as thick as in the surrounding material. This would provide a better site for the initiation of mode I degradation.

Another Brown Boveri cell, E6123, has a lacey inclusion at the surface, Figure 3.44, and Wilder at Brown Boveri has found that such flaws are due to a high concentration of MgO, and they are often associated with the failure of cells (Sa 82).

3.3. Conclusions

Mode I degradation appears to be related to processing flaws. Electrolytes from CGE have many processing flaws and also many mode I cracks, and cracks were observed at the boundaries of large grains in large grain size electrolyte.

Not all electrolytes undergo mode I degradation. Possible reasons include the flaw populations and purities of the electrolytes.

Formation of the degraded layer may provide flaws for mode I degradation in materials which initially lacked severe flaws. Again, some electrolyte specimens, particularly the General Electric material, showed little sign of surface degradation. This may be due to higher purity of this electrolyte.

Other factors contributing to electrolyte degradation were exposure to moisture and to HCl.

4. ACOUSTIC EMISSION STUDY OF CRITICAL CURRENT DENSITY

A study of the dependence of the critical current density at which degradation begins on temperature, surface condition, and time was performed on fine grain size beta"-alumina, microstructure A in Figure 2.1. Sodium/sodium cells were run overnight at 25 mA/cm^2 with the inside electrode acting as the cathode, and then the current was reversed for 30 minutes to insure good wetting of the outside surface of the electrolyte. The current was again reversed for another 30 minutes; then the cells were tested. A current ramp was generated with a programmer and galvanostat (Princeton Applied Research Corporation, Princeton, New Jersey, Model 175 Universal Programmer and Model 371 Potentiostat-Galvanostat) so that the current through the cell started at zero and increased linearly with time as the stress or strain would in a mechanical strength test. The current vs. the terminal voltage was plotted on an x-y recorder (Hewlett-Packard Model 7004B). A computerized acoustic emission system (Acoustic Emission Technology, Sacramento, California, AET 5000) was used to determine when the cracking began and to distinguish signals due to cracking from those due to electrical noise or mechanical vibrations.

Propagation of mode I cracks depends on the distribution of surface flaws, the distribution of local current densities at these flaws, and on the microstructure of the material around the flaws. When these factors are combined, a critical current density exists at which a mode I crack could propagate from each flaw. These flaws are distributed at random over the surface of the electrolyte, so there is a random distribution of critical current densities on the surface, and the electrolyte

will fail when the lowest of these critical current densities is exceeded. It is then possible to divide the surface into elements of area, each element having the critical current density of the most severe flaw in the element. Then, assuming that any dependence of the critical current density of one element of area on the other elements of area in the material weakens with increasing distance between elements, the critical current densities of electrolyte specimens can be described by Weibull statistics (Ga 78). Then the probability of survival, P_s, of a specimen of area A tested to a current density j is:

$$P_s = \exp\{-\int_A [(j - j_u)/j_o]^n \, dA\} \tag{4.1}$$

where j_u, j_o, and n are materials parameters. The current density below which all electrolyte specimens would survive is j_u. Because j_u could not be determined from these experiments, it will be assumed here that that j_u is zero. The Weibull modulus, n, is a measure of the variability of the data, and j_o is a normalizing parameter. If the variations in current density over the electrolyte surface are random and have only short range interactions, as should be the case for the variations in local current density caused by variations in electrolyte microstructure, these variations can be ignored for the purpose of integrating equation (4.1), so

$$P_s = \exp\{-A[(j - j_u)/j_o]^n\} \tag{4.2}$$

which is similar to the equation used for the mechanical strength of materials (Da 79):

$$P_s = \exp\{-V[(\sigma - \sigma_u)/\sigma_o]^m\} \tag{4.3}$$

where σ is the stress.

For easily fabricated cell geometries, the current density varies in a regular manner over the surface of the electrolyte, and this variation cannot be ignored. Therefore, in order to integrate equation (4.1), the secondary current distribution on the electrodes is calculated numerically in appendix A. From the results of this appendix for cells with non-uniform current distributions, Equation (4.2) becomes

$$P_s = \exp\{-A[(j - j_u)/j_o]^{nC}\} \tag{4.4}$$

where C is a function of the current distribution on the electrode and of the Weibull modulus, n. Combining equations (4.2) and (4.4),

$$P_s(\text{uniform}) = P_s^{1/C} \tag{4.5}$$

Values of C appropriate for these experiments are given in the Appendix. This correction is important for cells with small electrode area, thick electrolyte, small surface resistace, and large Weibull modulus. The values of C depend critically on the geometry of seals joining the electrolyte to the other parts of the cell. The average Weibull modulus for the acoustic emissions results is 2.86, and for a surface resistance of 10^{-6} ohm.m^2, C = 1.33.

Figure 4.1 shows the acoustic emission events and terminal voltage vs. current density for a typical cell. As the cell current increased, first a few intermittent signals were detected, and then at a higher current density the acoustic activity became continuous. Finally the voltage on the x-y recorder dropped slightly. Thus three parameters were obtained for each cell; the current densities at which the acoustic emission began, became continuous, and at which the terminal voltage dropped. These data were plotted on Weibull plots, using the equation:

$$\ln \ln (1/P_s) = \ln(A) + n \ln(j) - n \ln(j_o) + \ln(C) \quad (4.6)$$

Then $\ln \ln(1/P_s)$ is plotted vs. $\ln(j)$, and n, the Weibull modulus, is the slope of the plot. The data are ranked for plotting, and the mean rank position of the ith ranked specimen from a total of N specimens is

$$P_s = 1 - i/(N + 1) \quad (4.7)$$

Least squares lines were fitted to the data, and the adjustment was made for nonuniform current distribution with C = 1.33. From the corrected lines, the current density at which half of a population of cells would be expected to survive and half to fail, j_{50}, is found.

Cells were tested at 200°C, 300°C, and 350°C, with as sintered and ground surfaces, and at rates of increase of current density of 1 mA/cm^2-sec and 10 mA/cm^2-sec. Figure 4.2 shows that the results are similar for specimens with ground and as sintered surfaces. For cells tested at 300°C with a rate of increase of current density of 10 mA/cm^2, j_{50} for cells with as sintered surfaces is 1637 mA/cm^2, and 1916 mA/cm^2 with ground surfaces. Because these results do not differ greatly, in the remaining plots data for ground and as sintered specimens are combined.

The data for the current density and terminal voltage at which a drop in cell resistance occurred for fine grain size cells with as sintered surfaces are plotted in Figures 4.3 and 4.4. From these data, the critical current density was independent of temperature, and the corresponding voltages differed because the resistivity of the electrolyte varied with temperature. Thus the breakdown process appears to be related to the current density rather than the terminal voltage, so the rest of the data were plotted vs. current density.

Figures 4.5, 4.6, and 4.7 show that the critical current density for initial and continuous acoustic emission and for a drop in cell resistance all increased when the rate of increase of current density in the test was higher. The effect was greater for initial than for continuous acoustic emission, and was least for the drop in cell resistance. This indicates that the time dependence for the initiation of mode I degradation is greater than that for the propagation of the cracks. This indicates that some time dependent process is important at low current densities, but becomes less important at high current densities. Possible time dependent degradation mechanisms will be discussed in section 6, and a critical crack growth mechanism that is operative at high current density will be described in section 5.

5. MODE I DEGRADATION

The results of acoustic emission tests and microscopic examination of used electrolytes suggest that the degradation of beta"-alumina involves mechanical cracking at high current density, and at low current density and long time it also involves electrochemical corrosion. In this section, various attempts to describe the propagation of cracks through the electrolyte by mechanical cracking will be reviewed, and the effects of the mechanical properties of beta"-alumina and the current distribution on flaws in the electrolyte surface on mode I degradation will be discussed.

5.1 Prediction of Critical Current Density for Crack Propagation

At the negative electrode of a sodium/sodium cell, or at the sodium electrode of a sodium/sulfur cell during charging, sodium metal will form electrolytically on the electrolyte surface, including the inside of sodium filled surface flaws. If the rate of formation of sodium, which is proportional to the current density, is great enough, the Poiseuille pressure produced as this molten sodium metal flows out to the free surface could cause the flaws to extend, Figure 5.1, as first proposed by Armstrong, Dickinson, and Turner (Ar 74). The critical current density at which a flaw is predicted to extend depends on the assumptions made about the geometry of the flaw and the properties of the electrolyte.

The Poiseuille pressure for flow of a fluid of viscosity η between parallel plates of spacing 2y is

$$dP/dx = -3\,\eta v/y^2 \qquad (5.1)$$

and the width of a sodium filled crack depends on the internal pressure, so the problem would have to be solved by iteration, assuming either a pressure distribution or crack shape, then calculating the other quantity, and repeating the process until the crack shape and pressure distribution are consistent. Because of the complexity of this problem, simplifications must be made.

Several calculations of critical current densities for a two-dimensional crack have been made. Shetty et al. (Sh 77) assumed an edge crack in a semi-infinite plate, and assumed that the Poiseuille pressure would increase linearly along the crack, starting at the ambient pressure at the crack opening. Then the crack shape that would be produced by this pressure distribution was calculated. Virkar (Vi 81) calculated the primary current distribution on a crack of zero width, to determine the rate at which sodium would fill the crack. The pressure distribution that this current distribution would produce in a rectangular crack was approximately linear, and using the crack geometry and width of (Sh 77) for a linearly increasing pressure distribution, a critical current density in A/cm^2 of

$$j_{crit} = 124.39/l \qquad (5.2)$$

was predicted for a crack of length l in cm.

Feldman and De Jonghe (Fe 82) assumed an elliptic-cylindrical crack geometry, and from this calculated the primary current distribution, sodium flow velocity, and crack opening displacement. The calculated pressure distribution is linear over most of the crack length, but rises sharply at the crack tip. The critical current density is

$$j_{crit} = K_{Ic}^4/E^3 \; F/(3.32 \; nV_m l) \tag{5.3}$$

where K_{Ic} is the critical stress intensity factor, E is the elastic modulus, F is Faraday's constant, and V_m is the molar volume of sodium. Inserting the appropriate constants (Fe 82)

$$j_{crit} = 250/l \tag{5.4}$$

a factor of two greater than (5.3). For a crack length of 100 microns, the predicted critical current density is 25,000 A/cm^2, while observed critical current densities are 10 to 20 A/cm^2 for visible cracks (Vi 83), and a few hundred mA/cm^2 for acoustic emission due to crack propagation.

A three-dimensional calculation by Virkar and Viswanathan (Vi 83) gave a much lower predicted critical current density. For a rectangular crack of width 2c and length l, with approximately a primary current distribution, the critical current density is

$$j_{crit} = \frac{\pi}{32} \frac{(1 - \nu^2)^3 \; FK_{Ic}^4}{E^3 V_m \eta} \frac{c^2}{l^3} \tag{5.5}$$

so that for a crack 100 microns long and 60 microns wide, the critical current density is 150 A/cm^2.

The current distribution for small objects is much more uniform than for large objects, so the primary current distribution is not a good approximation for a surface flaw in beta"-alumina. Brennan attempted to determine the effect of a finite charge transfer resistance on the current distribution, and thus on the critical current density, (Br 80), but the equivalent circuit he used to approximate a sodium filled crack predicts that for zero charge transfer resistance all the

current will enter the crack at the tip, while the actual primary current distribution would have a maximum in the current density at the crack tip, but some current entering the sides of the crack as well. Also, this model predicts that a finite charge transfer resistance will lower the critical current density. It would seem that the amount of current flowing into the crack would be reduced by the charge transfer resistance, and the critical current density would be increased. The secondary current distribution on a crack of length 10 microns is calculated in the Appendix, and it is compared to the primary current distribution from Feldman et al. (Fe 82) in Figure 5.2. The primary current distribution predicts a current density at the crack tip 1/r times the average, which for a crack 10 microns long and with 7.3 nm crack opening displacement is $1/r = 316$, while the secondary current distribution at the crack tip is only 1.1 times the average current density, independent of the crack opening displacement. The total current entering the crack is $2j_o l$ for the primary, and $1.68j_o l$ for the secondary current distribution. For a uniform current distribution, the total current into the flaw would be $2j_o l$. The secondary current distribution resembles a uniform current distribution.

A three dimensional calculation of critical current density was made, closely following the calculation by Virkar et al. (Vi 83), but using a uniform current distribution rather than the primary current distribution. For a long, flat crack, as shown in Figure 5.3, of length l and width 2c, with the crack opening at $x = 0$, and the crack tip at $x = l$, the volume rate of flow of sodium at any point x along the crack will be equal to the rate of formation of sodium by electrolysis from x

to the tip of the crack,

$$dV/dt = \int_x^l j_o 4cV_m/F \, dx \tag{5.6}$$

where V_m is the molar volume of sodium and F is Faraday's constant, or

$$dV/dt = 4j_o cV_m(1 - x)/F \tag{5.7}$$

When the crack is pressurized by this flow of sodium, assuming that each element of length along the crack can deform independently, its shape will be elliptical and the semi-minor diameter, according to (Sn 69), is

$$b = (1 - nu^2)cP/E \tag{5.8}$$

where ν is Poisson's ratio, P is the pressure in the crack at that point, and E is Young's modulus for the electrolyte. The assumption that each element of length of the crack can deform independently would not be valid near the crack tip, but should apply far from the crack tip as long as the cross section does not vary rapidly with change in x, the position on the crack. The pressure in the crack is then related to the volume flow rate by the Hagen-Poiseuille law, which for an elliptic cross-section is (Be 63)

$$dV/dt = (\pi dP/dx/4\eta)(c^3b^3/(c^2 + b^2) \tag{5.9}$$

Then assuming $c >> b$, and combining 5.7, 5.8, and 5.9,

$$P^3dP/dx = 16 \, \eta V_m E^3 j_o(1 - x)/\pi \, F(1 - \nu^2)^3c^3 \tag{5.10}$$

which, when integrated, is

$$P^4 = 64\eta j_o V_m E^3(1x - x^2/2)/\pi F(1 - \nu^2)^3c^3 \tag{5.11}$$

The pressure is a maximum at the crack tip, x = l,

$$P = [32\eta j_o V_m E^3 l^2/\pi F(1 - \nu^2)^3 c^3]^{1/4} \quad (5.12)$$

The critical pressure for crack extension is

$$P_{cr} = [\pi K_{Ic}^2/4c]^{1/2} \quad (5.13)$$

and the critical current density for crack extension can be found by equating the right sides of 5.12 and 5.13 and solving for j,

$$j_{cr} = [\pi^3(1 - \nu^2)^3 F K_{Ic}^4]/[512\ V_m E^3 \eta](c/l^2) \quad (5.14)$$

This differs by a factor of $\pi^2/16$ l/c from equation 5.5, for a primary current distribution. Then for ν = 0.25, F = 96,500 coul/mol, K_{Ic} = 1.984 MPa.$m^{1/2}$ from Table 5.2, V sub m = 2.37×10^{-5} m^3/mol, E = 200 GPa (Sh 77) and $\eta = 3.4 \times 10^{-4}$ N sec/m^2, j_{cr} = 347 A/cm^2 for a crack width of 60 microns and a length of 100 microns, and for 60 micron width and 200 micron length, j_{cr} = 87 A/cm^2.

Roughly an order of magnitude difference remains between the predicted j_{cr} for a 3-dimensional crack with a uniform current distribution and the current density at which crack propagation was observed visually (Vi 83), while degradation can be detected by acoustic emissions about three orders of magnitude below the predicted j_{cr}. Two possible reasons for this difference are the use of an inappropriate value for the fracture toughness in equations (5.3), (5.5), and (5.14), and the presence of residual stresses in the microstructure. These factors will be discussed in the following subsections.

5.2 Fracture Toughness Anisotropy

According to equations (5.3), (5.5), and (5.14), j_{cr} is proportional to K_{Ic}^4, so the fracture toughness has an important effect on mode I degradation. Measurements of K_{Ic} typically are for a through crack

propagating in a plate, while a mode I crack is long and narrow, like a ribbon or a dendrite. The mode I crack should then have more freedom to select an easy path through the microstructure than would a through crack, so a lower value of K_{Ic} might be appropriate for the prediction of critical current density. This would be true especially for initial acoustic emission, where a crack might propagate along a single grain boundary or through a single favorably oriented grain. Thus, a single crystal value of K_{Ic} might be appropriate for the prediction of the current density at which initial acoustic emission would occur. Since 00.1 cleavage is most likely to be involved in the initial crack configuration, it is necessary to determine the K_{Ic} anisotropy. The K_c values were found from cracks produced by a microhardness tester on basal and on prismatic planes of sodium beta-alumina single crystals.

The expression used to calculate K_{Ic} was (An 81)

$$S = K_{Ic}(H/E)^{1/2}/(P/c^{3/2})$$

$$= 0.016 \pm 0.004 \qquad (5.15)$$

where S is a material-independent constant for radial cracks produced by a Vickers diamond indenter, H the hardness, E Young's modulus, P the load on the indenter, and c the measured length of the radial cracks. The Young's modulus for polycrystalline sodium beta"-alumina is reported to be about 200 GPa (Sh 77). For indentation fractures in elastically anisotropic crystals, the modulus E used in equation (5.15) should be that for the direction perpendicular to the crack habit plane. Measurements of the elastic anisotropy were not available, but a fair estimate can be made from the shape of Knoop indents. Knoop indents were made on

basal-plane surfaces and on prism-plane surfaces with the long axis of the indenter in the 00.1 plane. In the fully loaded state, the ratio of the length of the long axis, a, to the short axis, b, of the indent is 7.11. When the load is removed, the length of the long axis of the indent remains essentially constant, but the length of the short axis decreases by an amount depending on H/E, the ratio of the hardness to elastic modulus. The ratio H/E was found from (Ma 82)

$$b'/a = b/a - \alpha H/E \tag{5.16}$$

where b' is the length of the short axis after the load has been removed, and α is a constant equal to 0.45. Hardness, H, was calculated from Vickers indents and then E was derived from the H/E values and from H. The various values of H/E, H, and E so determined from the Knoop indents are listed in Table 5.1. It was interesting to note that both the hardness and the fracture toughness decreased with load, P, for indentations made on the basal plane surfaces, according to:

$$H(GPa) = 13.5 - 3.37 \times 10^{-5} \times P(N)^3 \pm 0.1 \tag{5.17}$$

and

$$K_c(MPa.m^{1/2}) = 0.916 - 6.42 \times 10^{-7} \times P(N)^3 \pm 0.003 \tag{5.18}$$

in the measured range, up to about 50 N. Additional complications, such as the temperature dependence of the hardness (Th 83), were not studied. The hardness of the polycrystal also appeared to decrease somewhat in these parameters for loads exceeding 50 N. The reason for this behavior is not entirely clear; it was caused possibly by subsurface basal-plane cracking that seemed to accompany indentations on basal-plane surfaces with increasing loads. Subsidiary cracking also became prominent in the

polycrystalline electrolytes at high indenter loads. The apparent reduction in hardness could then be due to the reduced elastic constraint of the plastically deformed material under the indent, allowing it to become larger so that both the hardness and K_c would decrease. The phenomenon of subsidiary cracking for basal-plane cracks may have caused these values to be systematically low. For indents made on prismatic plane surfaces, no such subsidiary cracking occurred and no load dependence was observed up to 20 N; larger loads on these surfaces splintered the crystals. The K_c values found for basal-plane-surface indents were about half those found from cracks formed normal to the basal planes — the short cracks of Figure 2.5. Because the basal-plane surface indents were not well-behaved, it was felt that the indents on the prism-plane surfaces yielded the significant values of the fracture toughness, and these are the values presented in Table 5.2. These fracture toughness values were determined from the measurements of the Vickers indenter cracks produced on the prism-plane surfaces and from the values for E1 and E2 listed in Table 5.1. The K_c values for cracks running in the 00.1 direction of the single crystals and for polycrystals (Table 5.2) are somewhat lower than the values for polycrystals measured by macroscopic fracture-mechanics methods, 3.21 $MPa.m^{1/2}$ (Vi 77). This is typical of crystalline ionic ceramics, while covalent ceramics give better agreement, and glasses have higher fracture toughness by indentation than by macroscopic methods (An 81). The K_c values for cracks in the 00.1 planes were a factor of ten lower than these values. When the 00.1 crack value, $K_c = 0.162$ $MPa.m^{1/2}$, is inserted into equation (5.14), for a crack width of 60 microns and a crack length of 100 microns $j_{cr} = 20$ mA/cm^2, while the lowest current density for initial crack propagation detected in the

acoustic emissions study of section 4 was about 70 mA/cm^2. It is therefore concluded that mode I crack initiation in sodium beta- and beta"-aluminas can occur well below the average values observed for rapid, catastrophic electrolyte failure, in agreement with the acoustic emissions study.

5.3. Effect of Residual Stresses on Mode I Degradation

An applied mechanical stress would affect mode I degradation in two ways. First, it will change the width of the crack, thereby changing the Poiseuille pressure. Second, it will contribute to the stress intensity at the crack tip. The analysis by Feldman and De Jonghe (Fe 82), whereby a pre-existing elliptical-cylindrical crack is propagated under the influence of electrolysis-generated Poiseuille pressure leads to an expression for the stress intensity at the crack tip of the form:

$$K_I^P = f\delta^{-3} j_o \tag{5.19}$$

where f is constant for constant crack length and is dependent on the viscosity of the sodium, δ is the crack opening displacement, and j_o is the macroscopic current density. We will assume here that, to a first approximation, the crack shape is independent of the source of the stress, and remains elliptical. The total stress intensity factor at criticality, K_{Ic}, can then be expressed as

$$K_{Ic} = K_I^P + K_I^\sigma \tag{5.20}$$

or

$$1 = K_I^P/K_{Ic} + K_I^\sigma/K_{Ic} \tag{5.21}$$

where K_I^P is the component of K_I due to the electrical current, and K_I^σ is

the component due to the applied mechanical stress. Since

$$K_{Ic} = f\delta_{cr}^{-3} j_{cr}(0) = g\sigma_{cr} \tag{5.22}$$

where $j_{cr}(0)$ is the critical current density at $\sigma = 0$, σ_{cr} is the critical mechanical stress at $j_o = 0$, and g is a constant (Ta 73), Equations (5.20) to (5.22) yield for the critical current in the presence of a stress, $j_{cr}(\sigma)$

$$j_{cr}(\sigma)/j_{cr}(0) = 1 - \sigma/\sigma_{cr} \tag{5.23}$$

Equation (5.23) clearly shows that the critical current for failure initiation is linearly dependent on the applied stress. Then compressive stresses will tend to prevent mode I cracking, while tensile stresses will promote cracking. Such stresses could arise due to the thermal expansion anisotropy of beta"-alumina.

5.4 Stresses Due to Thermal Expansion Anisotropy

For magnesia stabilized beta"-alumina, Radzilowski found thermal expansion coefficients of 7.8×10^{-6} and $7.3 \times 10^{-6}/°C$ in the a and c directions, respectively (Ra 70). Because the weak grain boundaries parallel to the basal plane are perpendicular to the direction of low thermal expansion, they will not be expected to display microcracking.

Thermal stresses have been calculated by Evans (Ev 78) for a grain with anisotropic thermal expansion in an isotropic matrix. For a flaw, such as a pore, at a triple point, Figure 5.4, the stress intensity at the end of the pore remote from the triple point is

$$K_o(Q) = P l^{1/2}(\cos\beta/2)A(\beta,\nu)[(a/l)/\pi]^{1/2}[\ln(l/a)-0.31] \tag{5.24}$$

where P is the thermal stress,

$$P = \frac{E\ \Delta T\ \Delta\alpha}{1 + \nu}$$

l is the length of a grain facet, β is the angle shown in Figure 5.4, 2a is the flaw size, and $A(\beta, \nu)$ is a function of and in the range $\pm 2\pi$.

Electrolyte with a maximum grain size of about 300 microns had no microcracks due to thermal stresses, and electrolytes of practical interest have much smaller maximum grain sizes, about 20 microns. If the flaw in Figure 5.4 is a mode I crack, then $K_o(Q)$ is equivalent to K_I^σ in equation (5.20). Then if $K_o(Q)$ for a 300 micron grain is just less than K_{Ic},

$$K_o(Q)(300\ \text{micron}) = K_{Ic}$$

Then if the flaw size is proportional to the grain size, from equation (5.24)

$$K_o(Q)0 \propto l^{1/2} \tag{5.25}$$

and combining this with equation 5.21 and 5.22,

$$j_{cr}(\text{thermal stress})/j_{cr}(0) = 1 - (20/300)^{1/2} = 0.74$$

so thermal stresses would account for only a slight difference between the predicted and the observed critical current density.

Another possible source of surface stresses is substitution of an impurity such as potassium or calcium for sodium. From Table 1.1, this will cause a 1.5% tensile strain, or a 2% compressive strain in the c direction for complete substitution of calcium and potassium respectively. Then, if the strain is linearly proportional to the impurity concentration, substitution of calcium for one per cent of the sodium

will produce as great a stress due to anisotropic strain as a 500°C change in temperature.

5.4. Conclusions

Calculations of critical current density assuming isotropic electrolyte predict values an order of magnitude higher than those observed for rapid propagation of large cracks, and several orders of magnitude higher than critical current densities determined by acoustic emissions testing. These differences can be explained in part by the low fracture toughness of beta"-alumina for cracks following the 00.1 cleavage plane. The Poiseuille pressure model cannot explain the time dependence observed in the acoustic emissions results. Possible time dependent degradation mechanisms will be presented in the next section.

To avoid mode I degradation, the grain size and flaw size of the electrolyte should be kept small, and the fracture toughness of the electrolyte should be high.

6. TIME DEPENDENT DEGRADATION

The observed degradation of beta"-alumina by sodium can be attributed to two distinct processes, critical fracture due to Poiseuille pressure in surface flaws as described in section 5 and, for longer times and lower current densities, chemical or electrochemical attack. In this section two possible corrosion mechanisms will be discussed.

6.1 Change in Composition of Sodium Electrode during Cycling

Both models involve a change in the concentration of a solute in the sodium. During charging of a Na/S cell, or at the exit side of a Na/Na cell, fresh sodium which does not contain solute (unless the electrolyte dissolves in the sodium as it forms) is formed electrochemically at the electrolyte/sodium interface. The solute, along with the sodium in which it is dissolved, is swept away at a velocity equal to the rate of formation of sodium,

$$v = jV_m/F \tag{6.1}$$

where j is the current density, V_m is the molar volume of sodium, and F is Faraday's constant. Then the solute diffuses into the solute-free sodium, so the solute concentration follows the equation of convection and diffusion, which in one dimension is

$$\frac{\partial c}{\partial t} = D \frac{\partial^2 c}{\partial x} - v \frac{\partial c}{\partial x} \tag{6.2}$$

where D is the diffusion coefficient of solute in molten sodium, v the velocity from equation (6.1), x is the distance from the electrode/electrolyte interface as shown in Figure 6.1, t is the time for which the current has been passed, and c is the concentration. The

solute cannot pass through the electrolyte or the container, so the initial condition is $c = c_o$ for all x, and the boundary conditions are

$$D \frac{\partial c}{\partial x} = vc \quad , \quad x = 0$$

$$c = c_o \quad , \quad x \rightarrow \infty \tag{6.3}$$

For the cell geometry shown in Figure 6.1, the problem is identical to the settling of particles in a suspension under the influence of gravity and Brownian motion, for which solutions are available. Mason and Weaver (Ma 24) give the solution

$$c/c_o = \frac{-v\sqrt{t}}{\sqrt{D\pi}} \exp -[(vt - x)^2/4Dt] + \frac{1}{2}\left[1 - \operatorname{erf}\left(\frac{vt - x}{\sqrt{4Dt}}\right)\right]$$

$$+ \frac{1}{2} \exp\left(\frac{vx}{D}\right)\left[1 + \frac{v}{D}(vt + x)\right]\left[1 - \operatorname{erf}\left(\frac{vt + x}{\sqrt{4DT}}\right)\right] \tag{6.4}$$

For $D = 5 \times 10^{-9}$ m^2/sec and $j = 10^3$ A/m^2, the concentration profile at various times is shown in Figure 6.2. After 24 hours, the concentration of solute at the surface is 0.35 of the initial concentration. The important factor for the degradation process is the concentration at the electrolyte/sodium interface, and this is shown for a variety of current densities and times in Figure 6.3.

From Feldman and De Jonghe (Fe 82), inside a surface flaw or crack, the velocity is increased by a factor l/r, where l is the crack length and r is half the crack opening displacement, compared to the velocity on the electrolyte surface given in equation (6.1), so that in a crack,

$$v = (j\ V_m/F)(l/r) \tag{6.5}$$

and

$$1/r = \frac{1E'F}{5.44\ j\ V_m\ \eta} \qquad (6.6)$$

For 1 = 100 micrometers and j = 10^3 A/m^2, 1/r is 1.2 × 10^4. Also the boundary conditions are changed, because the velocity at the crack opening would be given by equation (6.1), so the solute concentration will not change very rapidly. For the crack geometry shown in Figure 6.4, the boundary conditions would be

$$D\frac{\partial c}{\partial x} = vc \quad , \quad x = 0$$

$$c = c_o \quad , \quad x=1 \qquad (6.7)$$

and the equation will be much more difficult to solve because the second boundary condition is not homogeneous. As an approximation, it is possible to use another solution from Mason and Weaver (Ma 24) for the settling of particles in a suspension of finite depth 1', with the boundary conditions

$$D\frac{\partial c}{\partial x} = vc \quad , \quad x = 0\ ,\ 1' \qquad (6.8)$$

and to use a depth 1' longer than the crack length so that the concentration at the crack opening, where x = 1, remains approximately constant. Then the solution is

$$c/c_o = \frac{v1'\exp\frac{vx}{D}}{D\left[\exp\left(\frac{v1'}{D}\right) - 1\right]} + 16D^2v\pi\ 1'^3\exp\left(\frac{vx}{2D}\right)\sum_{n=1}^{\infty}$$

$$\frac{\exp\left[\frac{(4D^2n^2\pi^2 + v^2l'^2)t}{4\ D\ l'^2}\right]n\left[1 - (-1)^n\exp\left(\frac{-vl'}{2D}\right)\right]\left[v\sin\frac{n\pi x}{l'} + \frac{2n\pi D}{l'}\cos\frac{n\pi x}{l'}\right]}{[4D^2n^2\pi^2 + v^2l'^2]^2} \qquad (6.9)$$

and for j = 10^3 A/m^2, 1 = 100 micrometers, and 1/r = 1.2 × 10^4, 1' is

about 108 micrometers and after 2 seconds, the concentration of solute is 0.02 of its initial value, and after one minute it reaches an steady state of 10^{-20} of the initial value. Because the steady state concentration is reached so rapidly, for most purposes the time dependent term of equation (6.9) can be ignored, and the first term, which gives the steady state concentration can be used. The steady state concentration at the crack tip for various values of the dimensionless parameter vl'/D is shown in Figure 6.5.

Because the concentration at the crack opening varies slowly with time according to equation (6.4), c_o in (6.9) could be replaced by the concentration at the interface from equation (6.4), lowering further the oxygen concentration. Thus the solute concentration in a crack can be substantially reduced by the flow of sodium out of the crack, and some effect on the degradation process is to be expected.

6.2. Dissolution of the Electrolyte

The first degradation model based on corrosion was proposed by Richman and Tennenhouse (Ri 75), who assumed that the electrolyte was soluble to a slight degree in the sodium, and that as sodium flowed out of the crack, it would carry away dissolved electrolyte which would be replaced by dissolution of the electrolyte at the crack tip. The total flux of solute depended on three terms. First, the sodium flowing out of the crack was carried the electrolyte dissolved in it. Second, during electrolysis the stress due to Poiseuille pressure as sodium flows out of the crack would raise the chemical potential at the crack tip, causing even more electrolyte to dissolve at the tip and to be swept away. Finally, the chemical potential of the electrolyte would be lower in the

crack tip due to the small radius of curvature, causing a flux of solute into the crack, opposing the other fluxes. At low current density, the flux into the crack due to capillarity would be greater than the fluxs out of the crack due to sodium flow and Poiseuille pressure, and no crack growth would be expected, but at high current density the stress and the flow terms would be larger and the crack would grow. Beta"-alumina is not subject to slow crack growth in sodium (Sh 77), so the stress term cannot be important. The solubility of beta"-alumina in sodium is too low for the observed amount of crack growth to occur simply due to the flow of sodium without an increase in chemical potential due to the stress (Ri 75), so the model has received little further attention, but beta"-alumina is known to have some slight solubility in sodium. Specimens immersed in sodium for 47 and 167 days had similar weight losses, suggesting that dissolution proceeds until a solubility limit is reached (Sm 84). Then, if the crack proceeds mostly by critical cracking along weak grain boundaries or along the easy cleavage planes of grains, according to the Poiseuille pressure model of section 5, and only in a few areas of higher fracture toughness by dissolution of the electrolyte, the model might be plausible.

6.3. Destructive Reduction of the Electrolyte

A second possible corrosion mechanism is chemical reduction of the electrolyte. Normally the sodium used in testing electrolyte is saturated with oxygen, setting the oxygen fugacity in the sodium at about 10^{-62} atmospheres at 300°C. Beta"-alumina is reduced to some degree even by immersion in sodium saturated with oxygen, but the degree of reduction should depend on the oxygen fugacity. If the the defect

formed in the electrolyte is doubly charged oxygen vacancies, the reaction can be written with Kroger-Vinck notation

$$O_o^x = V_o^{\cdot\cdot} + 2e' + \frac{1}{2} O_2 \tag{6.10}$$

where O_o^x, an oxygen ion on an oxygen site in the lattice, with the normal charge for that site, leaves the lattice, forming an oxygen vacancy which is neutral, but occupies the site of an ion of charge -2, so its charge relative to the site is +2, $V_o^{\cdot\cdot}$, and two free electrons, e', with charge -1, and half an oxygen molecule. Then the equilibrium constant for this reaction is

$$K_{eq} = P_{O_2}^{1/2} [V_o^{\cdot\cdot}][e']^2/[O_x^x] \tag{6.11}$$

To preserve electroneutrality,

$$[V_o^{\cdot\cdot}] - 2[e'] = 0 \tag{6.12}$$

and when this is substituted into (6.11),

$$[V_o^{\cdot\cdot}] \propto P_{O_2}^{1/6} \tag{6.13}$$

So at some low oxygen fugacity $[V_o^{\cdot\cdot}]$ should become large enough to weaken the electrolyte substantially, and this can be considered a critical oxygen concentration for the onset of degradation, C_{cr}. The current density is proportional to vl'/D, so Figure 6.5 shows that equilibrium concentration drops rapidly as current density increases. A critical current density above which slow degradation will proceed can be calculated by substituting the velocity from equation (6.5) into the first term of (6.9) for the steady state concentration with x = 0 at the crack tip, and for exp(vl'/D) much greater than 1,

$$C_{cr}/C_o = (j_{cr}V_m/FD)(1/r) \exp - [(j_{cr}V_m/FD)(1/r)] \quad (6.14)$$

and this can be solved for j_{cr} by iteration.

Because oxygen vacancies diffuse more rapidly along the grain boundaries than through the bulk grains (De 82a), grain boundary cracking or weakening is expected. The degraded layer described in section 3 does indeed exhibit grain boundary cracking.

6.4 Crack Velocity

Finally, for a prediction of crack velocity it is necessary to consider the chemistry of bond breaking at the crack tip. Four possible chemical reactions are

$$Al\text{-}O\text{-}Al = Al\text{-}O^* + Al^* \quad (6.15)$$

$$Al\text{-}O\text{-}Al + Na_2O = 2Al\text{-}O\text{-}Na \quad (6.16)$$

$$Al\text{-}O\text{-}Al + Na = Al\text{-}O\text{-}Na + Al^* \quad (6.17)$$

$$Al\text{-}O\text{-}Al + 2Na = 2Al^* + Na_2O \quad (6.18)$$

where Al-O-Al represents any segment of the aluminum-oxygen lattice of beta"-alumina, and Al-O* or Al* represent oxygen or aluminum ions with a broken bond. Reaction (6.15) would apply to fracture in vacuum. In sodium saturated with sodium oxide, any of the remaining reactions would be possible, but (6.16) might be most favorable, as it leaves no unsatisfied bonds. Under these conditions, no slow crack growth is observed (Sh 77), but the strength is lowered by about 25% compared to air (Da 79a). In oxygen-free sodium, only reactions (6.17) and (6.18) would be possible. This might be the reason that beta"-alumina is degraded more severely by oxygen-saturated sodium than by oxygen-free sodium (Ba 84).

Because there is likely to be a change of crack tip reaction when the oxygen concentration drops during electrolysis, slow crack growth is possible under this condition. The derivation of the crack velocity follows Lawn and Wilshaw (La 75b). The change in energy of the system and environment, δU, for the extension of the crack a distance δc, with crack extension force

$$G=K_I^2/E + K_{II}^2/E + K_{III}^2(1 + \nu)/E \tag{6.19}$$

by breaking the N bonds existing in this distance δc, is

$$\delta U = \{-G + [2\mu(Al^*) + \mu(Na_2O) - \mu(Al\text{-}O\text{-}Al) - 2\mu(Na)]N\}\ \delta c \tag{6.20}$$

assuming that reaction (6.18), which would be favored by low oxygen concentration, occurs. Then an approximate equation for the crack velocity is

$$V_c = \nu_o a_o \exp(-U_o^*/kT)$$

$$\exp(\alpha G/kT)\ \exp\{\beta[-\mu(Na_2O) + \mu'] + \mu']/kT\}\ \delta c \tag{6.21}$$

where ν_o is a vibrational frequency, $\nu_o \sim \frac{kT}{h} \sim 5\times10^{12}$ Hz, h is Planck's constant, a_o is the distance between bonds, U_o^* is an energy for nucleation or motion of kinks, so that bonds can be broken one at a time, α and β are adjustable parameters, and μ' is the difference in chemical potential change when the reaction changes from (6.16) to (6.18). The pre-exponential term is the dynamic crack velocity, about 10^3 m/sec, the first exponential is the resistance of the material to crack propagation, the second is the mechanical contribution to crack growth, and the third is the chemical contribution to crack growth. Thus a decrease in oxygen concentration can lead to an increase in crack velocity.

Theory predicts that $\alpha = \frac{a_o^2}{2}$ and $\beta = \frac{1}{2}$, but it is difficult to predict values for the chemical potentials of broken bonds, involved in the term μ', and thus calculation of crack velocities is not straightforward. Crack velocity vs. $\alpha G - U_o^*$ for various values of $\mu' - \mu(Na_2O)$ is plotted in Figure 6.6.

Both oxygen concentration and crack extension force are related to current density. Combining equations (5.12), (5.13) and (6.19),

$$G = \left(\frac{512\ n\ j_o\ V_m\ E'1^2}{\pi^3 Fc}\right)^{1/2} \tag{6.22}$$

When the oxygen concentration reaches its equilibrium value, from the first term of equation (6.9), Figure 6.7 shows the crack velocity vs. current density for various crack lengths, assuming $\mu\ (Na_2O) = kT\ \ln(c/c_o)$ and $\mu' = 0$. For $\mu' > 0$, the velocity will be lower.

Another possible reason for more severe degradation when the sodium is saturated with oxygen would be partial coverage of the electrolyte surface by a sodium oxide layer. If the current density is locally lowered by a layer of sodium oxide or some other impurity adsorbed at the interface, the current density of the clean spots would be higher to maintain the same average current density, so that the oxygen concentration in the clean areas would drop further due to the flow of current, and destructive reduction could occur in these areas, as shown in Figure 6.8.

If sodium oxide is deposited uniformly on the surface, then destructive reduction could not begin until the oxide layer was removed, so there might be some time interval between the beginning of the charging cycle and the onset of destructive reduction.

6.5. Conclusions

The concentration of a solute in the sodium electrode adjacent to the electrolyte changes only slightly during electrolysis, but in a sodium-filled crack the concentration can drop rapidly.

The Richman-Tennenhouse model, in which the crack advances by the dissolution of electrolyte from the crack tip, cannot account for all the observed crack growth, but if most of the crack growth is due to critical cracking along easy cleavage planes or weak grain boundaries, the model might be used to explain the progress of the crack through the remaining strong regions.

The oxygen concentration in cracks decreases rapidly with increasing current density, so degradation would occur when some critical current density less than that predicted in section 5 for critical cracking is exceeded.

Enhanced degradation, without slow crack growth, when sodium is saturated with oxygen, is to be expected because of a favorable crack tip chemical reaction. A different reaction at low oxygen concentration

might allow slow crack growth, or the observed time dependent degradation might be due to the removal of an oxide layer from the electrolyte surface before destructive reduction begins.

7. Conclusions

Rapid degradation of beta"-alumina at high current density, above current densities on the order of 10 A/cm^2, is well described by the Poiseuille pressure mechanism.

Evidence of time dependent degradation is observed in some, if not all, electrolytes at lower current density. A degraded layer forms on the sodium exit surface of most electrolytes, but recent Ford Motor Company and General Electric electrolytes show little evidence of this degraded layer, and also have no mode I cracks. Mode I cracks in electrolytes which have degraded layers often show signs of chemical attack. Another evidence of time dependent degradation is a dependence of critical current density as determined by acoustic emissions detection on the rate of increase of current density.

This can best be attributed to changes in the composition of the sodium electrode and the sodium/beta" alumina interface when current flows. A mechanism has been proposed in which the oxygen concentration drops, promoting crack growth. This mechanism might be tested by measuring crack velocity as a function of stress intensity and oxygen fugacity.

ACKNOWLEDGMENTS

The author would like to thank his advisor, Professor Lutgard C. De Jonghe, for his advice and suggestions throughout the course of this work,and the other professors on his committee,particularly Anthony G. Evans, for helpful discussions.

The author would also like to thank the other graduate students with whom he worked,especially Andrew C. Buechele, Robert McClelland,and Martin W. Weiser; and the technicians of MMRD for their assistance.

This work was supported by the U.S. Department of Energy under Contract No. DE-AC03-76SF00098.

APPENDIX A. CURRENT DISTRIBUTIONS

Degradation of beta"-alumina occurs when some threshold current density is exceeded. Therefore the variations in the current density due to cell geometry have been evaluated for three types of sodium/sodium cells. Also, because models used to explain the degradation process often involve current focusing on sodium filled cracks, a calculation of the secondary current distribution on such a crack has been performed.

The first cell configuration, Figure A.1A, consists of a section of beta"-alumina tube, the outside of which is covered with sealing glass except for a small circular region with a diameter of 5 mm forms the working electrode. The wall thickness of the tube is 1.3 mm, and the inside surface of the tube is the counter electrode. For the purpose of calculating the current distribution, the cell was assumed to consist of a thin electrolyte plate with a circular working electrode opposite a large counter electrode. This type of cell was not used in the experiments reported in this thesis, but more extensive calculation have been performed on this cell geometry on the accuracy of the calculation and the effect of variations in cell geometry.

The two types of cells used in this thesis are made from a beta"-alumina disk sealed to an alpha alumina tube, and the cells differ only in the seal geometry. The cell of Figure A.1B is sealed with a glass ring, so that the working electrode is the circular area of the electrolyte surface exposed to sodium inside the tube, and the counter electrode is the exposed edges of the electrolyte and the opposite side of the electrolyte. The cell of Figure A.1C has, in addition to the glass ring, sealing glass around the edge of the electrolyte, so that the

working electrode is the circular area exposed to the sodium inside the tube, and the counter electrode is the opposite side of the electrolyte disk.

Assuming a homogeneous electrolyte, electrodes of infinite conductivity, and no surface overpotential, the primary current distribution would be calculated by solving Laplace's equation. However, because the angle of the electrolyte between the electrode/electrolyte and electrolyte/insulator interfaces is obtuse (180°), the primary current distribution becomes infinite at the electrolyte edge. Then even for small average current density the electrolyte would fail immediately at the edge. In fact, degradation is observed in the middle of tested cells about as frequently as at the edges, so the secondary current distribution, which takes into account the surface overpotential, was calculated by numerical methods, similar to those of Parrish and Newman (Pa 70). In general, eight parameters are required to define the problem, as discussed by Parrish and Newman (Pa 70). For beta"-alumina, sodium ions will be, to a good approximation, the only current carrier, so no concentration gradients in the electrolyte need be considered. Also, because the exchange current density, j_o, is much greater than the operating current density, the Butler-Vollmer equation relating current to overpotential, η_s,

$$j = j_o\{\exp[(Z\alpha_a F/RT)\eta_s] - \exp[(-Z\alpha_c F/RT)\eta_s]\} \qquad (A\text{-}1)$$

can be linearized to give

$$j = (\alpha_a + \alpha_c)(ZF/RT)\, j_o\eta_s \qquad (A\text{-}2)$$

where Z is the charge on the sodium ion, F is the Faraday constant, and

α_a and α_c are transfer coefficients for the anodic and cathodic reactions, respectively. Since the reduction of sodium ions to sodium is probably a simple reaction, it should be expected that $(\alpha_a + \alpha_c) = 1$ (Ne 73). Then it was necessary to determine the exchange current density experimentally.

Two experimental determinations of the surface overpotential, or of the surface resistance $r_s = j/\eta_s$, are described in section 2.6. The surface overpotential in each case was plotted vs. the current, and the slope of this plot gave a surface resistance. For the first experiment, $r_s = 9.5 \times 10^{-7}$ ohm·m^2 $\pm$ 5×10^{-7} ohm·m^2 was found with low frequency alternating current. This surface resistance is probably due to an impurity such as Ca^{2+}, K^+, or H_2O that collects at the surface when current is passed. The reaction $Na^+ + e^- = Na$ is probably too fast for measurement by this method, as the process observed did not occur at frequencies as low as 25 Hz. Very high frequencies would have to be used in order to observe the reduction or oxidation of sodium, making the measurement much more difficult.

Cell resistances were also determined for electrodes containing oxygen, and for electrodes from which the oxygen had been removed by the introduction of reactive metals such as vanadium. Then the difference in resistance was attributed to the removal of a sodium oxide film from the interface. The log of the cell resistance was plotted vs. 1/T, Figure A.2, and for the thick cell there was a slight drop in resistance, mainly at high temperature. The thin cell showed a more substantial decrease in resistance, from about 20% at 200° centigrade to about 50% at 400° centigrade. The resistance was about the same for all three

additives, with vanadium reducing the resistance slightly more than manganese, and titanium reducing the resistance slightly more than either manganese or vanadium. The reduction in surface resistance at 300°C was 1.05×10^{-5} ohm·m^2 for the thick cell and 2.25×10^{-5} ohm·m^2 for the thin cell.

Then the parameters used in the numerical calculations were the various cell geometries and dimensions; and the electrolyte conductivity, K = 25 (ohm·m)$^{-1}$, and the surface resistances measured above, which determine the dimensionless exchange current density:

$$J = 1/r_s K \tag{A-3}$$

Once the current distribution was found, the integral in equation (4.1) could be evaluated numerically, leading to an integrated expression of the form

$$P_s = \exp[-A/A_o(j/j_o^n)C] \tag{A-4}$$

where C is a function of the current distribution, and thus of the cell geometry, size, surface resistance and electrolyte conductivity; and of the Weibull modulus, n. For a uniform current distribution (or for n = 1), C = 1. Then, considering cell with a uniform current density j, with all other factors identical, one would have

$$P_s(\text{uniform}) = \exp[-A/A_o(j/j_o)^n] \tag{A-5}$$

or, combining Eq. (A-4) and (A-5)

$$P_s(\text{uniform}) = P_s^{1/C} \tag{A-6}$$

or if the current density of the cell with uniform current density is adjusted to give the same failure probability as the cell of (A-4)

$$j\,(\text{uniform}) = j\,C^{1/n} \qquad \text{(A-7)}$$

Then in a Weibull plot the values of ln ln $1/P_s$ for a cell of nonuniform current distribution will all be lower than the values for a cell of uniform current distribution by the same factor, ln C.

Values of $C^{1/n}$ for the cell of Fig. A.1A were calculated for various values of n, L, h/L, and J. The results are shown in Figures A.3, A.4 and A.5. Figure A.3 shows that $C^{1/n}$ increases as n increases, and the rate of increase is greater for large values of J. Figures A.4 and A.5 show that $C^{1/n}$ increases with increasing L and h/L, and the increase is greater for larger n.

Figures A.6 and A.7 give the values of $C^{1/n}$ determined for the cell geometries of Fig. A.1B and A.1C. respectively, for various values of n and J. Again $C^{1/n}$ increases with increasing n and J.

A calculation of the primary current distribution on a sodium filled crack by Feldman and De Jonghe (Fe 82) gives a current density at the crack tip of

$$j(\text{tip}) = jl/r \qquad \text{(A-8)}$$

where l is the crack length, and r is half the crack opening displacement. However, particularly for small objects the secondary current distribution is much more uniform than the primary, so the secondary current distribution was calculated for a surface resistance of 10^{-6} ohm·m^2, the smallest of the measured surface resistances. Then for any larger surface resistance the current distribution will be even more uniform. For a crack of length 10 micrometers, with a crack opening displacement of 6.32 nm, the primary current density from the equation of

Feldman and De Jonghe, and the secondary current distribution calculated numerically were calculated and are compared in Figure 5.2. The current density at the crack tip is 3.17×10^3 times the average current density for the primary current distribution, while the secondary current distribution predicts a current density 1.1 times the average current density. Also the primary current distribution depends strongly on the crack opening displacement and the crack shape, while the secondary current distribution is independent of these for crack length much greater than crack width.

REFERENCES

Al 81 Alden, M., J.O. Thomas and G.C. Farrington, Solid State Ionics 5, 205 (1981).

An 81 Anstis, G.R., P. Chantikul, B.R. Lawn and D.B. Marshall. J. Amer. Ceram. Soc., vol. 64, no. 9, 533-38 (1981).

Ar 80 Archer, W.I., R.D. Armstrong, D.P. Sillick, W.G. Budgen and J.H. Duncan. J. Mat. Sci., vol. 15, 2066 (1980).

Ba 84 Battles, J. Private Communication, Argonne National Laboratory, May 1984.

Ar 74 Armstrong, R.D., T. Dickinson and J. Turner. Electrochim. Acta, vol. 19, 187 (1974).

Be 36 Beevers, C.A. and S. Brohult. Z. Kristallogr., vol. 95, 472 (1936).

Be 37 Beevers, C.A. and M.A.S. Ross. Z. Kristallogr., vol. 97, 59 (1937).

Be 63 Berker, R. in "Handbuch der Physik" Vol. 802, ed. S. Fluegge (Springer-Verlag, Berlin, 1963).

Be 69 Bettman, M. and C.R. Peters. J. Phys. Chem., vol. 73, no. 6, 1774-80 (1969).

Bi 76 Birk, J. and R Whitaker. Electric Power Research Institute Journal, vol.1, no. 8, 6-13 (1976).

Bo 80 Boilot, J.P., G. Collin, Ph. Colomban and R. Comes. Phys. Rev. B, vol. 22, no. 12, 5912-23 (1980).

Br 31 Bragg, W.L.,C. Gottfried and J. West. Z. Krist., vol. 77, 255 (1931).

Br 80a Brennan, M.P.J. Electrochim. Acta, vol. 25, No. 5, 621-627 (1980).

Br 80b Breiter, M.W., B. Dunn and R.W. Powers. Electrochim. Acta, vol. 25, 613-616 (1980).

Br 81 Brown, G.M., D.A. Schwinn, J.B. Bates and W.E. Brundage. Solid State Ionics 5, 147 (1981).

Bu 79 Buechele, A.C. and L.C. De Jonghe. Am. Ceram. Soc. Bull., vol. 58, no. 9, 861-4 (1979).

Bu 83 Buechele, A.C., L.C. De Jonghe and D. Hitchcock. J. Electrochem. Soc., vol. 130, no. 5, 1042-9 (1983).

Ca 82 Cameron, C. Unpublished research, Lawrence Berkeley Laboratory, Berkeley, California (1982).

Da 79a Davidge, R.W., G. Tappin, J.R. McLaren and G.J. May. Amer. Ceram. Soc. Bull., vol. 58, no. 8, 771-774 (1979).

Da 79b Davidge, R.W. "Mechanical Behaviour of Ceramics," (Cambridge University Press, Cambridge, 1979)

De 69 De Vries, R.C. and W.L.Roth. J. Amer. Ceram. Soc., vol. 52, no. 7, 364-9 (1969).

De 76 De Jonghe, L.C. J. Mater. Sci., vol. 11, 206-8 (1976).

De 77 De Jonghe, L.C. "Substructure and Properties of Beta Alumina Solid Electrolytes," EPRI Rept. EM-494, 1977.

De 80 De Jonghe, L.C., and L. Feldman. Mat. Res. Bull., vol. 15, no. 6, 777-82 (1980).

De 82a De Jonghe, L.C. and A Buechele. J. Mater. Sci., vol. 17, 885-92 (1982).

De 82b De Jonghe, L.C. Solid State Ionics 7, 61-4 (1982).

De 82c De Jonghe, L.C., A. Buechele and K.H. Yoon. Lawrence Berkeley Laboratory Report LBL-1115, June 1983.

Du 81 Dunn, B. J. Am. Ceram. Soc., vol. 64, no. 3, 125-8 (1981).

Ev 76 Evans, A.G. and E.A. Charles. J. Am. Ceram. Soc., vol. 59, no. 7-8, 371-72 (1976).

Ev 78 Evans, A.G. Acta Met., Vol. 26 1845-1853 (1978).

Fa 73 Fally, J., C. Lasne, Y. Lazennec, and P. Margotin. J. Electrochem. Soc., vol. 120, no. 10, 1292-95 (1973).

Fa 76 Farrington, G.C. J. Electrochem. Soc., vol. 123, 591 (1976).

Fe 82 Feldman, L. A. and L.C. De Jonghe. J. Mater. Sci., vol. 17, 517-24 (1982).

Fi 81 Fischer, W. Solid State Ionics, Vol. 3/4, 413-24 (1981).

Fl 84 Flinn, J. San Francisco Examiner, p. B-1, April 29, 1984.

Ga 78 Galambos, J. "The Asymptotic Theory of Extreme Order Statistics," (John Wiley & Sons, New York, 1978).

Ga 81 Garbarczyk, J., W. Jakubowski and M. Wasiucionek. Szklo Ceram., vol. 32, no. 5-6, 83-6 (1981).

Gr 84 Green, D.J. "Improved Beta"-Aluminum Oxide Electrolytes Through Transformation Toughening," Final Report Draft for the period July 1, 1983 through June 30, 1984, subcontract no. 4523010, Rockwell Science Center, May, 1984.

He 82 Heavens, S.N. J. Mater. Sci., vol. 17, no. 4, 965-9 (1982).

He 83 Hellstrom, E.E. and R.E. Benner. Solid State Ionics 11, 125-32 (1983).

Ho 83 Hodge, J.D. J. Amer. Ceram. Soc., vol. 66, no. 3, 166- 9 (1983).

Hs 78 Hsieh, M.Y. and L.C. De Jonghe. J. Amer. Ceram. Soc., vol. 61, no. 5-6, 185-91 (1978).

Iw 80 Iwabuchi, S. and S. Hattori. 82-98 in Ta 80.

Ku 72 Kummer, J.T. Progress in Solid State Chemistry, vol. 7, p. 146, ed. J.O. McCaldin (Pergammon Press, New York, 1972).

Kv 81 Kvachkov, R., A. Yanakiev, C.N. Poulieff, I. Balkanov, P.D. Yankulov and E. Budevski. J. Mater. Sci., vol. 16, no. 10, 2710-16 (1981).

La 75a Lazennec, Y., C. Lasne, P. Margotin and J. Fally. J. Electrochem. Soc., vol. 122, no. 6, 734-737 (1975).

La 75b Lawn, B.R., and T.R. Wilshaw, "Fracture of Brittle Solids" (Cambridge University Press, 1975).

Le 72 Le Cars, Y., J. Thery and R. Collongues. Rev. Int. Haute Temp. et Refract., vol. 9, 153-60 (1972).

Le 80 Levine, C.A. pp 99-101 in Ta 80 (1980).

Li 79 Lingscheit, J.N., G.J. Tennenhouse and T.J. Whalen. Am. Ceram. Soc. Bull., vol. 58, no. 5, 536-8 (1979).

Li 84 Liu, M.L. Research in progress, Lawrence Berkeley Laboratory, Berkeley, California (1984).

Ma 76 Mahan, G.D. and W.L. Roth. "Superionic Conductors," (Plenum Press, 1976).

Ma 82 Marshall, D.B., T. Noma and A.G. Evans. J.Am. Ceram. Soc., vol. 65, no. 10, C-175-C-176 (1982).

Mi 79 Miller, M.L., B.J. McEntire, G.R. Miller and R.S. Gordon. Am. Ceram. Soc. Bull., vol. 58, no. 5, 522-6 (1979).

Ne 73 Newman, J. "Electrochemical Systems" (Prentice-Hall, Inc., Englewood Cliffs, New Jersey 1973).

Ni 81 Ni, J., Y.T. Tsai and D.H. Whitmore. Solid State Ionics, Vol. 5, 199 (1981).

Pa 70 Parrish, W.R., and J. Newman. J. Electrochem. Soc., vol. 117, no. 1, 43-48 (1970).

Pe 71 Peters, C.R., M. Bettman, J.W. Moore and M.D. Glick. Acta Cryst., vol. B27, 1826-34 (1971).

Ra 70 Radzilowski, R.H. J. Am. Ceram. Soc., Vol. 53, No 12, 699-700 (1970).

Ra 16 Rankin, G.A. and H.E. Merwin. J. Am. Chem. Soc., vol. 38, 568-88 (1916).

Ri 75 Richman, R.H., and G.J. Tennenhouse. J. Amer. Ceram. Soc., vol. 58 63 (1975).

Ri 36 Ridgway, R.R., A.A. Klein and W.J. O'Leary. Trans. Electrochem. Soc., vol. 70, 71-88 (1936).

Ro 65 Rolin, M. and P.H. Thanh. Rev. Int. Haute. Temp. et Refract., vol. 2, no. 2, 175-85 (1965).

Ro 76 Roth, W.L., F. Reidinger and S. La Placa. pp. 223-41 in Ma 76.

Sa 82 Saxton, H.J. Trip Report, Visit to United Kingdom, Germany, and France, Sept 15 to Oct. 15, 1982, Power Sources Department, Sandia National Laboratories, Albuquerque.

Sh 77 Shetty, D.K., A.V. Virkar and R.S. Gordon, "Electrolytic Degradation of Beta"-Alumina," 651-665 in Fracture Mechanics of Ceramics Vol. 4, ed. R.C. Bradt, D.P.H. Hasselman and F.F. Lange (Plenum, 1977).

Ta 73 Tada, H. "The Stress Analysis of Cracks Handbook," (Del Research, St. Louis, 1973).

Ta 80 Takahashi, T. and A. Kozawa (eds.), "Applications of Solid Electrolytes," (Cleveland, Ohio, JEC Press, 1980).

Ta 82 Takikawa, O., A. Imai and M. Harata. Solid State Ionics vol. 7, 101-107 (1982).

Te 75 Tennenhouse, G.J., R.C. Ku, R.H. Richman, and T.J. Whalen. Am Ceram. Soc. Bull., vol. 54, no. 5, 523-27, 531 (1975).

Th 62 Thery, J. and D. Briancon. Compt. Rend., vol. 254, 2782-4 (1962).

Th 83 Thery, J. and A.M. Lejus, Mater. Res. Bull., vol. 18, no. 4, 481-90 (1983).

To 39 Toropov, N.A. and M.M. Stukalova. Compt. Rend. Acad. Sci. U.R.S.S., vol. 24, 459-61 (1939).

To 40 Toropov, N.A. and M.M.Stukalova. Compt. Rend. Acad. Sci. U.R.S.S., vol. 27, 974-7 (1940).

Tr 81 Trantina, G.G. J. Am. Ceram. Soc., Comm., vol. 64, no. 3, C48-C51, (1981).

Un 77 Unertl, W.N., L.C. De Jonghe and Y.Y. Tu. J. Mat. Sci., vol. 12, no. 4, (1977).

Vi 77 Virkar, A.V., and R.S. Gordon. J. Am. Ceram. Soc., vol. 60, no. 1-2, 58-61, (1977).

Vi 80 Virkar, A.V., L. Viswanathan and D.R. Biswas. J. Mater. Sci. vol. 16, 302 (1980).

Vi 81 Virkar, A.V. J. Mater. Sci., vol.16, 1142-1150 (1981).

Vi 82 Viswanathan, L. and Virkar, A.V. J. Mater. Sci., vol. 17, 753-59 (1982).

Vi 83 Virkar, A.V. and L. Viswanathan. J. M,ater. Sci., vol. 18, 1202-1212 (1983).

Wa 57 Wagner, C. pp. 361-77 in "International Committee of Electrochemical Thermodynamics and Kinetics, Proceedings of the 7th meeting, Lindau, 1955" (Butterworth Scientific Publications, London, 1957).

Wa 79 Wayne, M. Electric Power Research Institute Journal, vol. 4, no. 9, 6-15 (1979).

Wa 80 Wang, J.C. J. Chem. Phys., vol. 73, no. 11, 5786-95 (1980).

Wa 81 Wang, J.C., J.B. Bates, N.J. Dudney and H. Engstrom. Solid State Ionics 5, pp. 35-40 (1980).

We 67 Weber, N., and J.T. Kummer. 21st Power Sources Symposium Proceedings, 37-9 (1967).

We 74 Weber, N. Energy Conversion vol.14, 1-8 (1974).

Wh 71 Whittingham, M.S. and R.A. Huggins. J. Electrochem. Soc., vol. 118, no. 1, 1-6 (1971).

Wh 74 Whalen, T.J., G.J. Tennenhouse and C. Meyer. J. Amer Ceram. Soc., vol. 57, no. 11, 497-8 (1974).

Wo 78 Worrell, C.A. and B.A.W. Redfern. J. Mater. Sci., vol. 13, 1515 (1978).

Wi 59 Williams, D.D., J.A. Grand and R.R. Miller. J. Phys. Chem., vol. 63, 68 (1959).

Ya 68 Yamaguchi, G. and K. Suzuki. Bull. Chem. Soc. Japan, vol. 41, 93 (1968), cited in Be 69.

Ya 80 Yasui, I. and T. Hattori, pp. 113-5 in Third Int. Mtg. on Solid Electrolytes-Solid Ionics and Galvanic Cells, Extended Abstracts, Tokyo, Japan, Sept. 15-19, 1980.

Table 1.1 Effect of Changes in Mobile Ion on Lattice Parameters of Beta"- Alumina

	Lattice Parameters, angstroms (Reference)			
	Lithia-stabilized polycrystal		Magnesia-stabilized single crystal	
Ion	a_o	c_o	a_o	c_o
Na	5.610	33.655 (He 83)	5.623	33.536 (Br 81)
K	5.610	34.048 (He 83)	5.625	34.067 (Br 81)
Ca	5.599	33.497 (He 83)	5.624	33.334 (Al 81)

Table 3.1. Analyses of cell 5/73 with large grains.

Region	Composition, Weight Per Cent, and (Precision, two standard deviations) Al	Na	Ag
Large grain, above the void.	99.96 (3.00)	-	31.70 (3.11)
Large grain, to the right of the void.	99.98 (2.00)	-	21.07 (2.11)
Below the void.	99.99 (1.80)	20.19 (2.34)	17.43 (1.67)
Fine grain region, 200 microns to the right of the first measurement.	99.99 (2.20)	14.64 (2.69)	18.57 (2.08)

Table 3.2 Analyses of cell 5/37 with silicon-rich inclusion.

Region	Composition, Weight Per Cent, and (Precision, two standard deviations) Al	Na	Ag	Si	Ca	Cl
Inclusion	6.31 (0.54)	9.40 (1.24)	61.12 (1.22)	4.67 (0.45)	- -	18.50 (0.44)
Near Inclusion	48.24 (0.58)	18.99 (0.57)	- -	32.10 (0.58)	0.67 (0.18)	- -
Bulk of Electrolyte	90.90 (0.73)	3.25 (0.44)	5.85 (0.61)	- -	- -	- -

Table 5.1. Values of Hardness and Elastic Modulus Determined from Surface Indents.

Plane of Indentation	H/E	H(GPa)	E(GPa)
Basal	0.0632	13.59	215 (E1)
Prismatic	0.0465	8.1	174 (E2)

Table 5.2. Fracture Toughness Values.

Material	Plane of indentation	Kc(MPa.$m^{1/2}$)	Std. deviation
Beta Single Crystal	Prismatic	0.162	0.067
Beta Single Crystal	Basal	1.973	0.232
Beta" Polycrystal		1.984	0.226

FIGURE CAPTIONS

Fig. 1.1. Crystal Structures of Beta and Beta" Alumina

Fig. 1.2. Phase Diagram of the Al_2O_3-Rich Portion of the System Al_2O_3-Na_2O. Beta" alumina exists as a metastable phase in the shaded region.

Fig. 1.3. Conduction Plane of Beta Alumina. Triangles are oxygen, open squares are sodium on Beevers-Ross sites, solid squares are sodium on mid-oxygen sites, crosses are vacant anti-Beevers-Ross sites. A Roth defect is enclosed by the dashed line.

Fig. 1.4. "Roth Defect"

Fig. 1.5. Conduction Plane of Beta" Alumina. Solid squares are sodium on mid-oxygen sites, open squares are sodium on anti-Beevers-Ross sites, crosses are vacant anti-Beevers-Ross sites, and the dashed line outlines a cell of the superlattice on which the vacancies are ordered.

Fig. 1.6. Low Angle Tilt Boundary. Lines represent spinel blocks, arrows show sodium ion paths through conduction planes converging at grain boundary.

Fig. 2.1. Low (left) and high (right) magnification polished, H_3PO_4 etched sections of Ceramatec electrolyte. (A) Fine grain size. (B) Large grain size.

Fig. 2.2. Surface Pore in Ceramatec Beta" Alumina.

Fig. 3.9. Scanning electron micrograph of crack shown in Fig. 3.8.

Fig. 3.10. Higher magnification od lower end of crack first shown in Fig. 3.8.

Fig. 3.11. (A) Crack intersecting the plane of sectioning, SEM. (B) Higher magnification of right end.

Fig. 3.12. Crack passing through plane of sectioning, (A) SEM, (B) silver stained, optical.

Fig. 3.13. (A) Crack of Fig. 3.12. (B) Arrowed region in (A) at higher magnification.

Fig. 3.14. Scanning electron micrographs of (A) electrolytic degradation and (B) fracture surfaces.

Fig. 3.15. Ford electrolyte, 592 Ah/cm^2.

Fig. 3.16. Ford electrolyte, 602 Ah/cm^2.

Fig. 3.17. Surface layer of electrolyte first shown in Fig. 3.2.

Fig. 3.18. Surface Layer, British Railway Electrolyte, Normal Grinding and Polishing.

Fig. 3.19. Surface Layer, Same Electrolyte as Fig. 3.18, Gentle Grinding and Polishing.

Fig. 3.20. Degradation on sodium exit, but not on sodium entrance side of CGE electrolyte. M marks mounting media.

Fig. 3.21. Sodium exit surface of sodium/sodium cell, cracks are visible at the boundaries of large grains after staining.

Fig. 3.22. Polished, stained cross section of electrolyte shown in Figure 3.21. An extremely dark layer indicating the presence of degradation is visible on the exit side (B), but only a chemically darkened layer (A) on the entrance side.

Fig. 3.23. Polished, stained cross section of British Railway electrolyte. Annular crack is indicated by arrows.

Fig. 3.24. Cracks parallel to interface of electrolyte first shown in Fig. 3.23.

Fig. 3.25. Calcium profile and scanning electron micrograph showing crack parallel to interface.

Fig. 3.26. Gently Ground Surface of Electrolyte First Shown in Fig. 3.23.

Fig. 3.27. Surface Layer in Electrolyte Exposed to Humidity.

Fig. 3.28. Polished, Stained Cross Section of Cell E6123.

Fig. 3.29. Surface layer of electrolyte first shown in Fig. 3.28, SEM.

Fig. 3.30. Polished, Stained Section of Cell v69F206.

Fig. 3.31. Microcracks near Surface of Cell v69F206.

Fig. 3.32. Surface Layer after Normal Grinding and Polishing, Cell v69F206.

Fig. 3.33. Polished, Stained Section of Cell E3307.

Fig. 3.34. Surface Layer, Cell E3307, SEM.

Fig. 3.35. Higher Magnification of Surface Layer, Cell E3307.

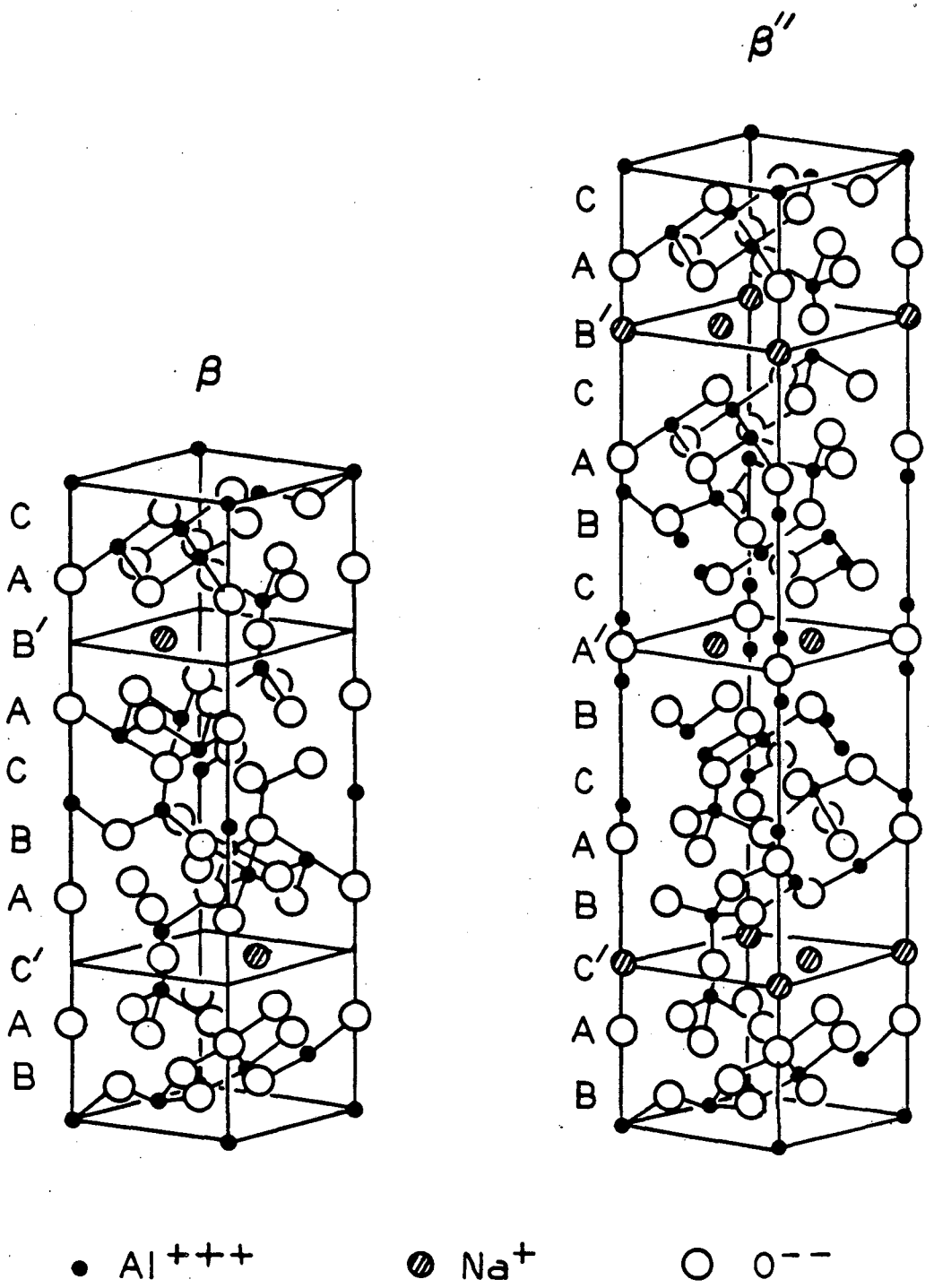

Fig. 1.1

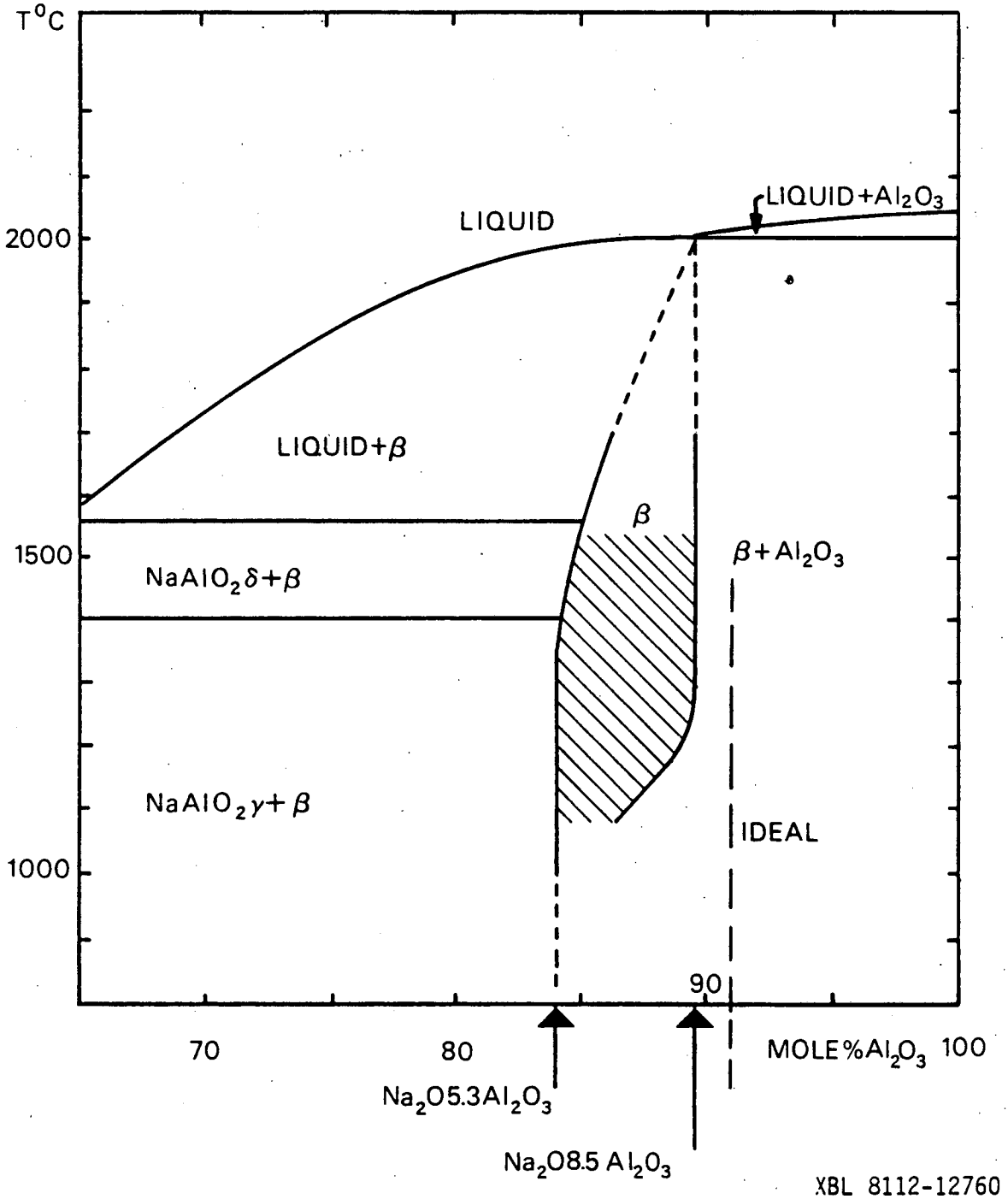
T°C
2000
1500
1000
LIQUID
LIQUID+Al2O3
LIQUID+β
β
β+Al2O3
NaAlO2δ+β
NaAlO2γ+β
IDEAL
90
70
80
MOLE%Al2O3
100
Na2O5.3Al2O3
Na2O8.5 Al2O3
XBL 8112-12760

Fig. 1.2

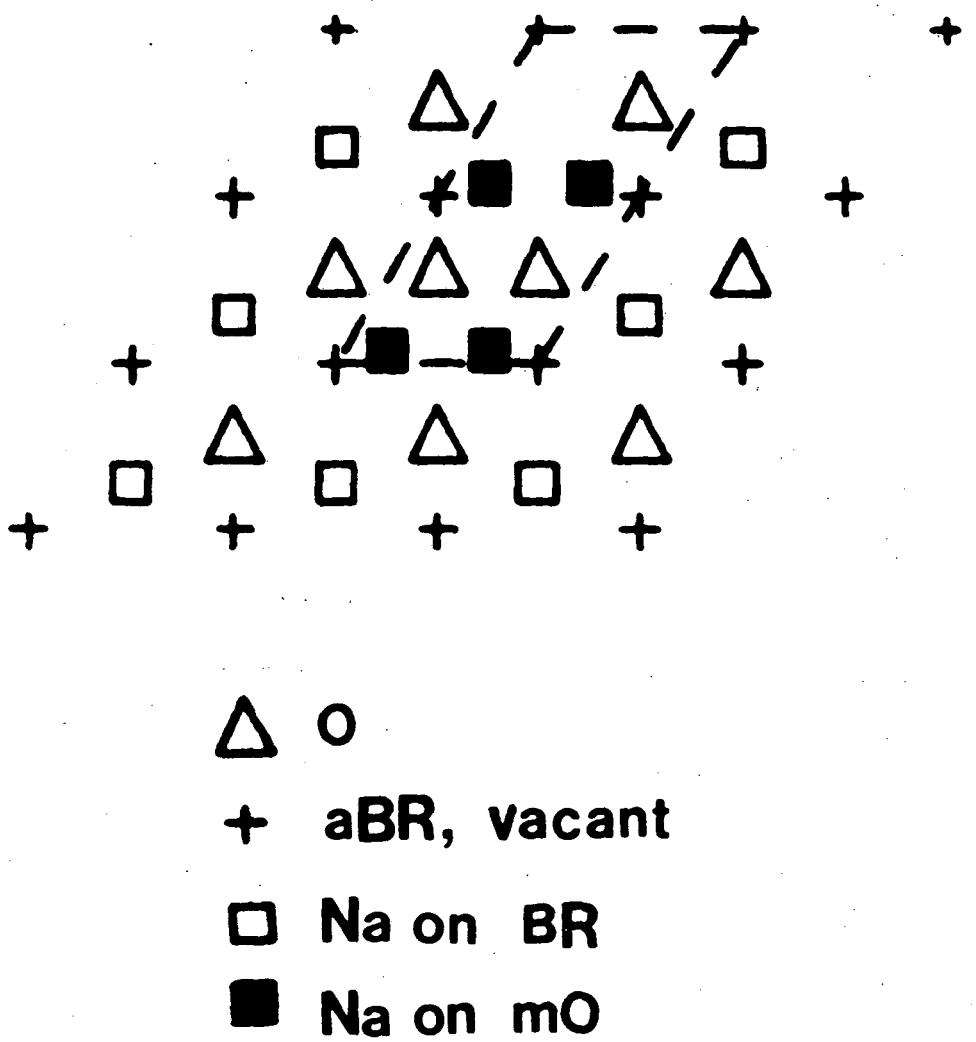

XBL 8411-4777

Fig. 1.3

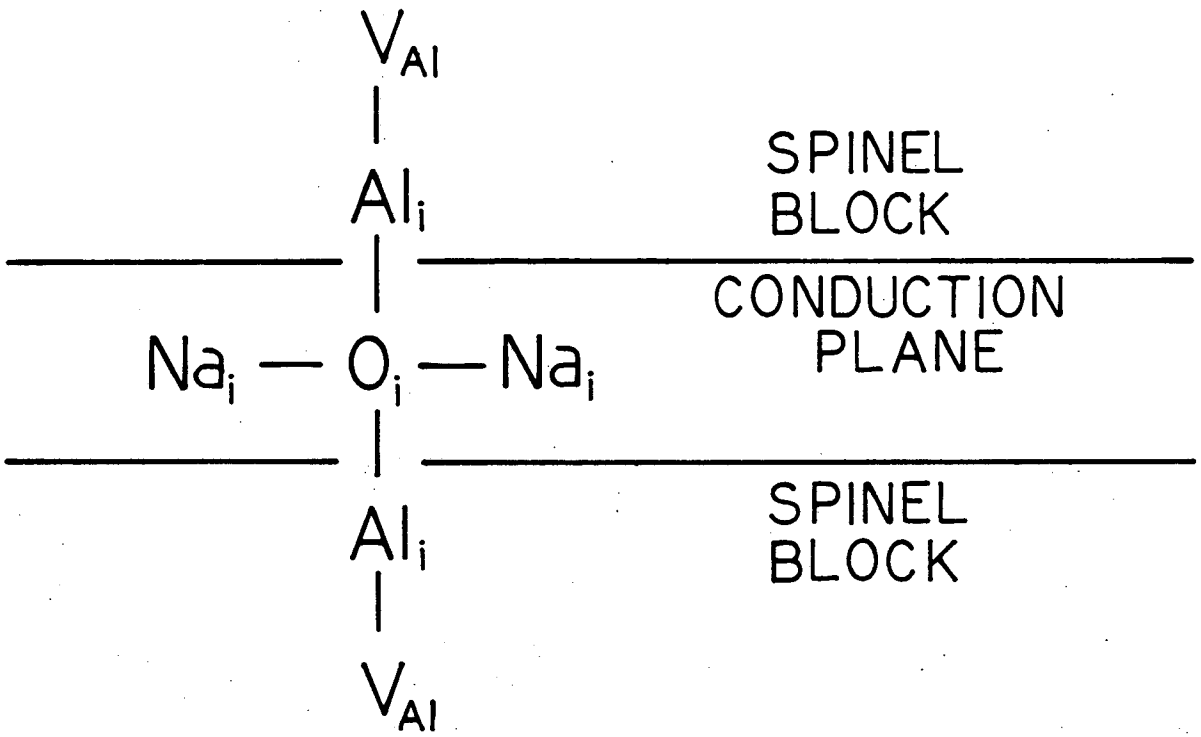
V_{Al}
Al_i
SPINEL BLOCK
CONDUCTION PLANE
$Na_i - O_i - Na_i$
SPINEL BLOCK
Al_i
V_{Al}
XBL 8112-12952

Fig. 1.4

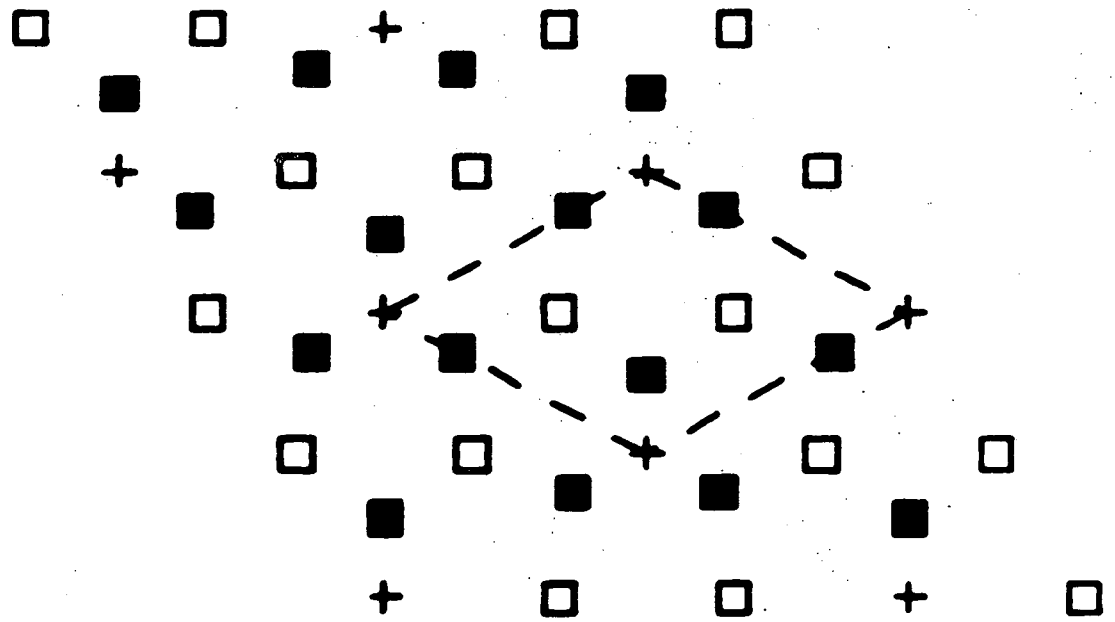

XBL 8411-4774

Fig. 1.5

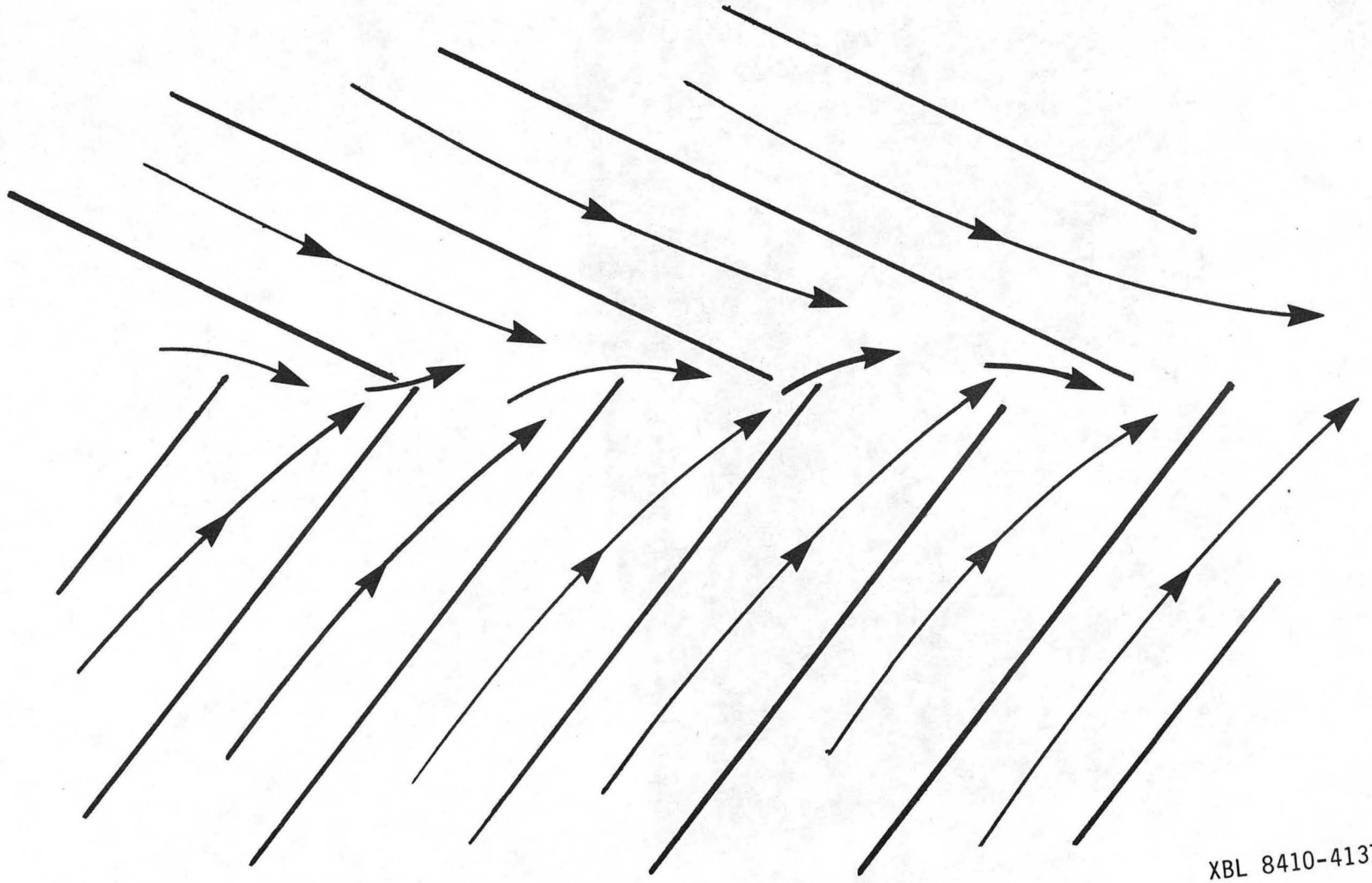

XBL 8410-4137

Fig. 1.6

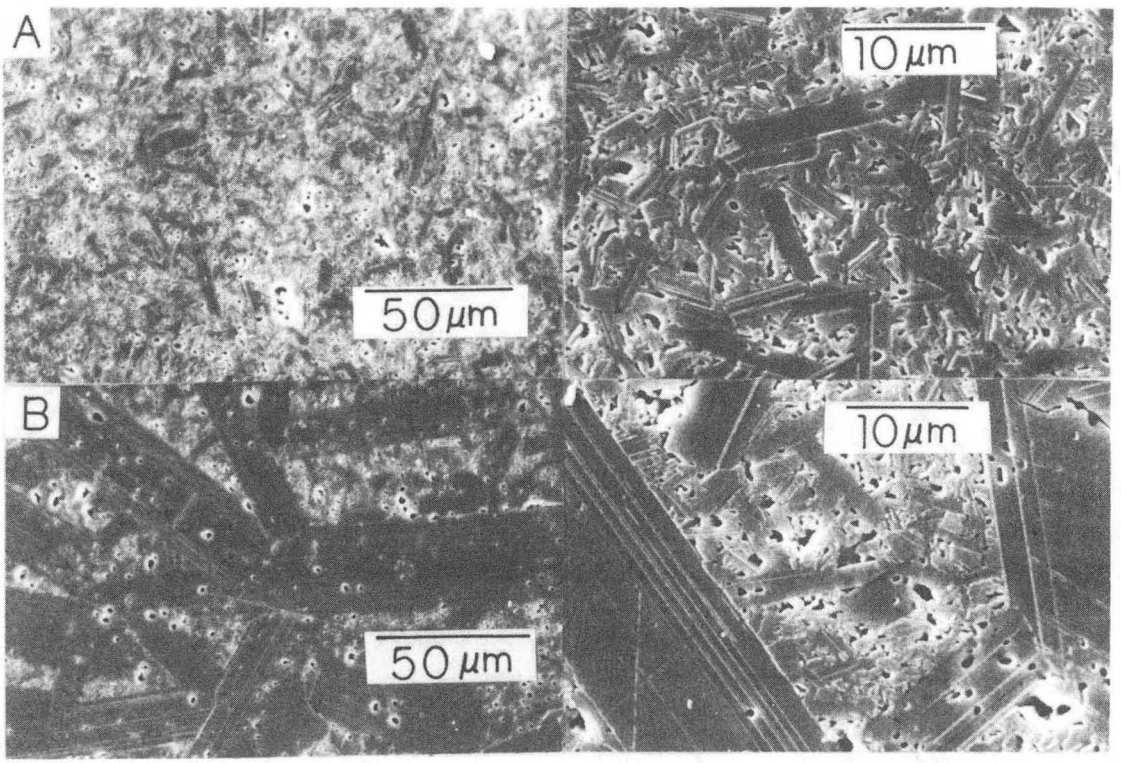

XBB 815-4088

Fig. 2.1

XBB 847-5139

Fig. 2.2

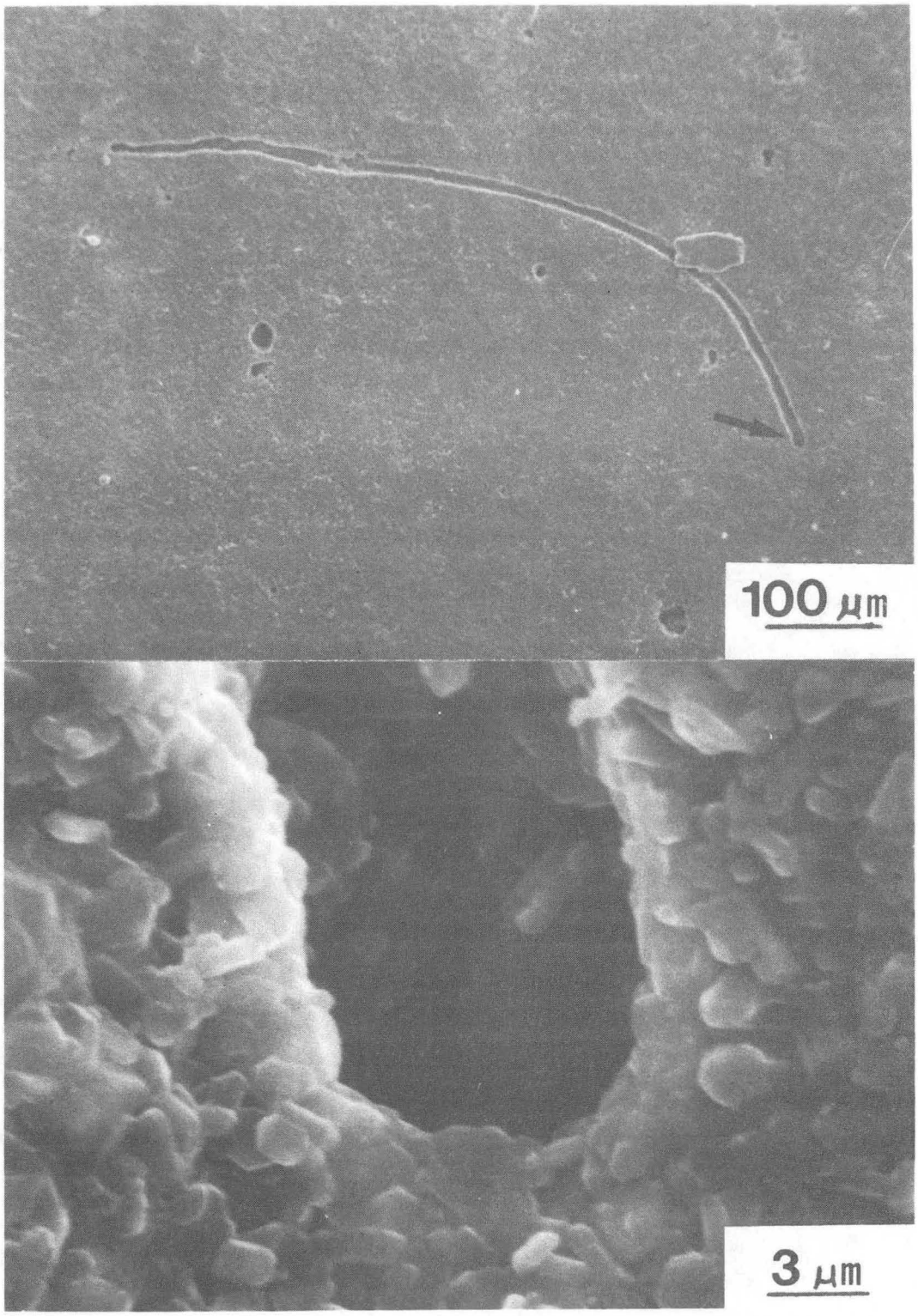

XBB 847-5137

Fig. 2.3

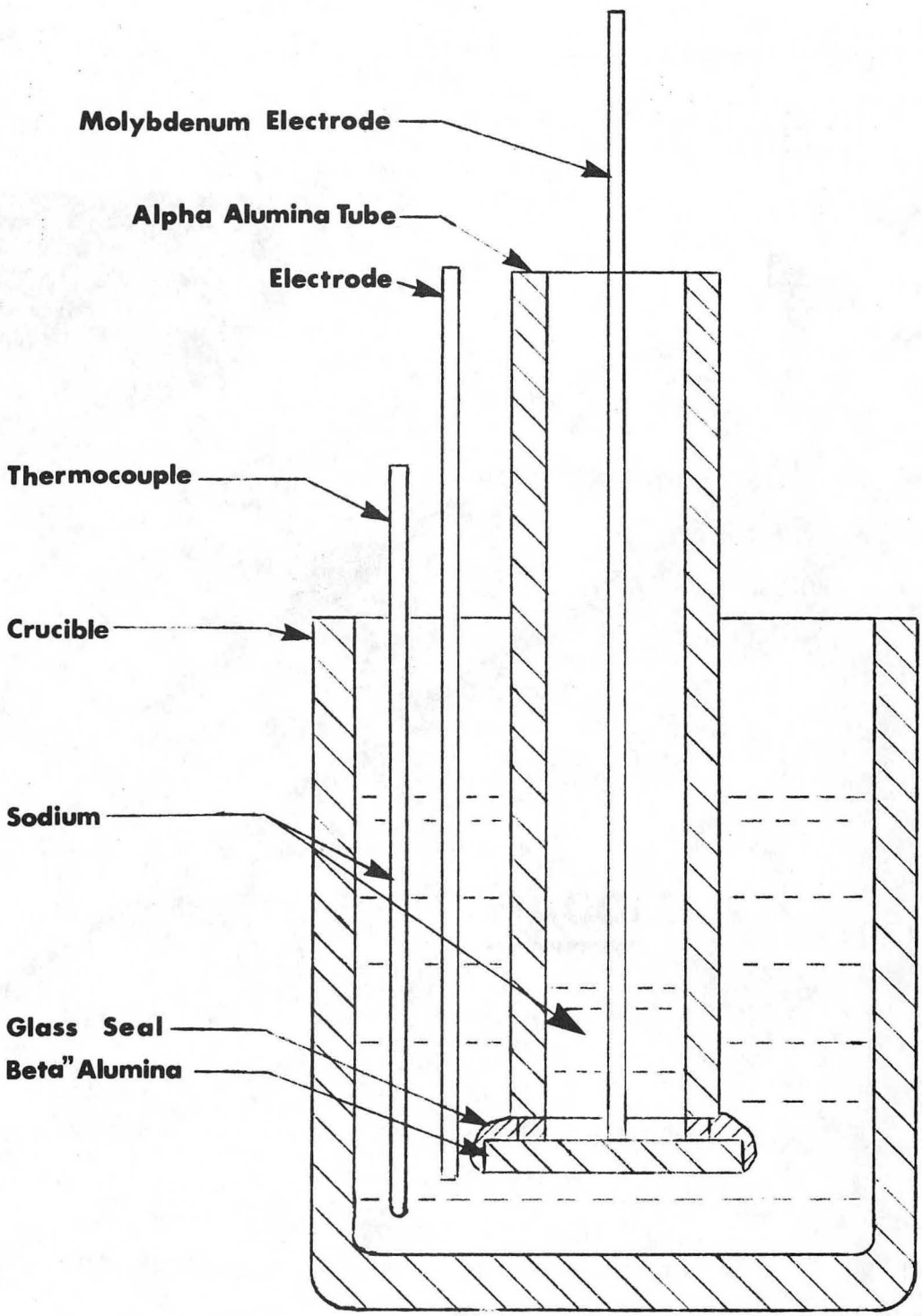
Molybdenum Electrode
Alpha Alumina Tube
Electrode
Thermocouple
Crucible
Sodium
Glass Seal
Beta" Alumina
XBL 845-2002

Fig. 2.4

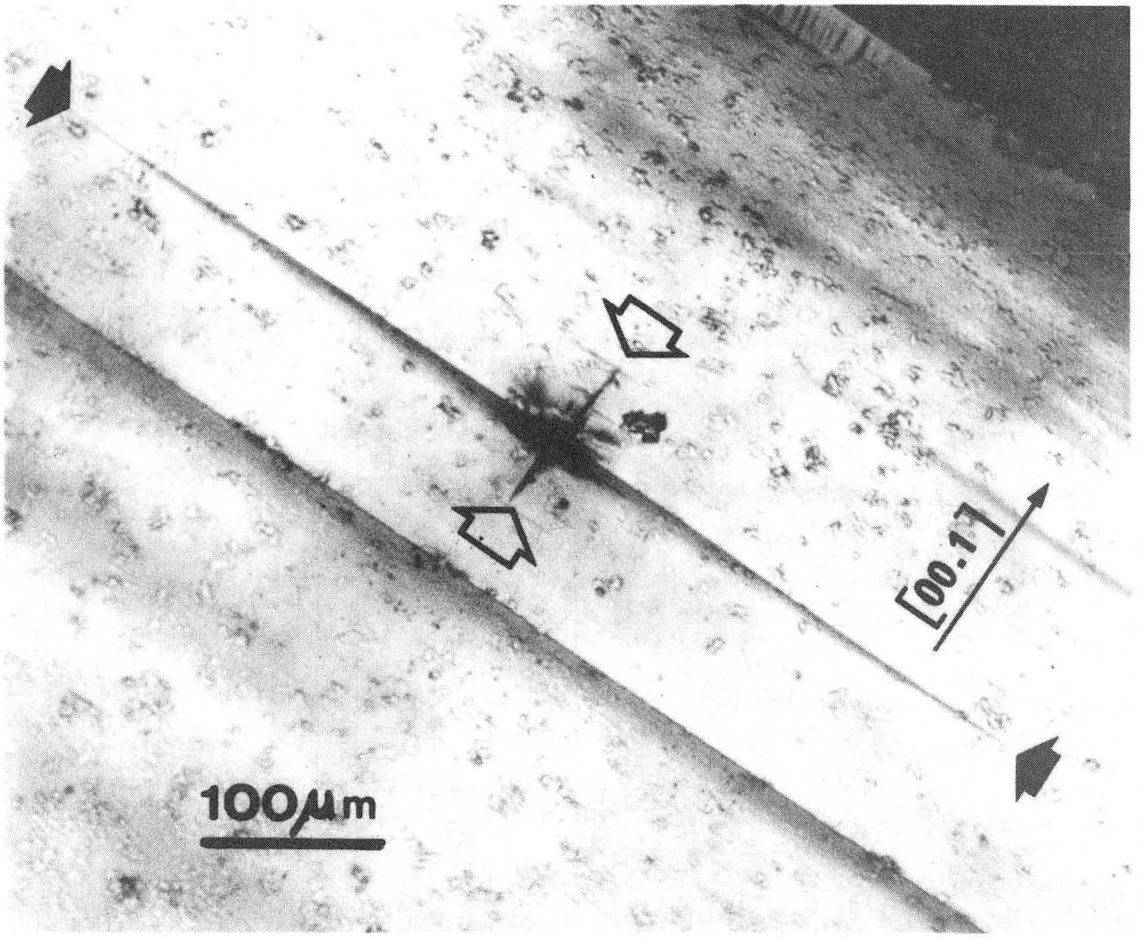

XBB 836-5083

Fig. 2.5

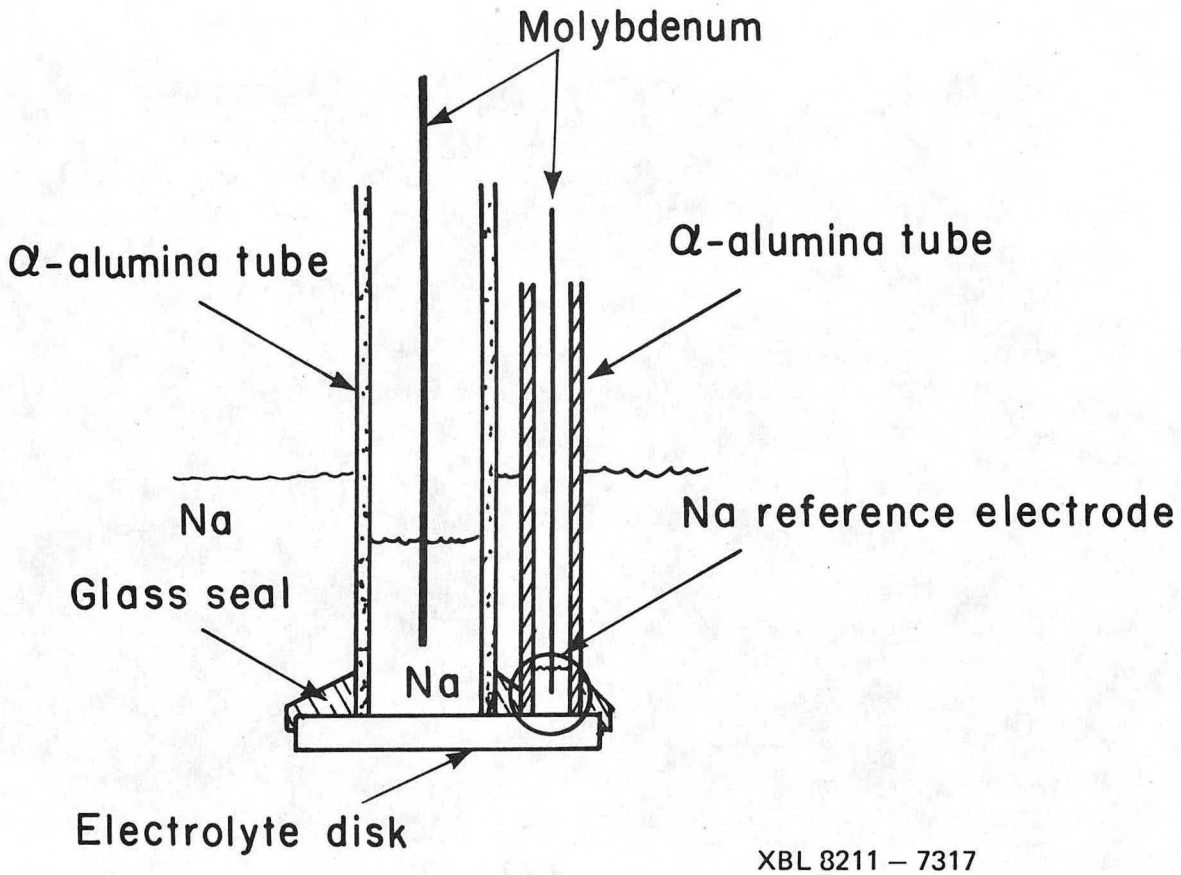
Molybdenum
α-alumina tube
α-alumina tube
Na
Na reference electrode
Glass seal
Na
Electrolyte disk
XBL 8211 – 7317

Fig. 2.6

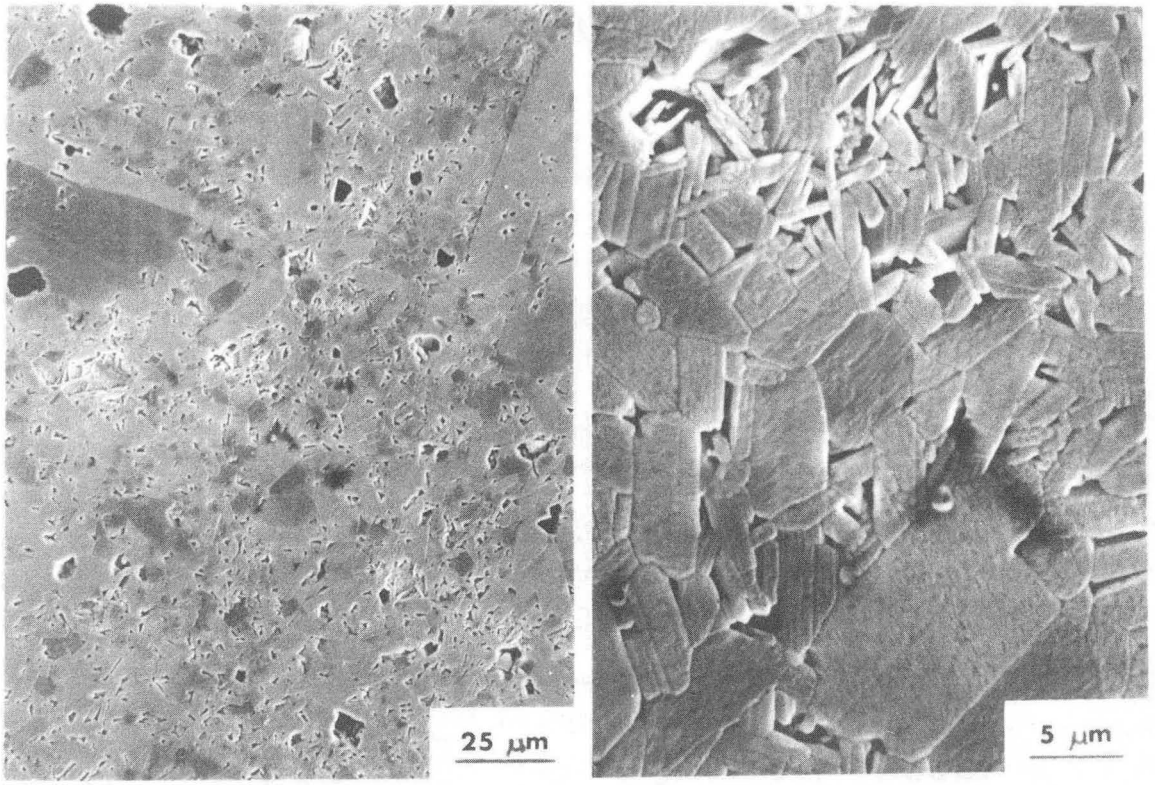

V 69 F 206 XBB 830-9343

Fig. 3.1

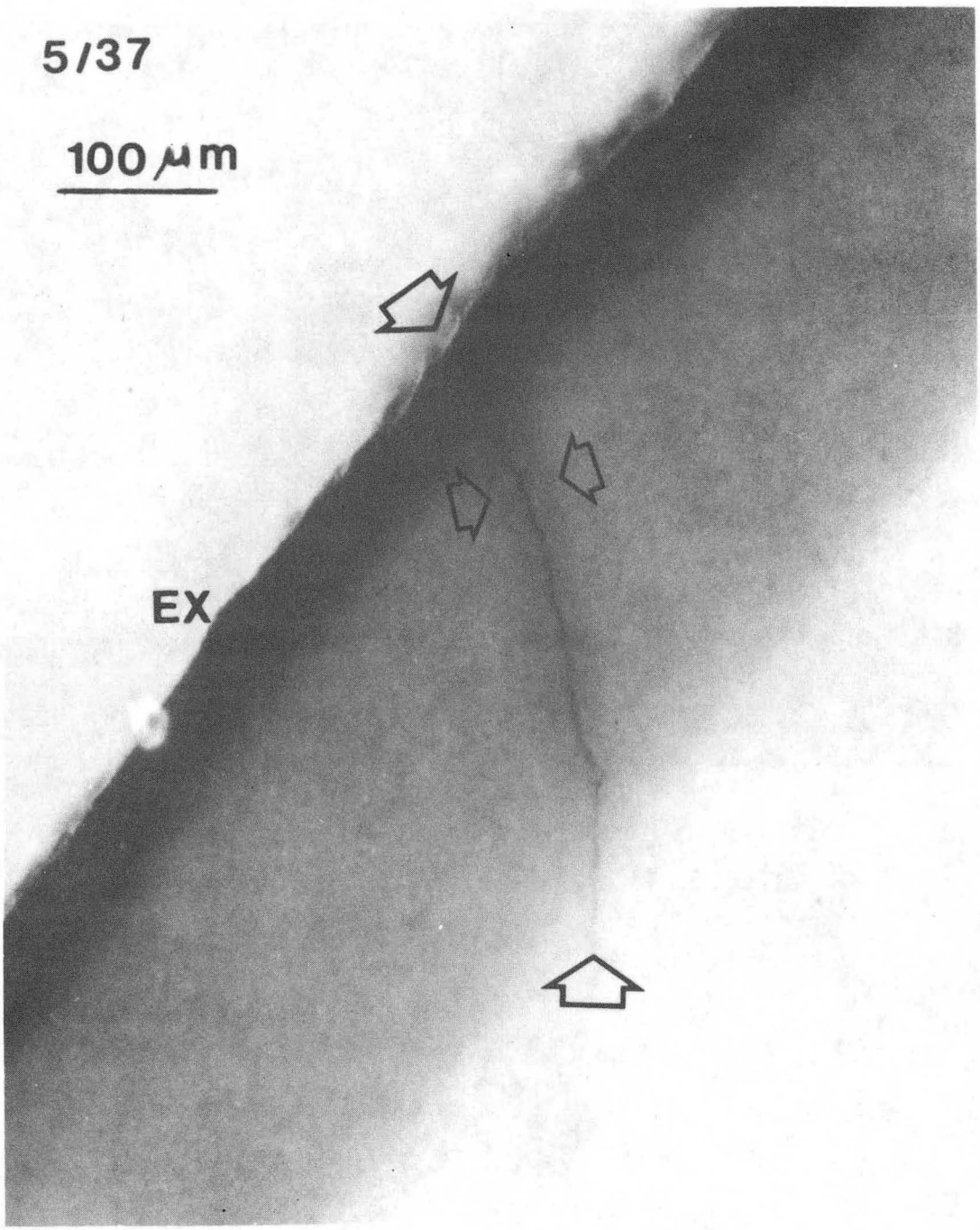

XBB 826-5037

Fig. 3.2

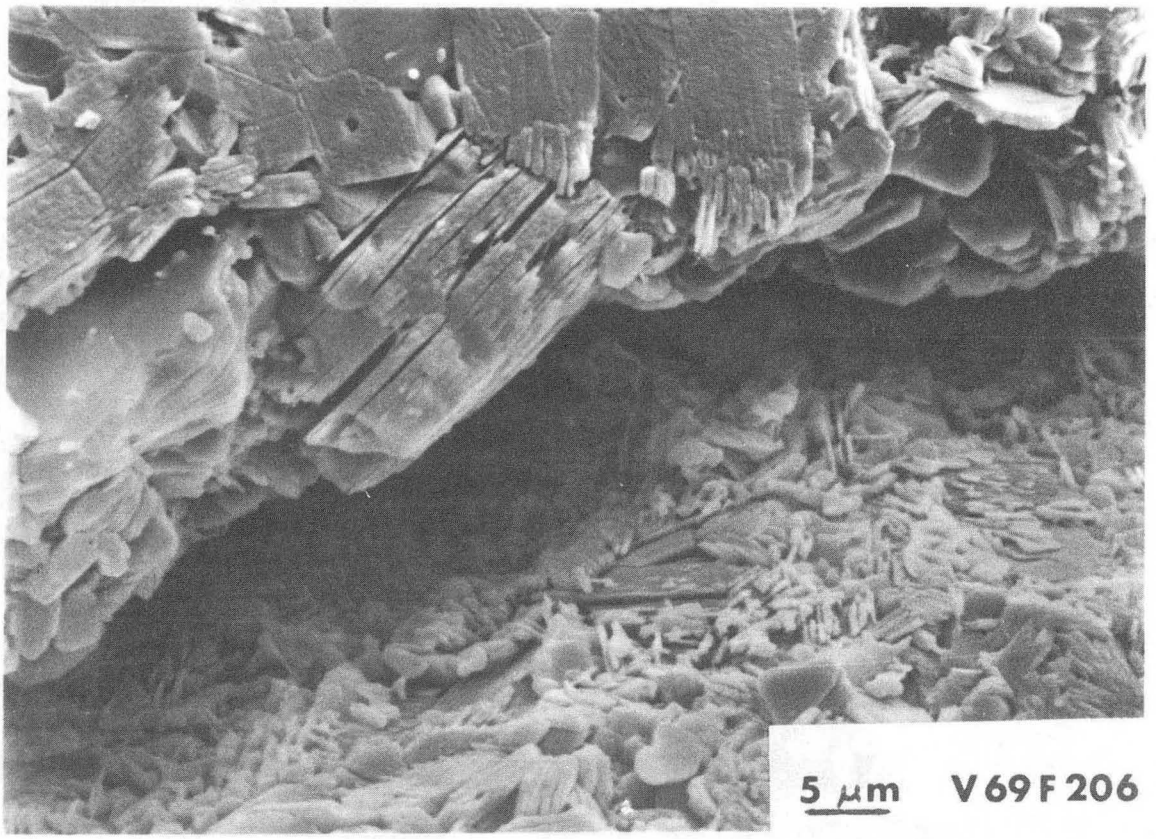

XBB 830-9342

Fig. 3.3

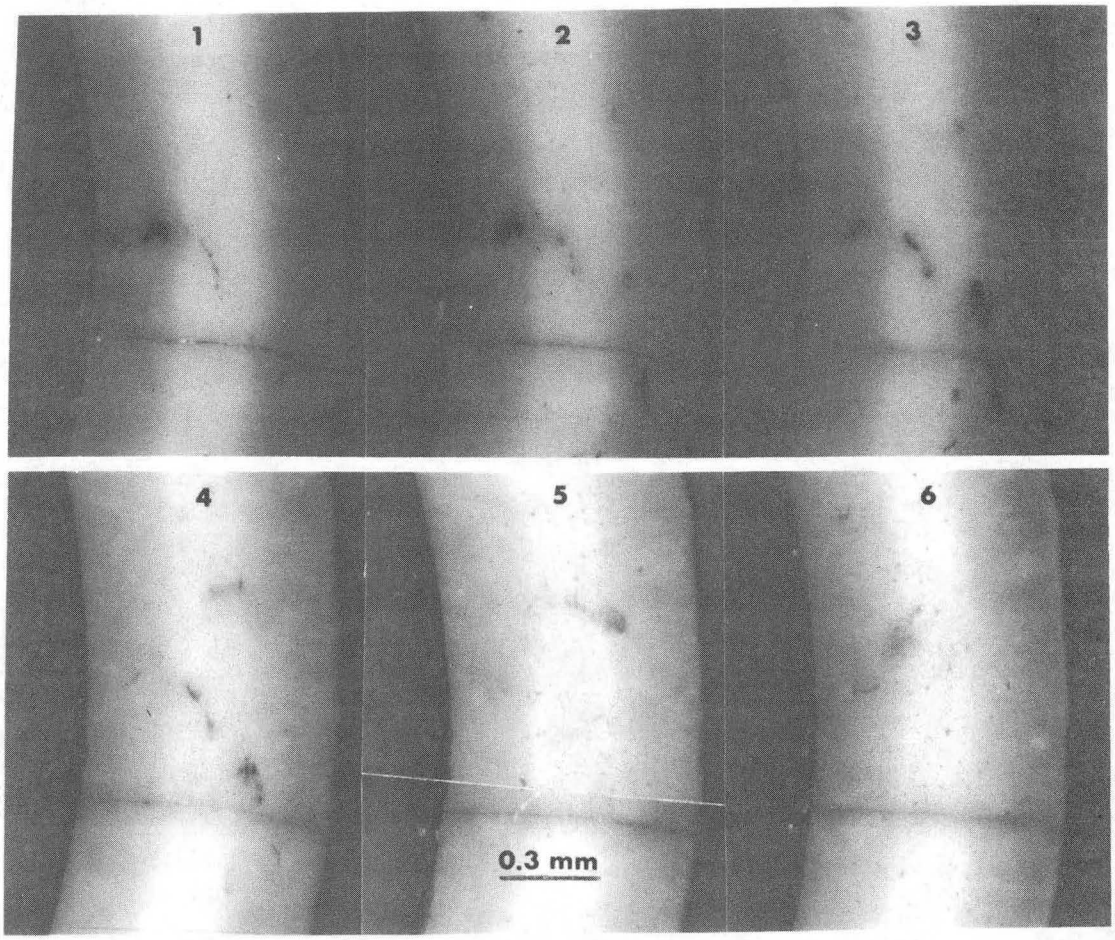

XBB 843-2030

Fig. 3.4

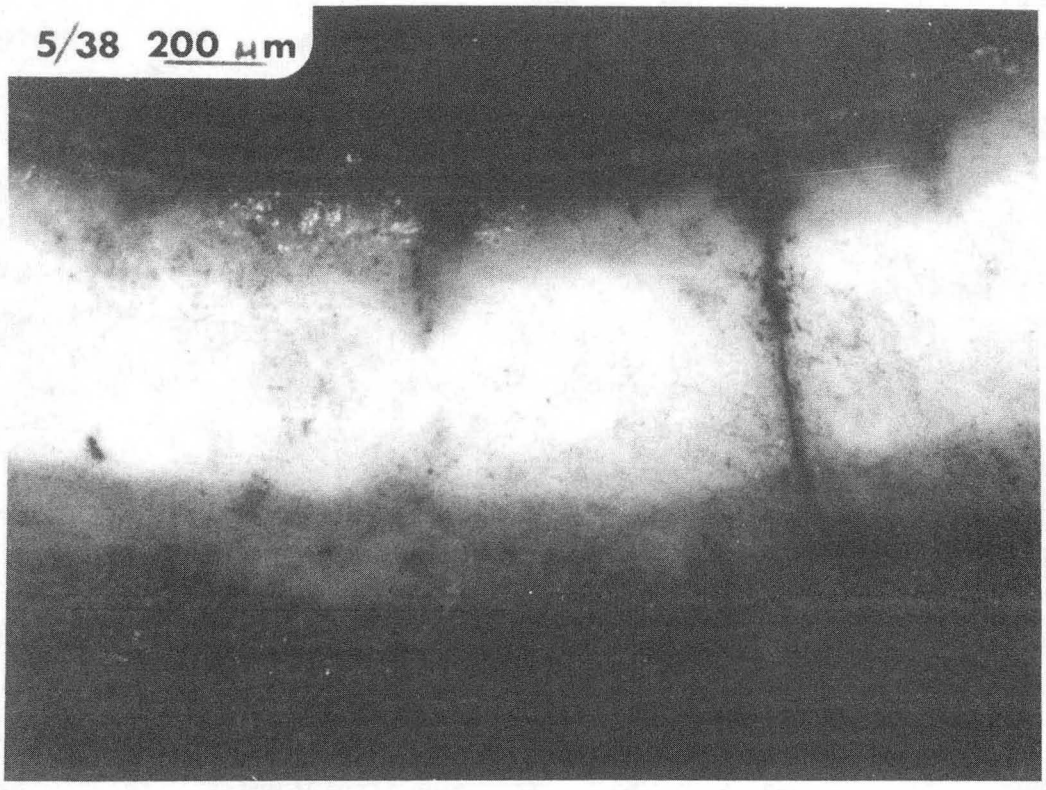

XBB 841-172

Fig. 3.5

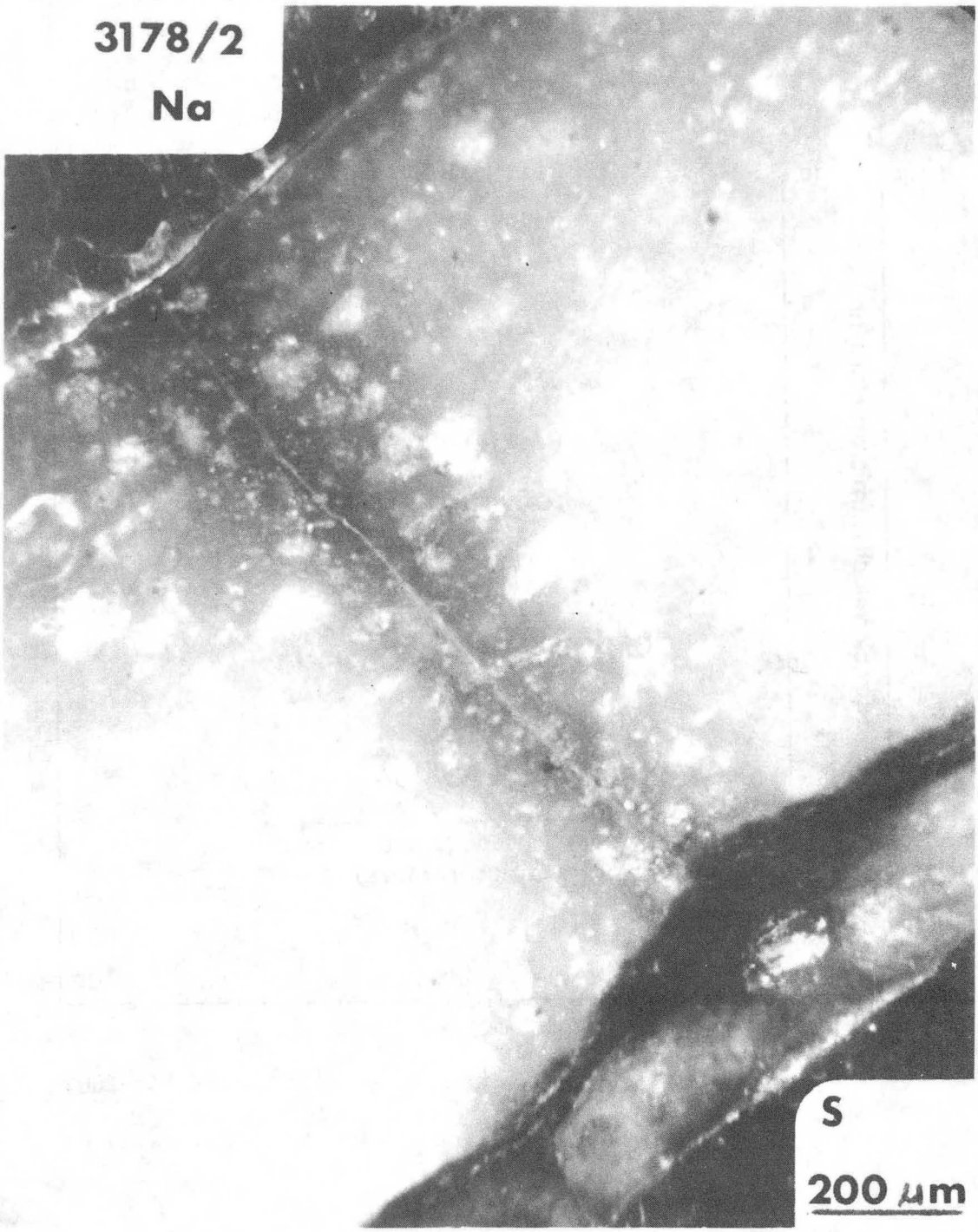

XBB 830-9344

Fig. 3.6

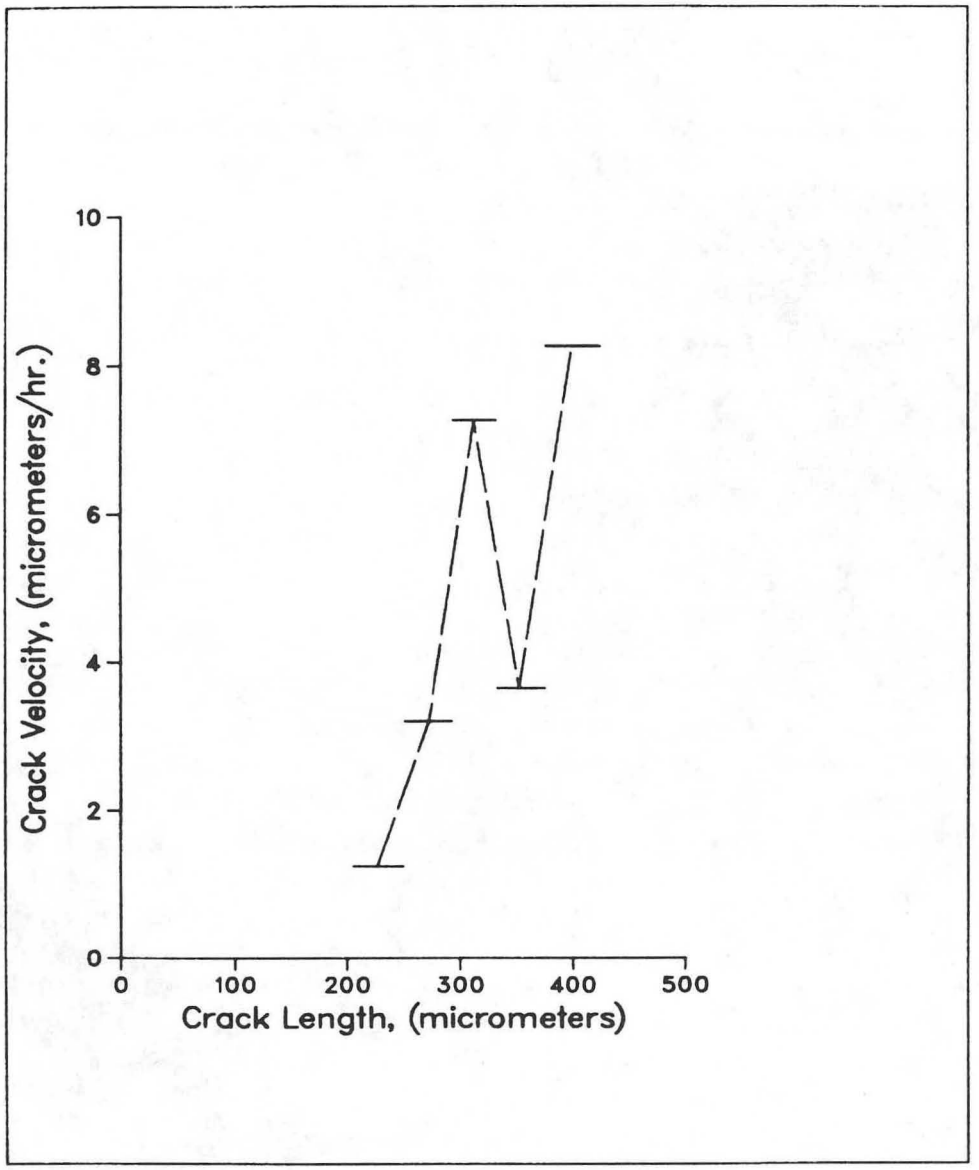

XBL 845-2003

Fig. 3.7

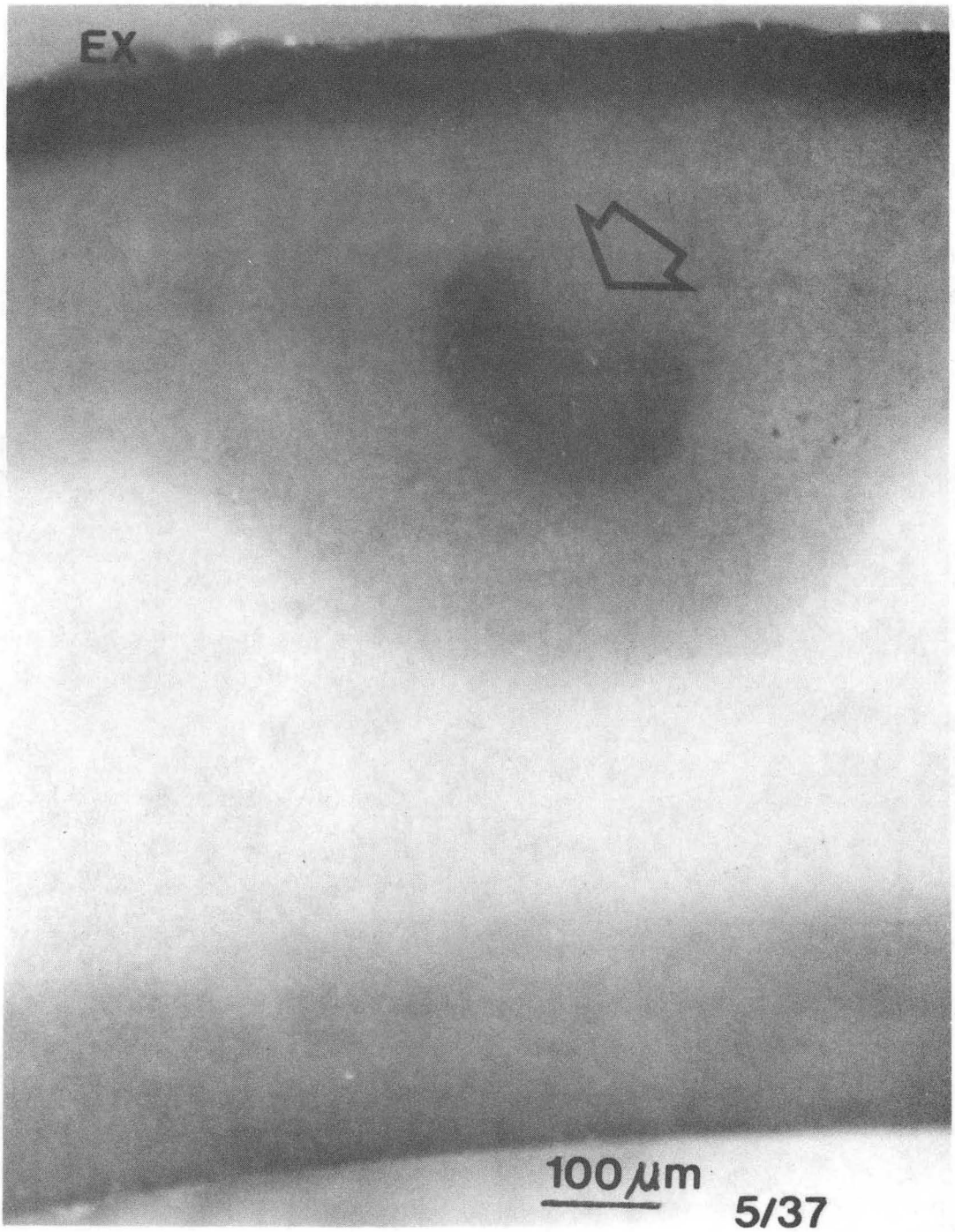

Fig. 3.8

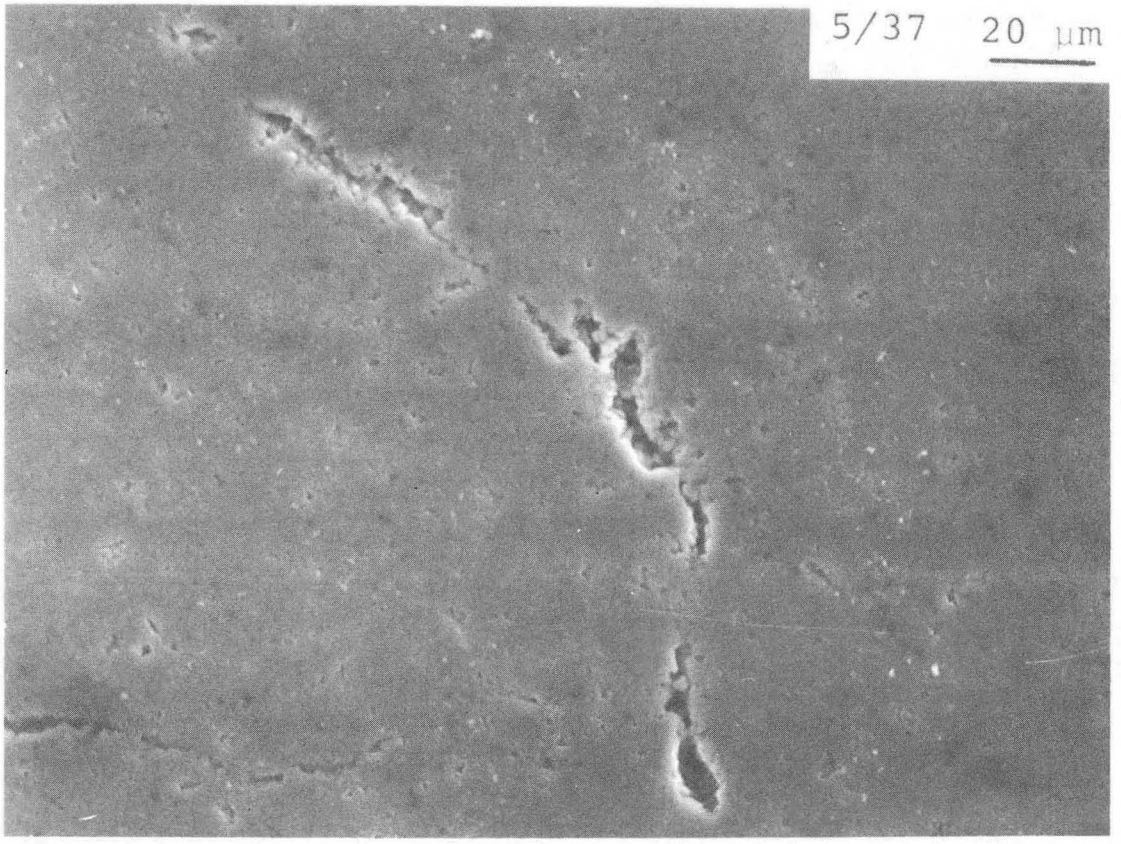

XBB 838-7686

Fig. 3.9

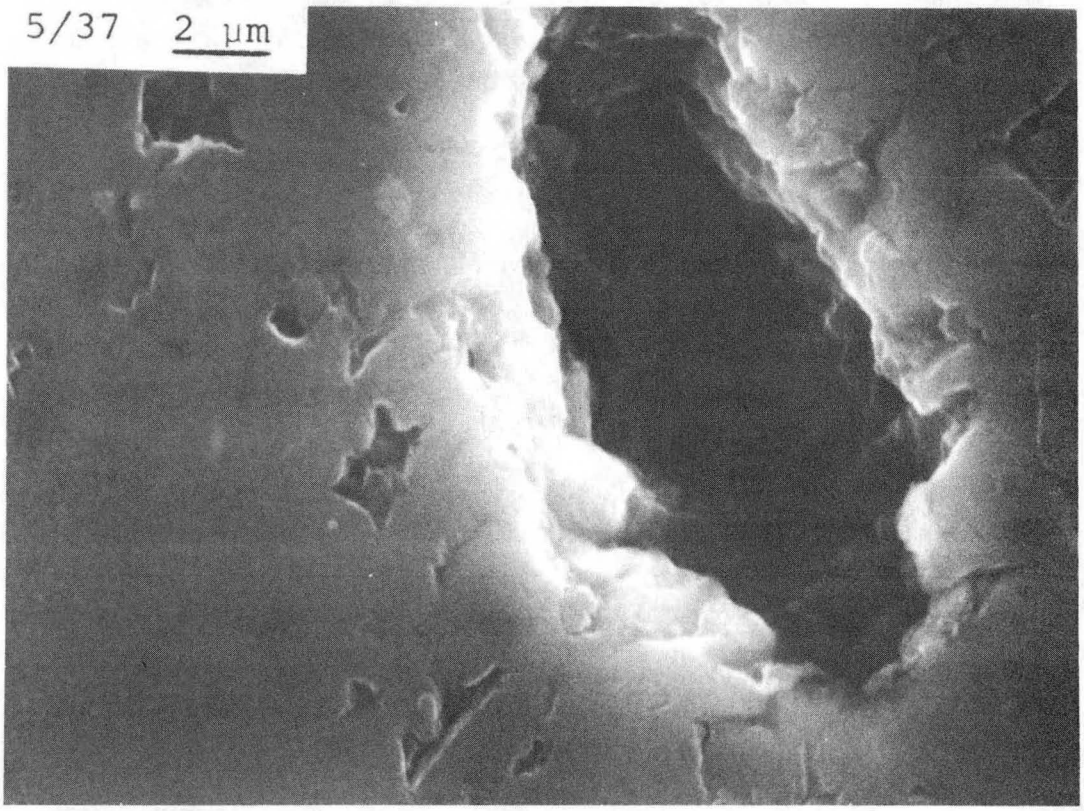

XBB 838-7688

Fig. 3.10

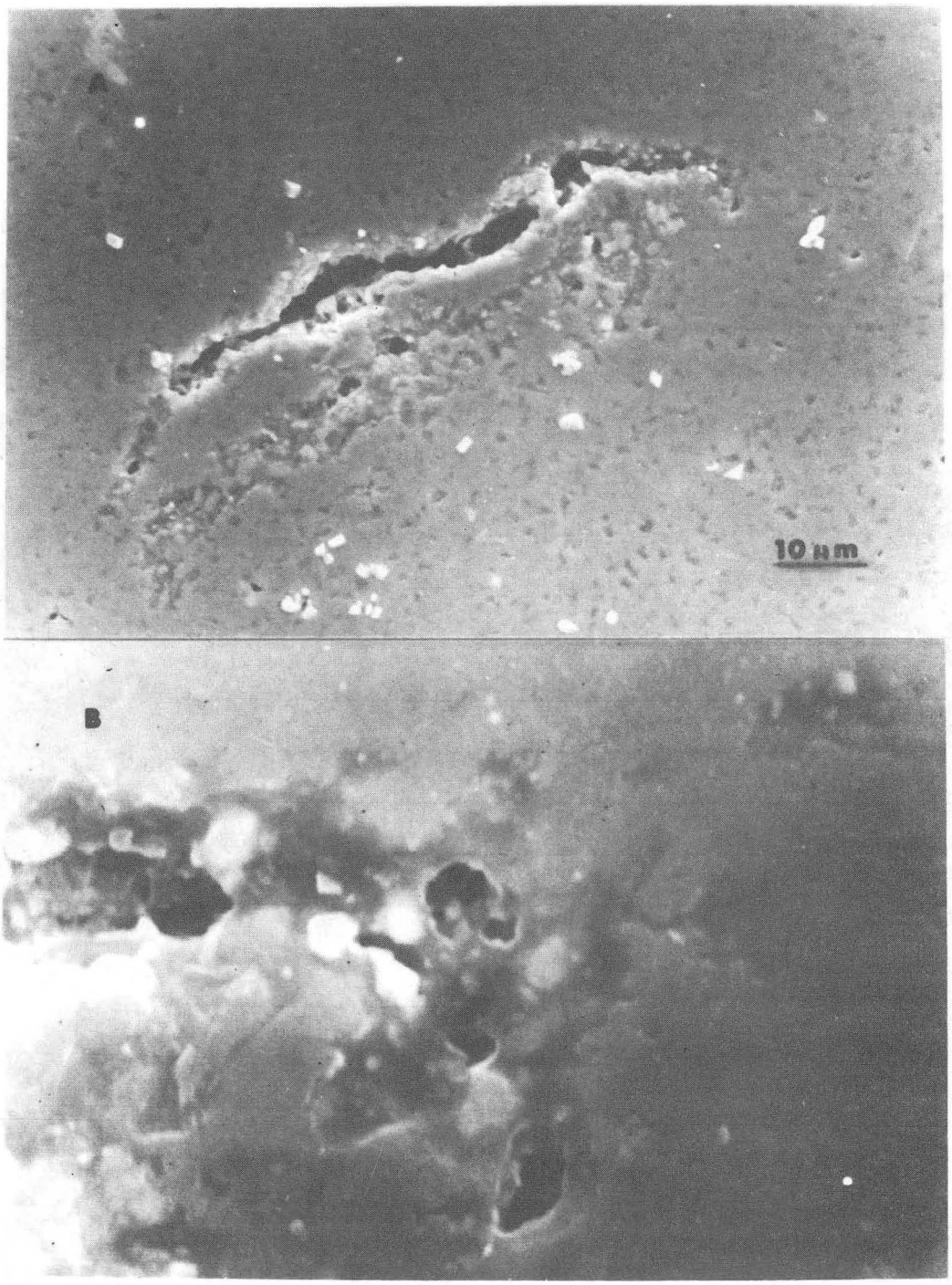

XBB 844-2638

Fig. 3.11

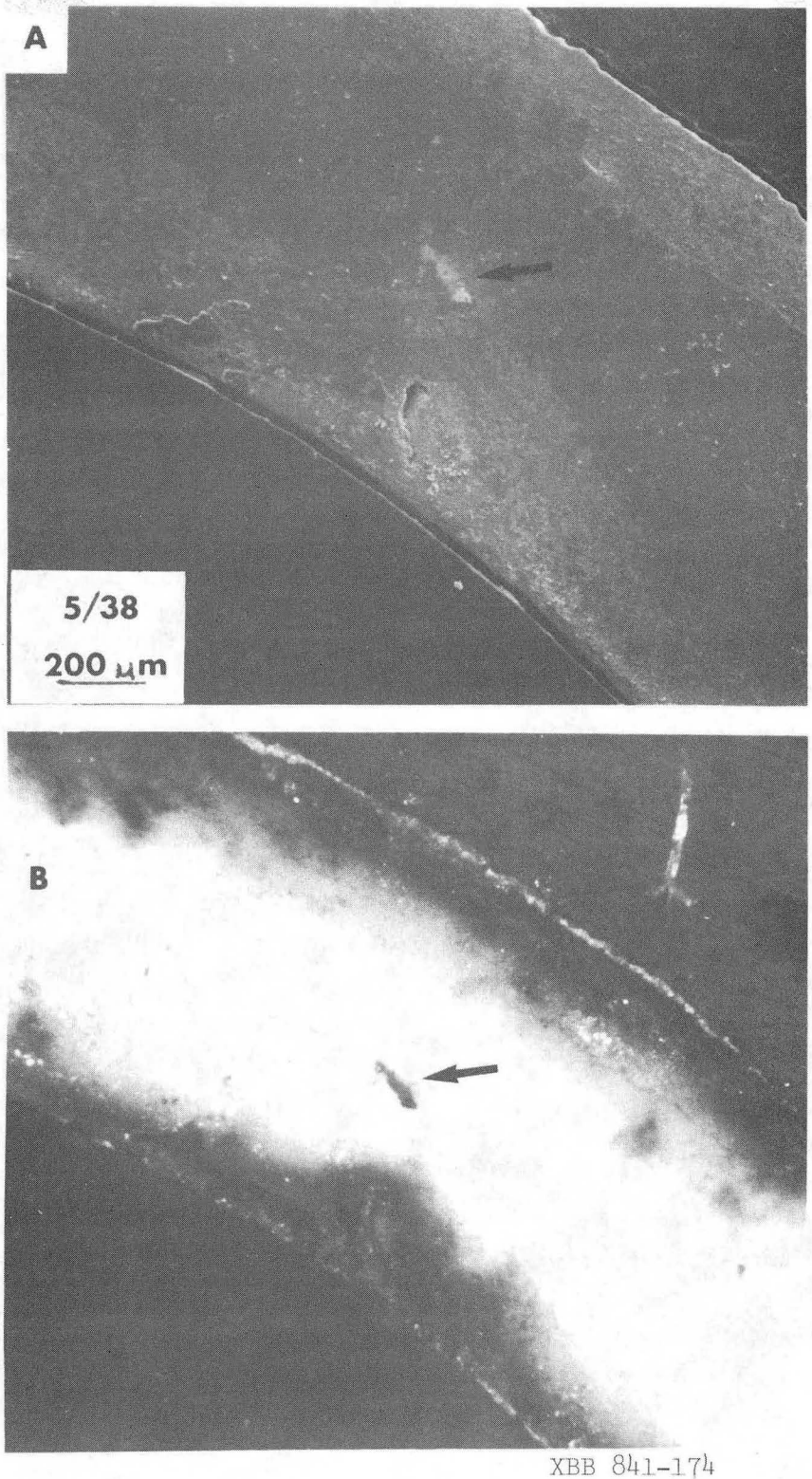

XBB 841-174

Fig. 3.12

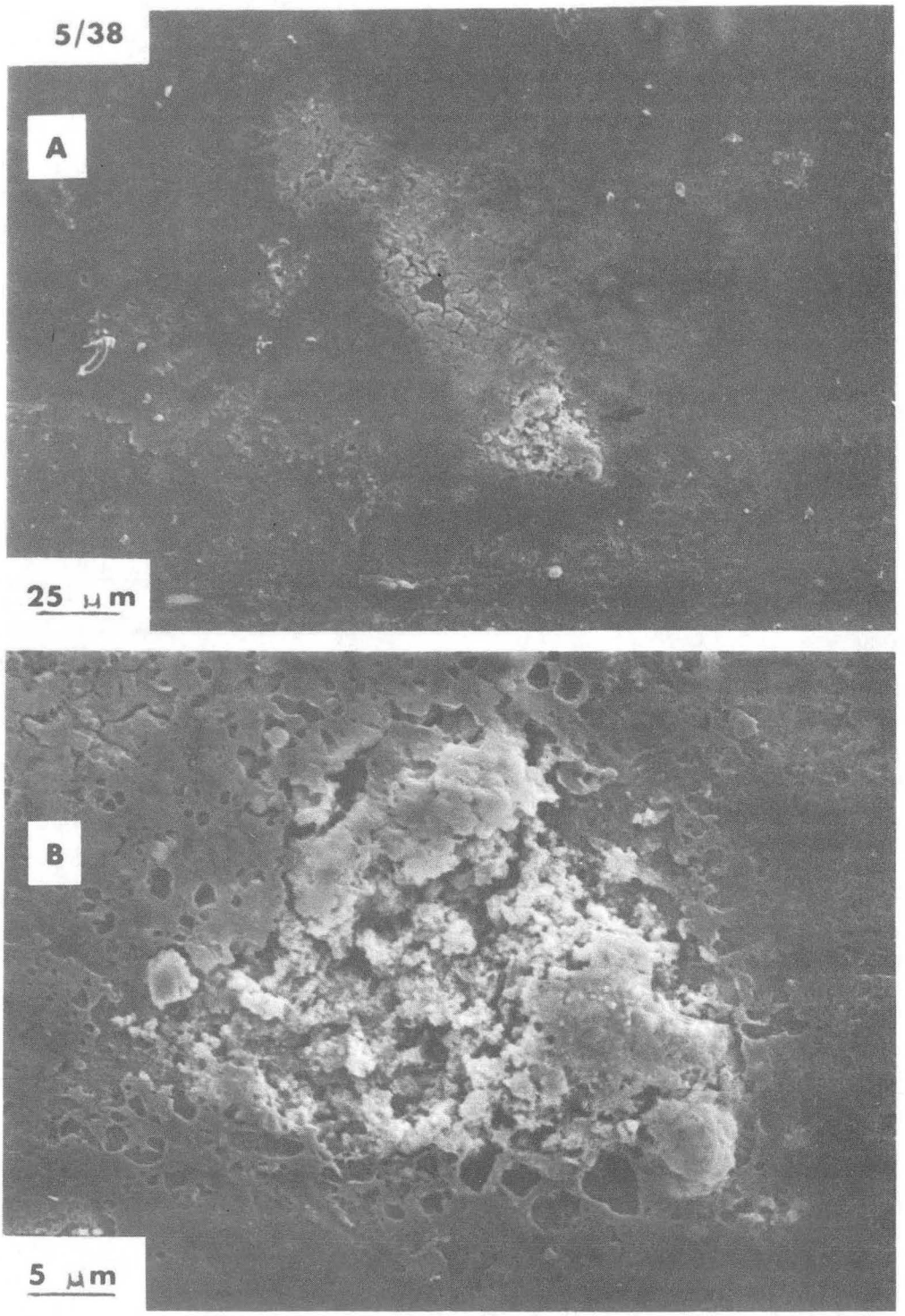

XBB 841-173

Fig. 3.13

XBB 844-2639

Fig. 3.14

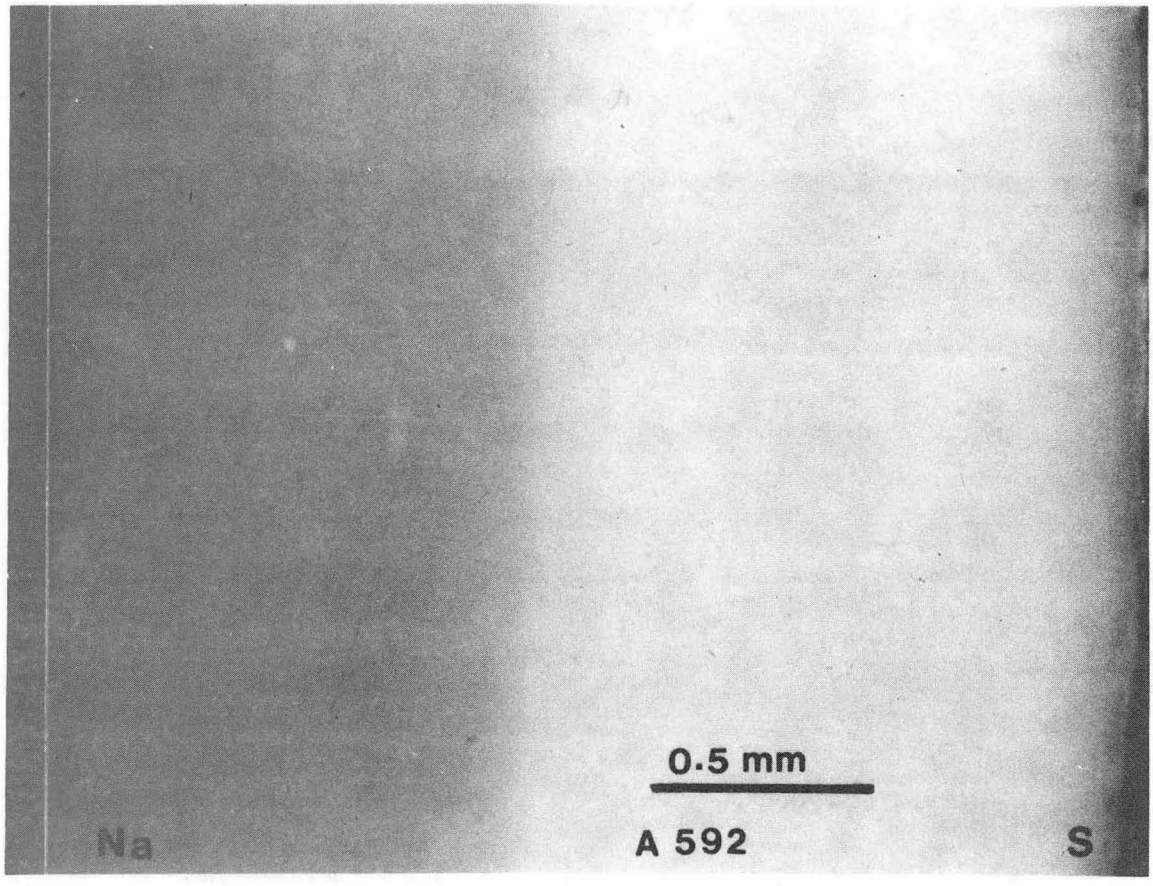

XBB 820-10682

Fig. 3.15

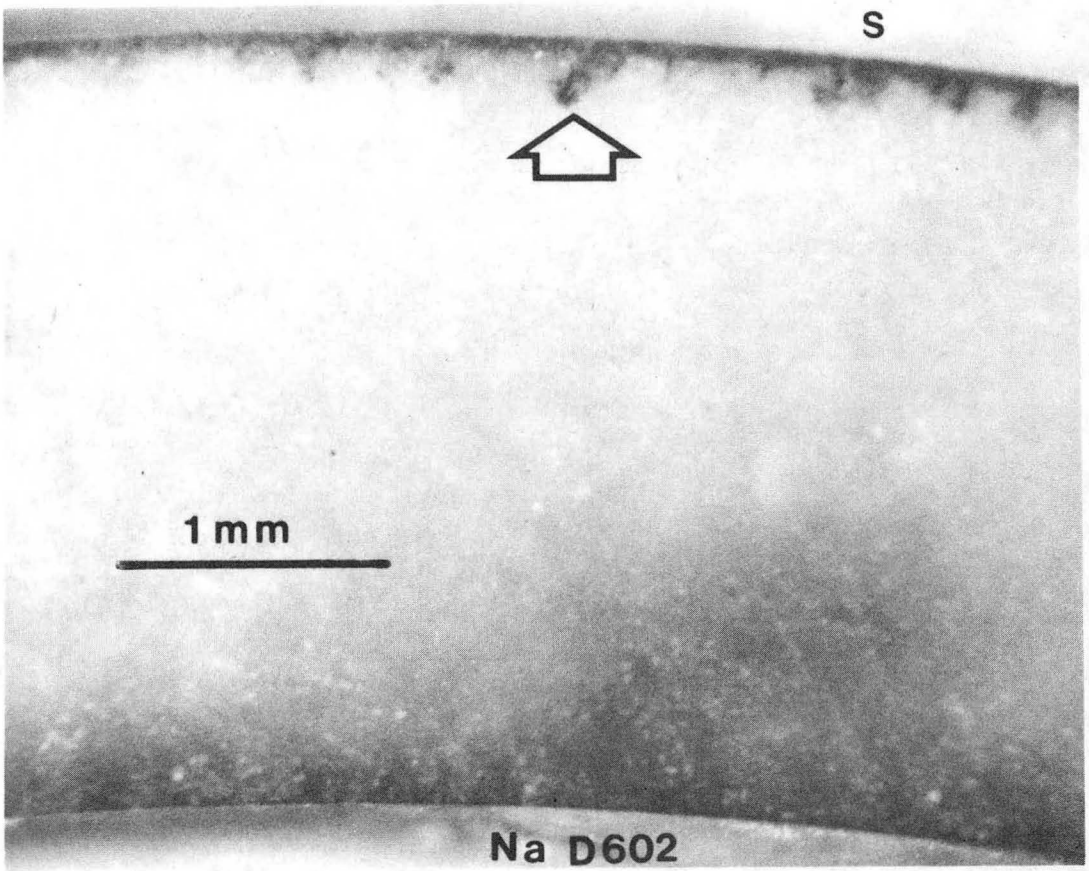

XBB 820-10686

Fig. 3.16

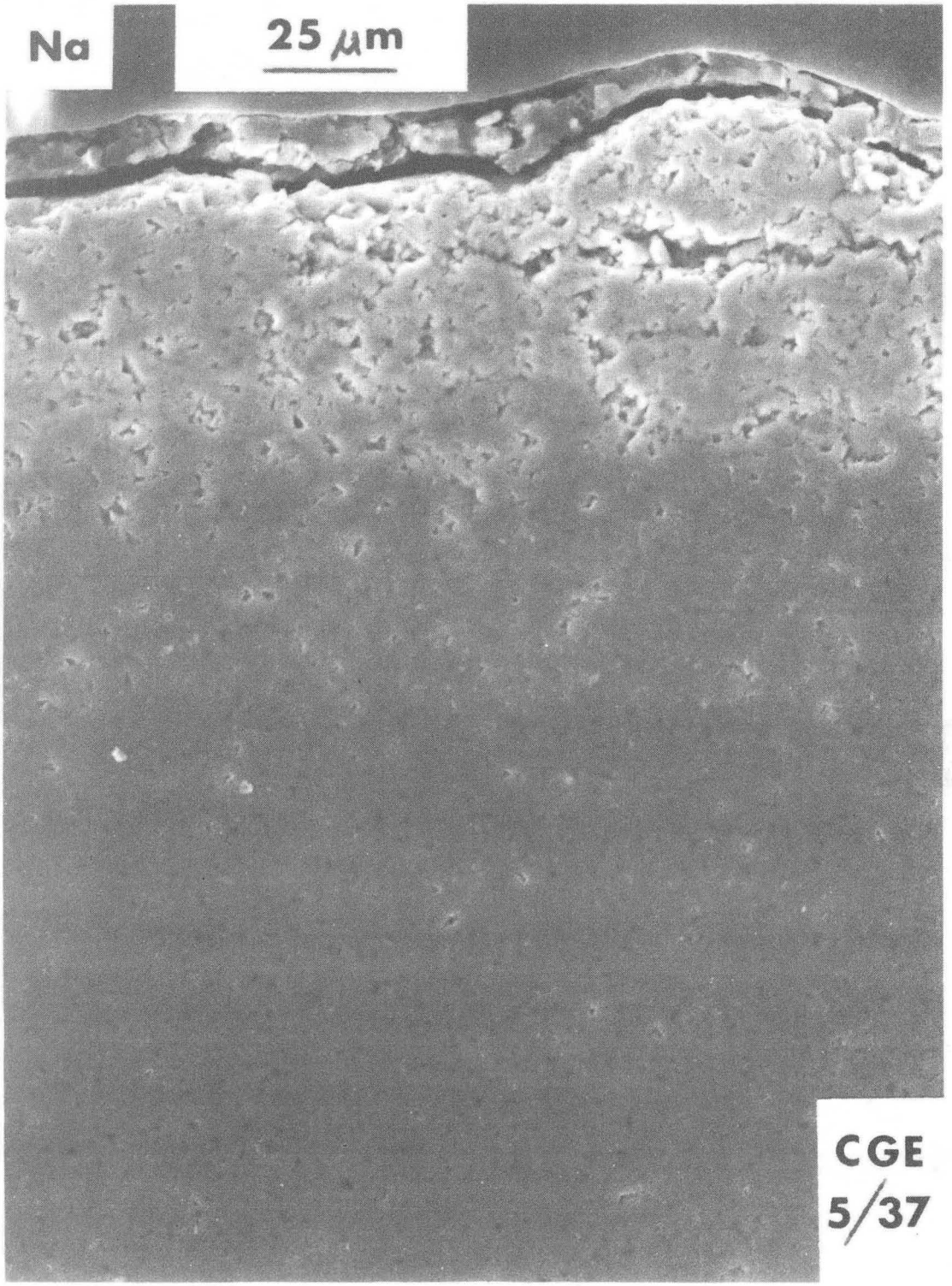

XBB 836-5181

Fig. 3.17

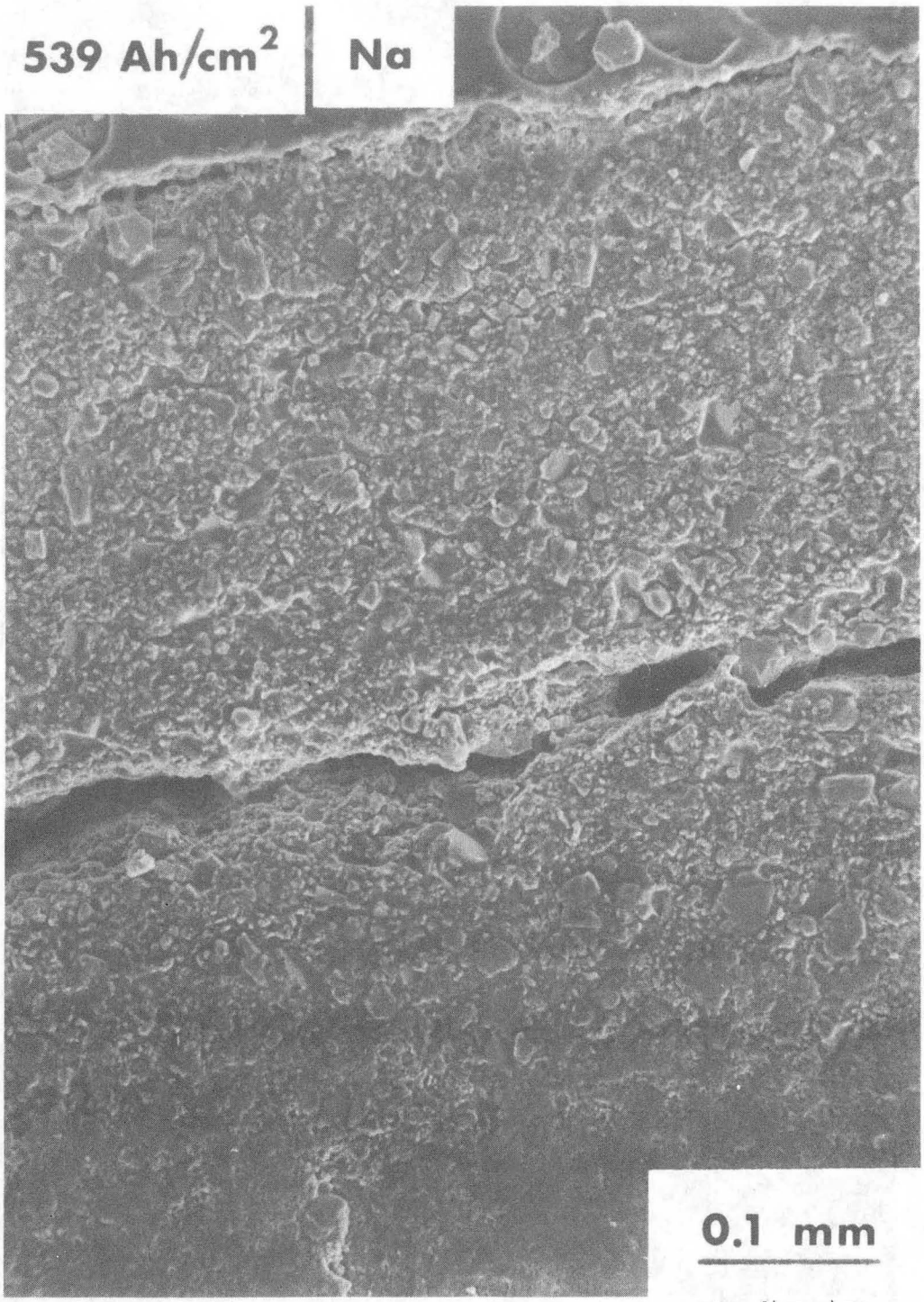

XBB 842-1450

Fig. 3.18

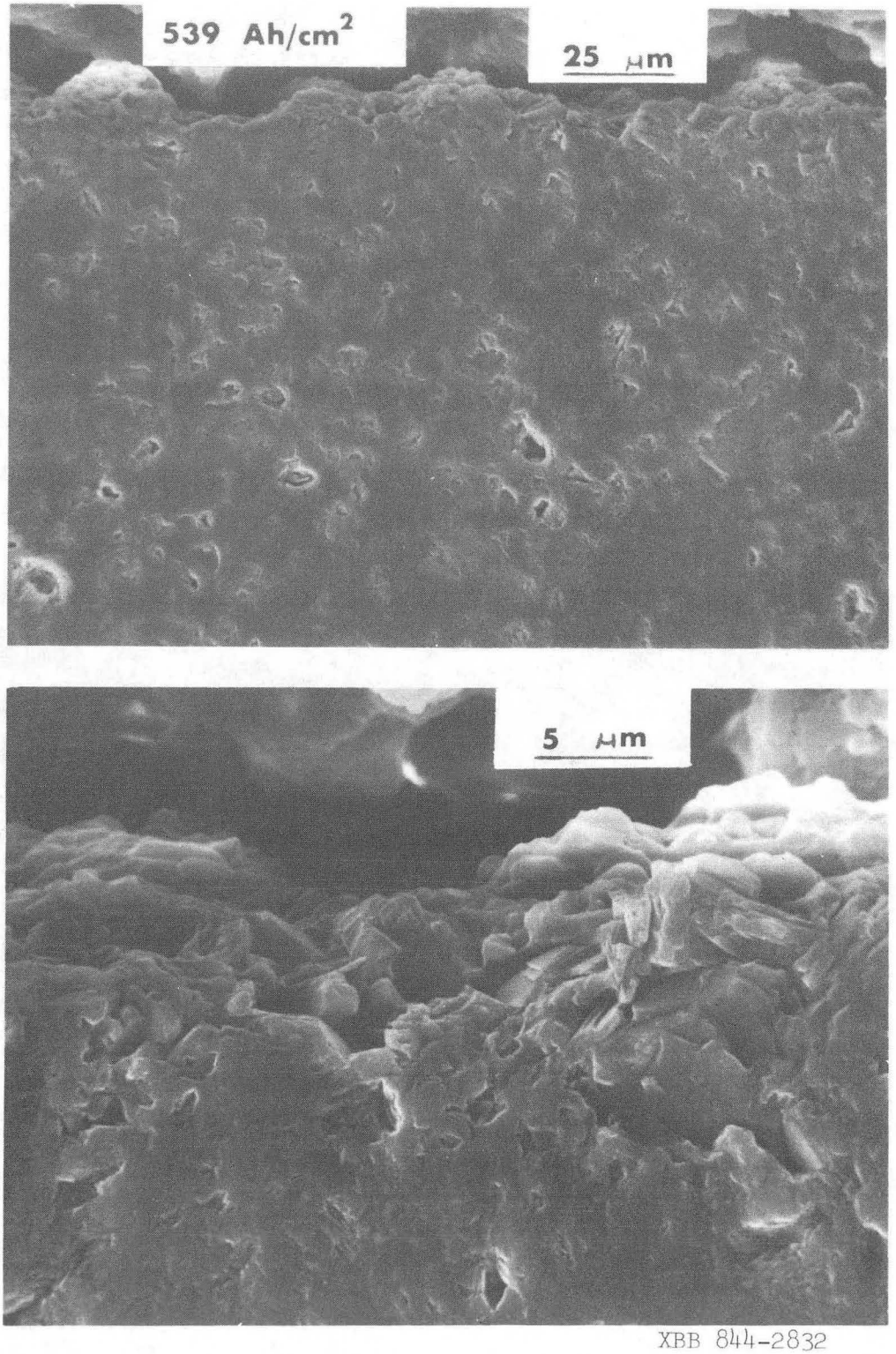

XBB 844-2832

Fig. 3.19

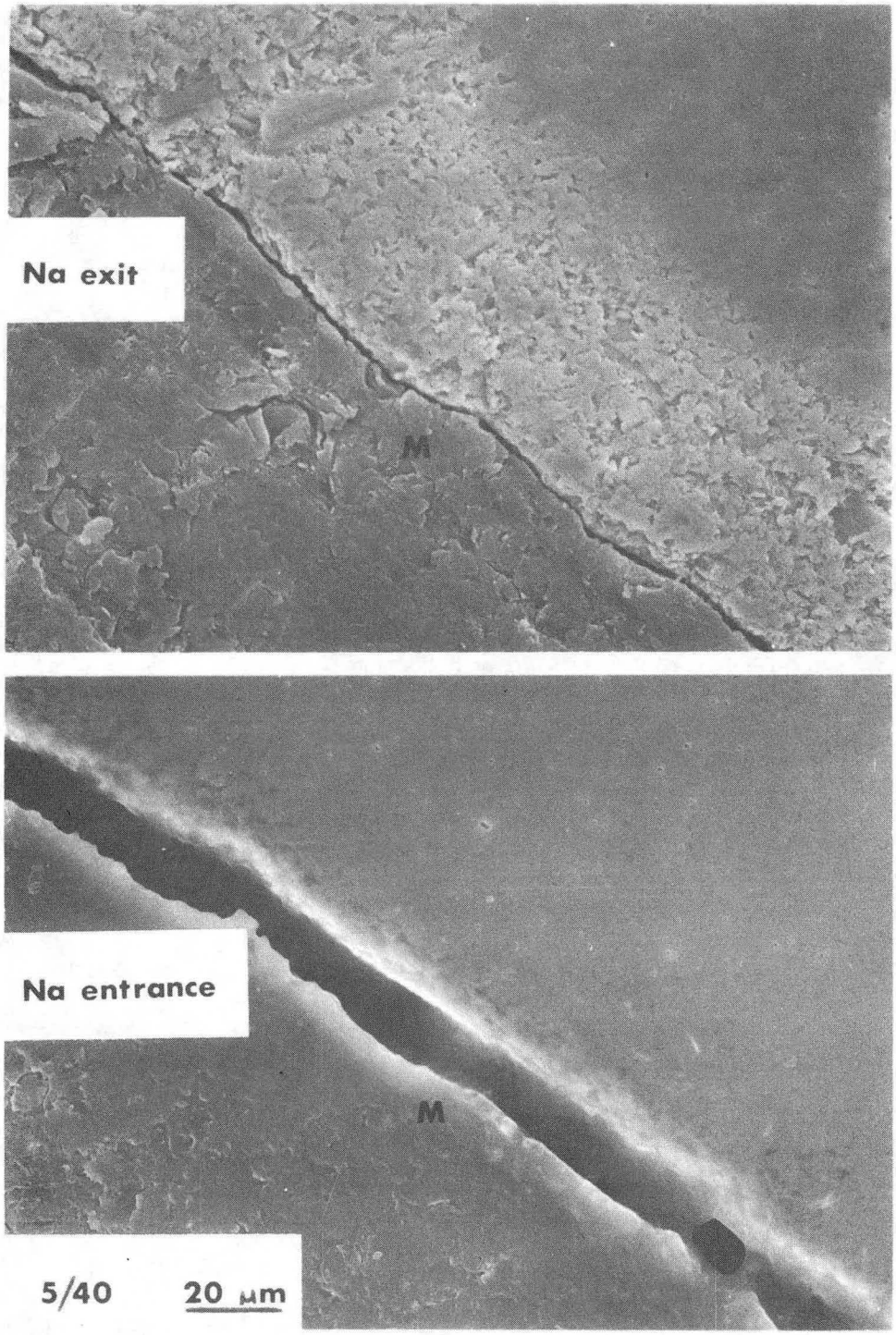

XBB 842-1416

Fig. 3.20

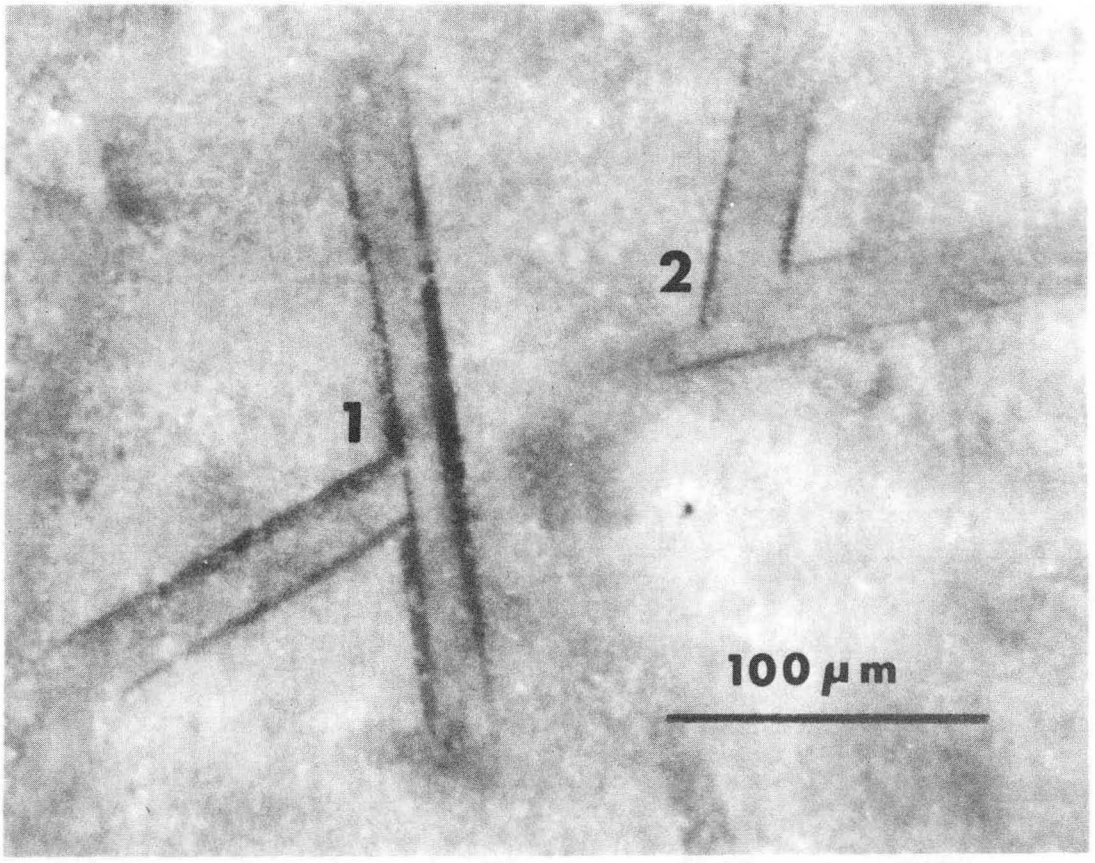

XBB 810-10999

Fig. 3.21

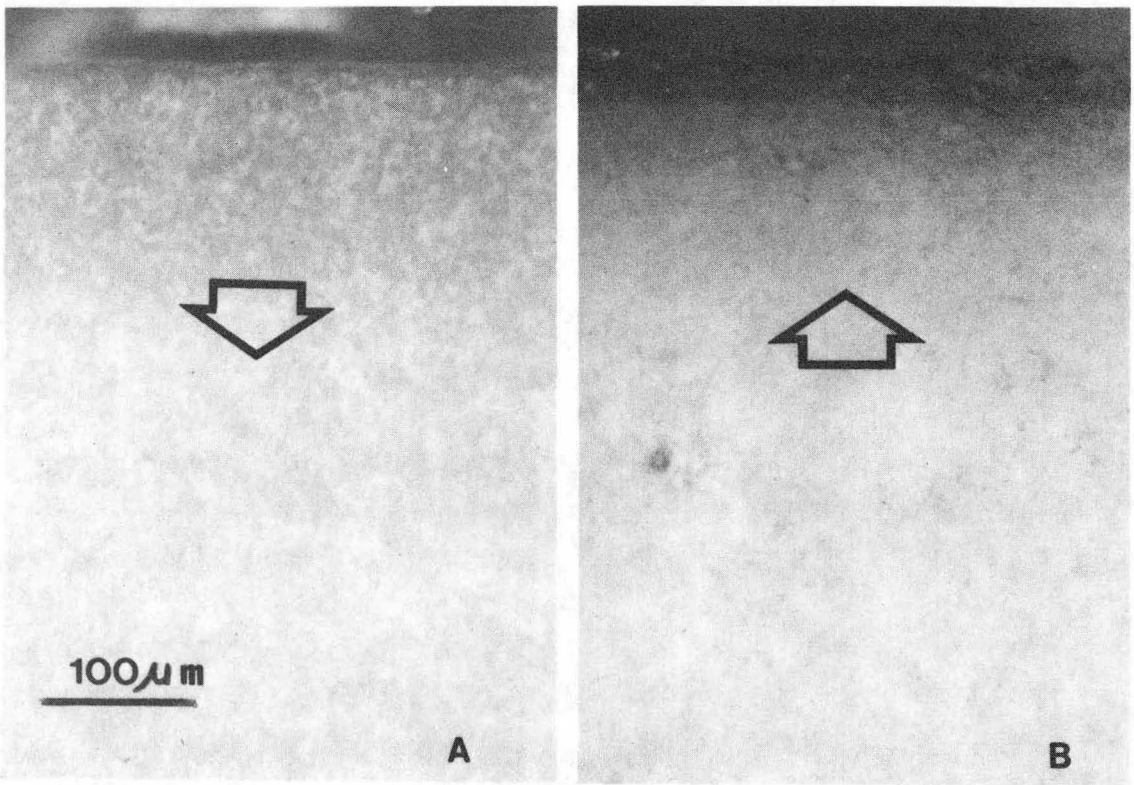

XBB 820-10690

Fig. 3.22

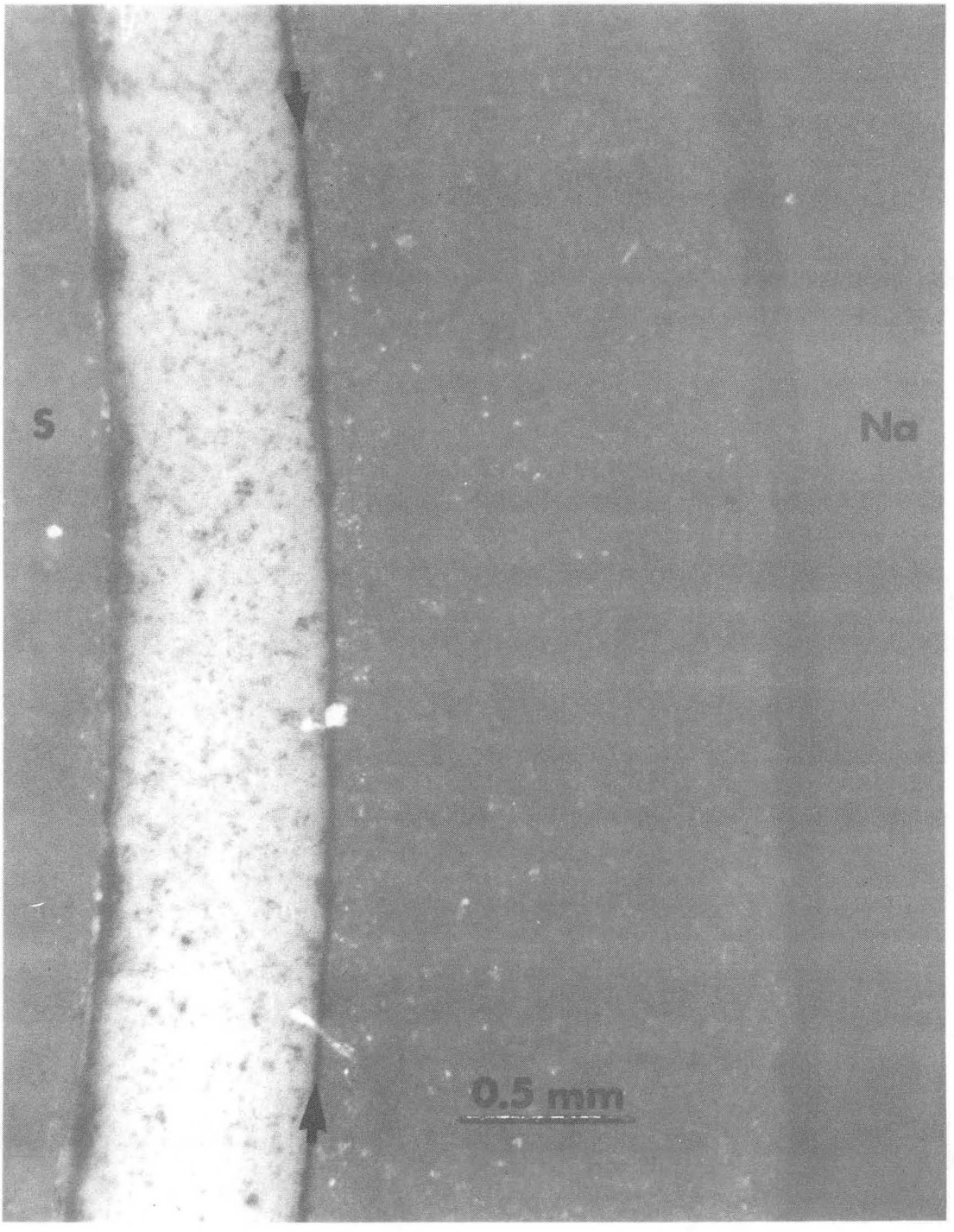

XBB 842-1454

Fig. 3.23

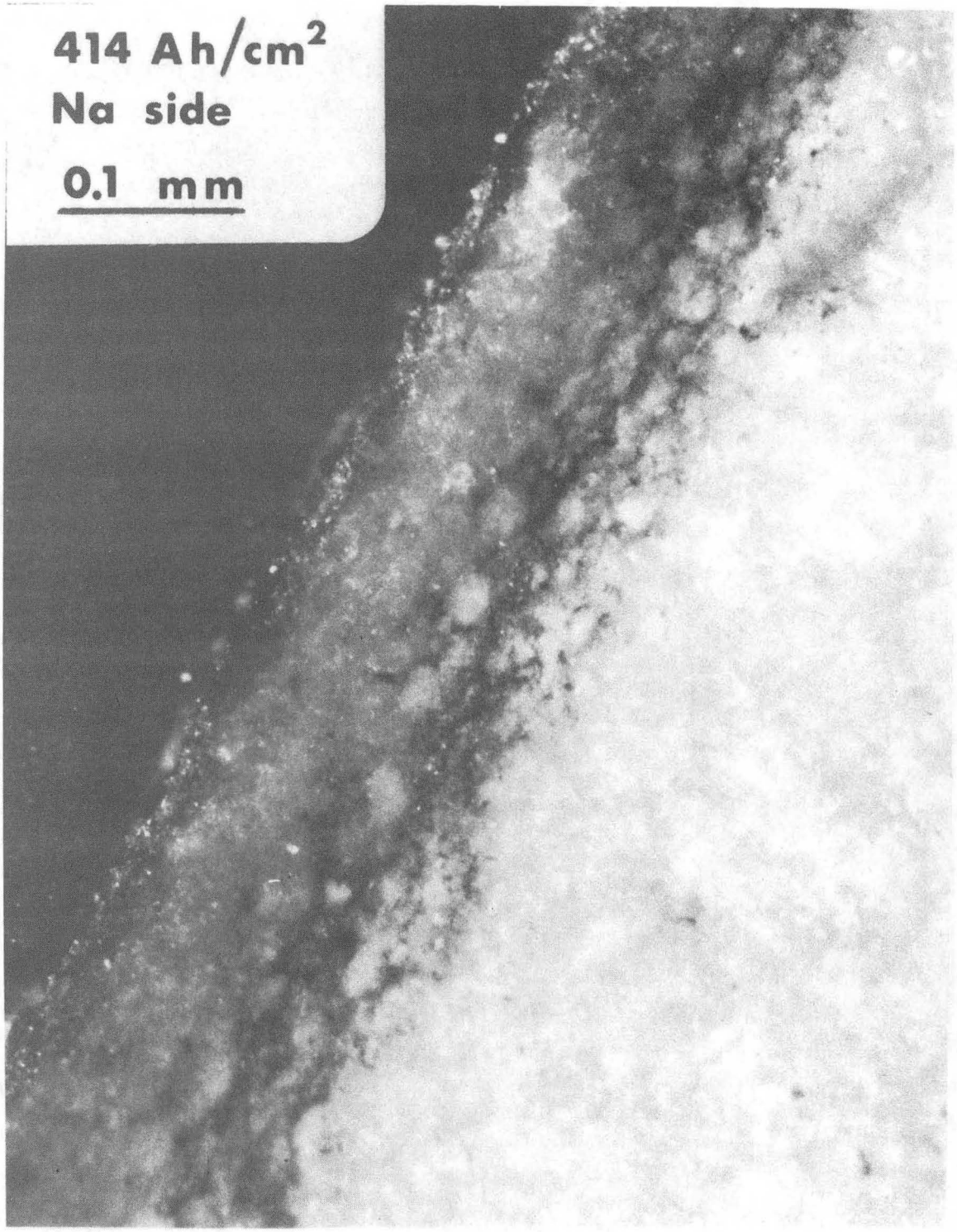

XBB 843-2032

Fig. 3.24

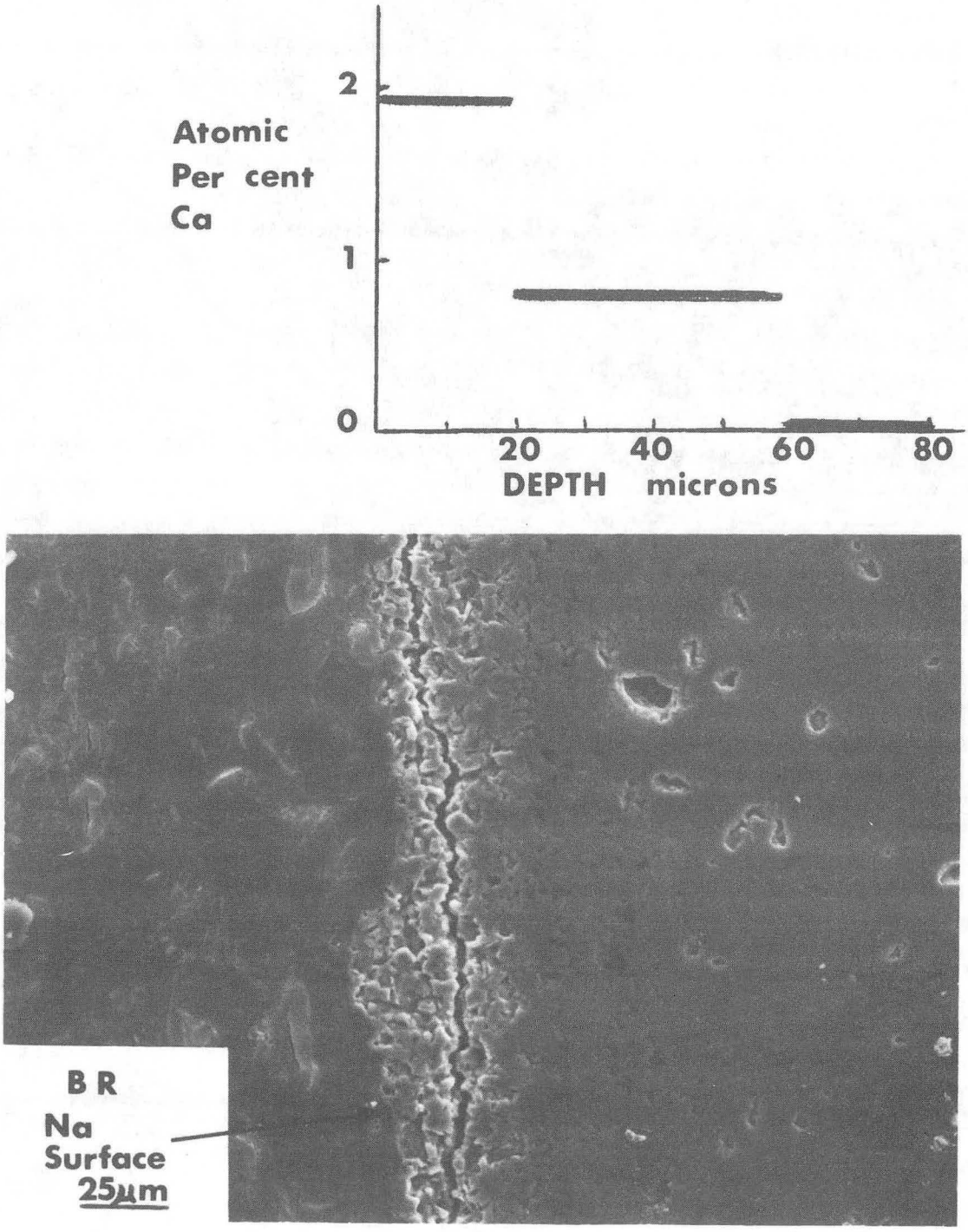

XBB 830-8823

Fig. 3.25

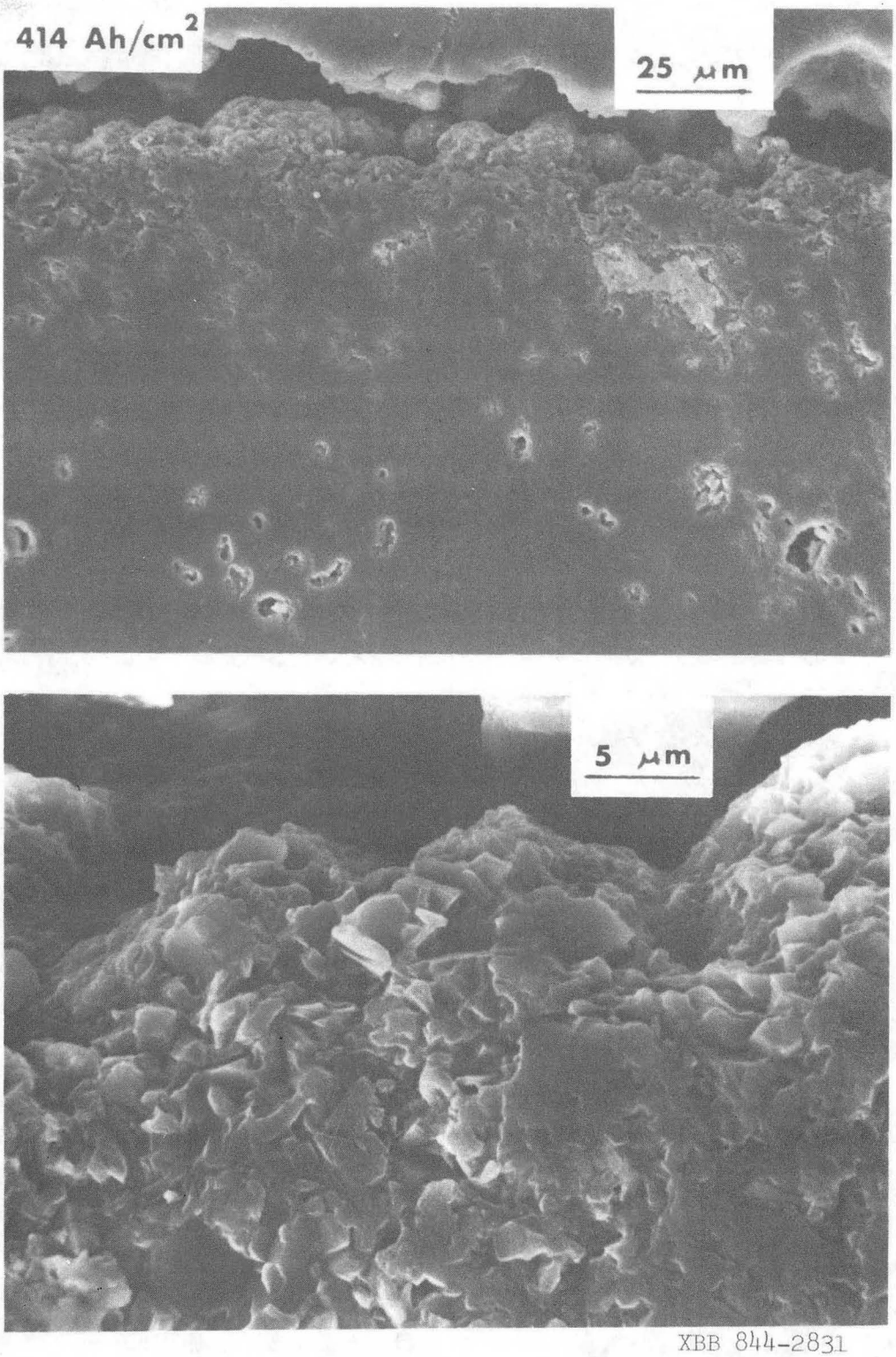

XBB 844-2831

Fig. 3.26

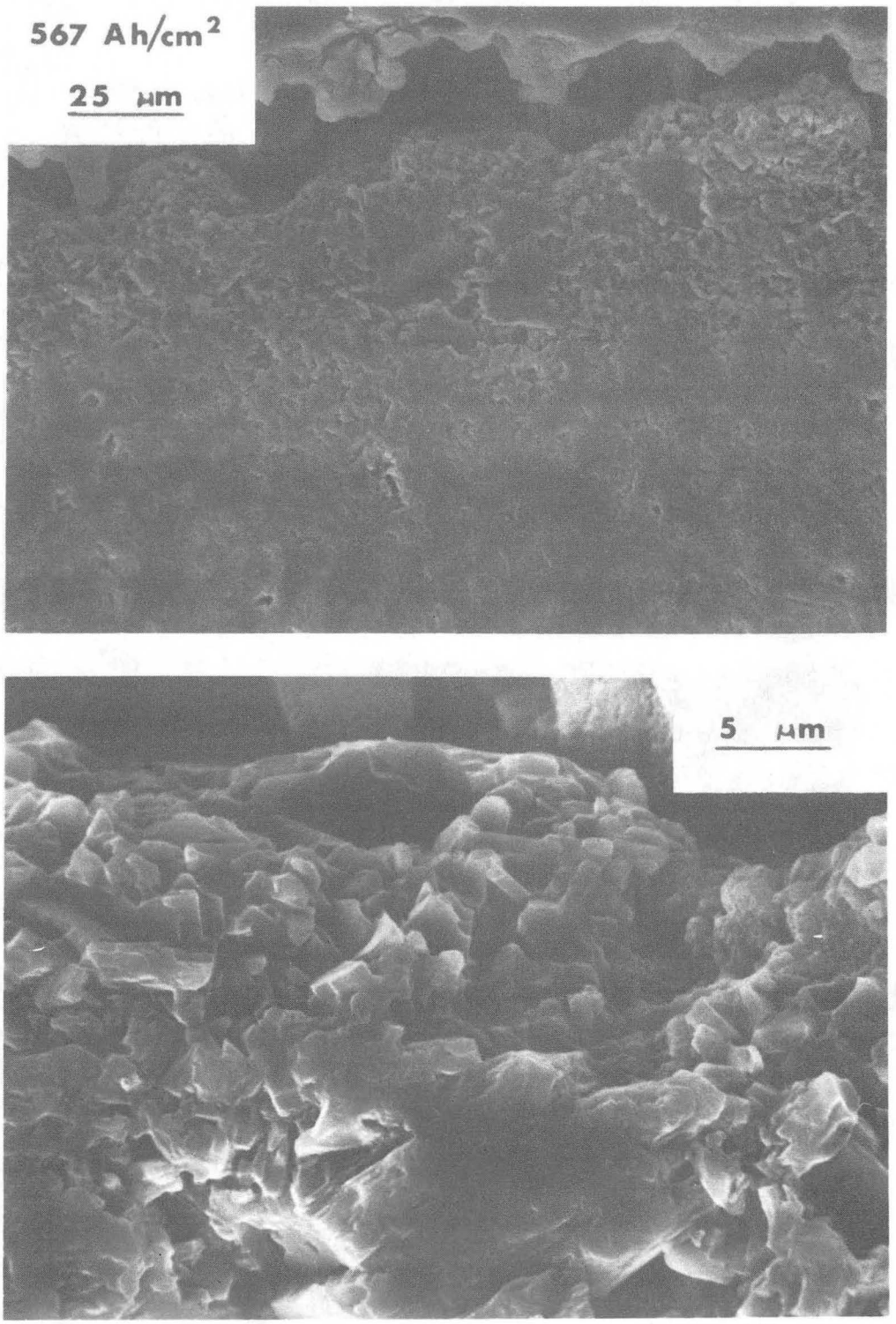

XBB 844-2830

Fig. 3.27

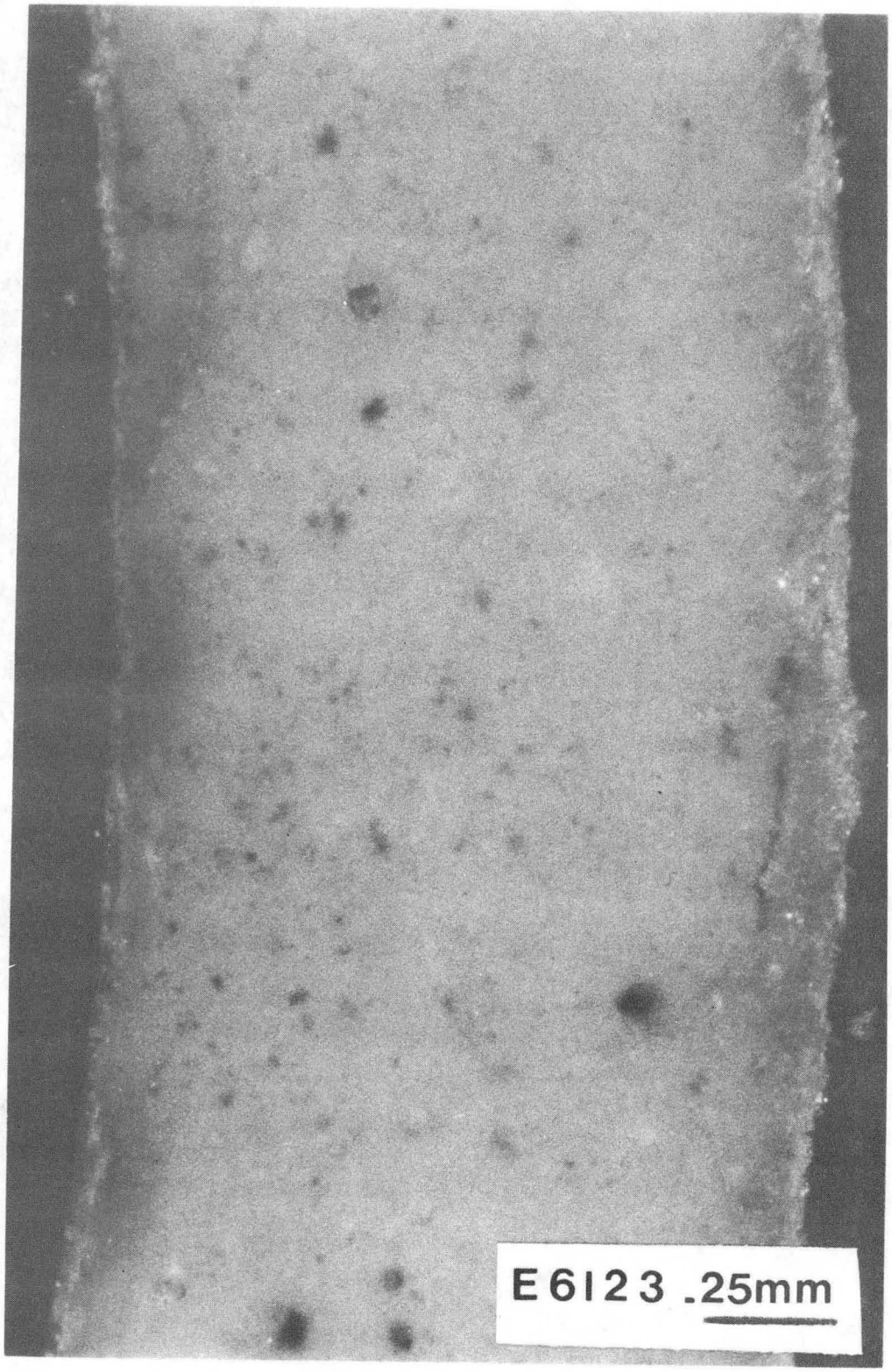

XBB 843-2051

Fig. 3.28

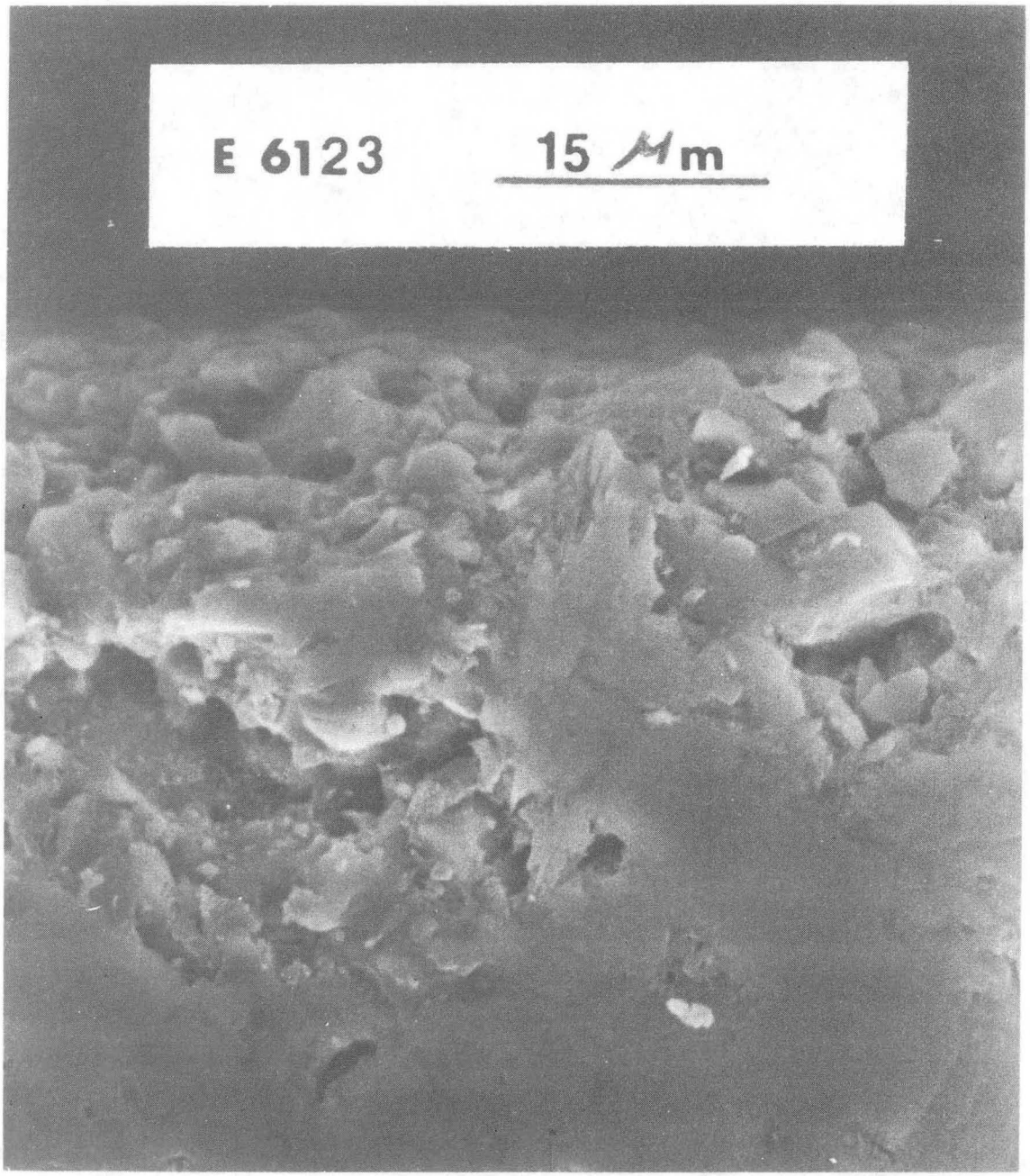

XBB 843-2038

Fig. 3.29

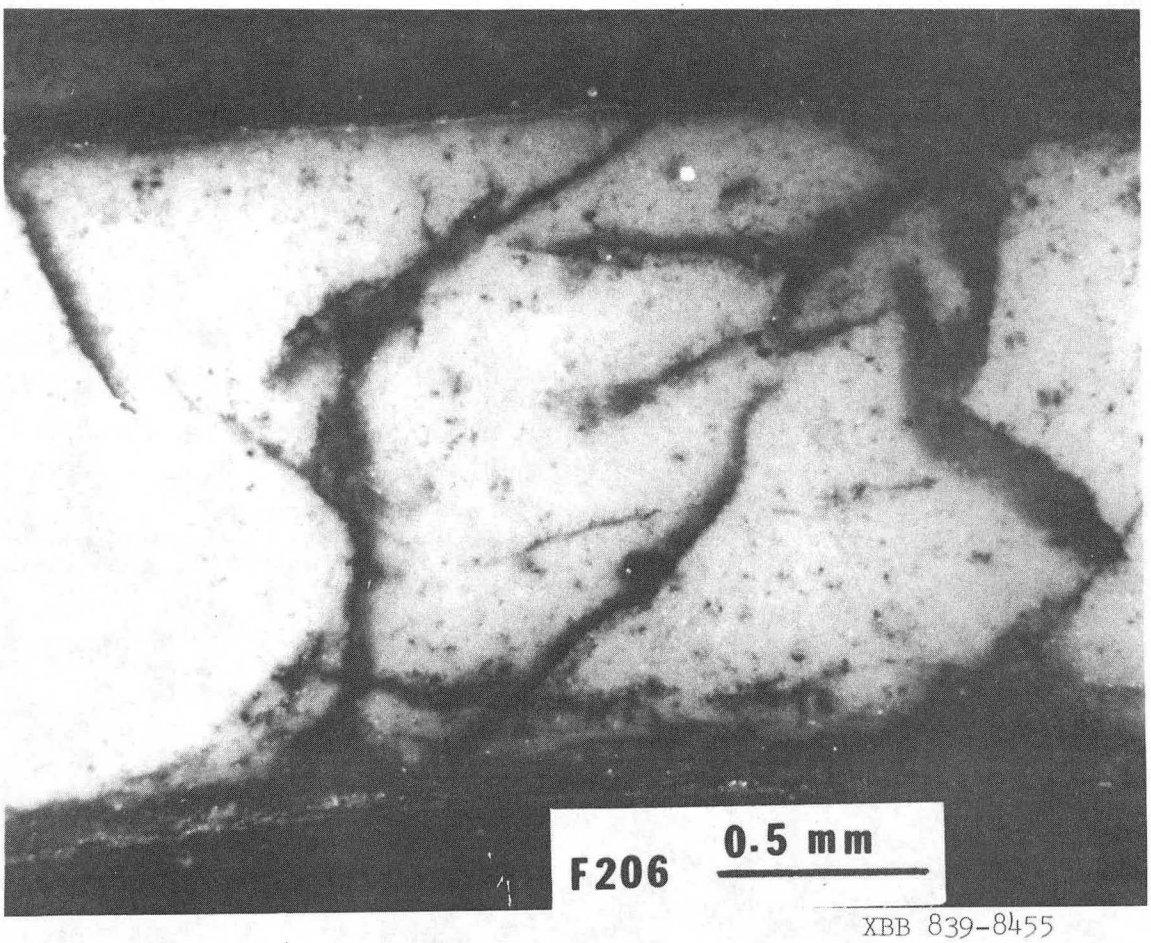

XBB 839-8455

Fig. 3.30

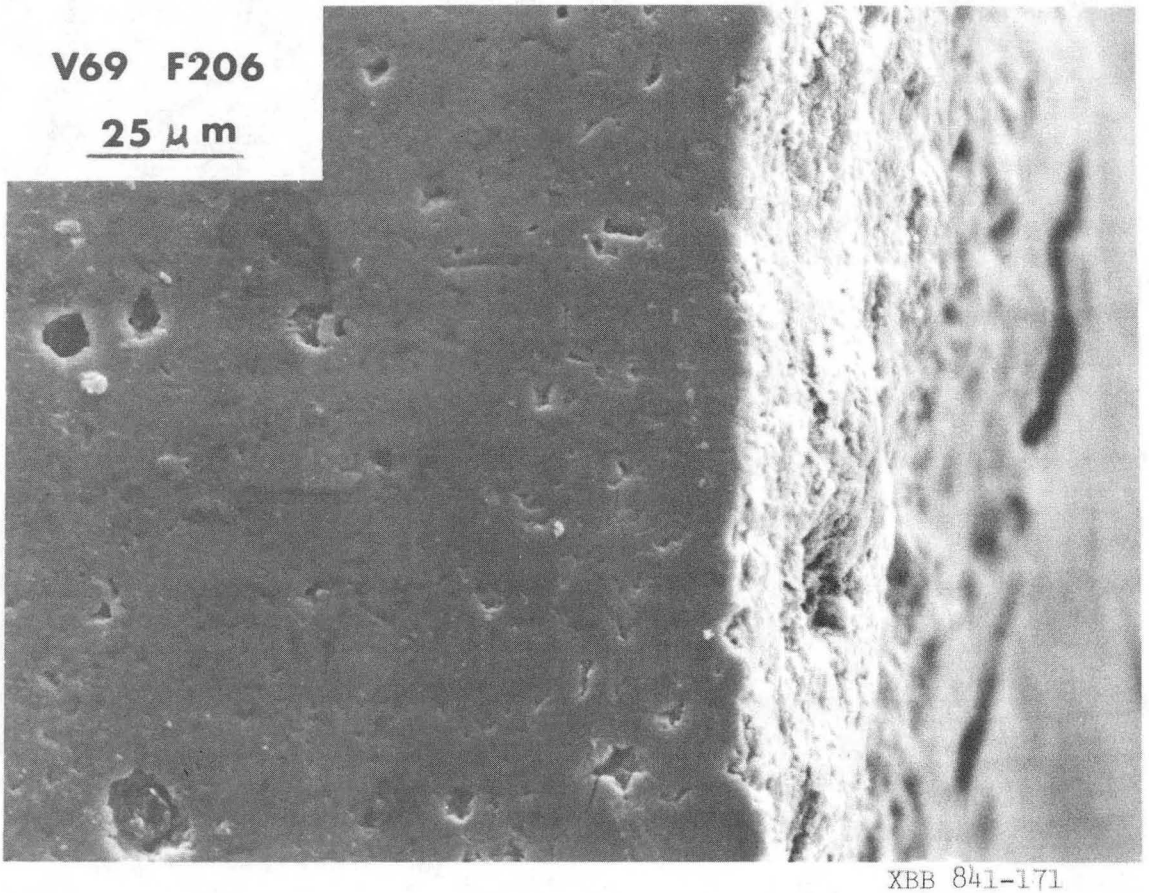

XBB 841-171

Fig. 3.31

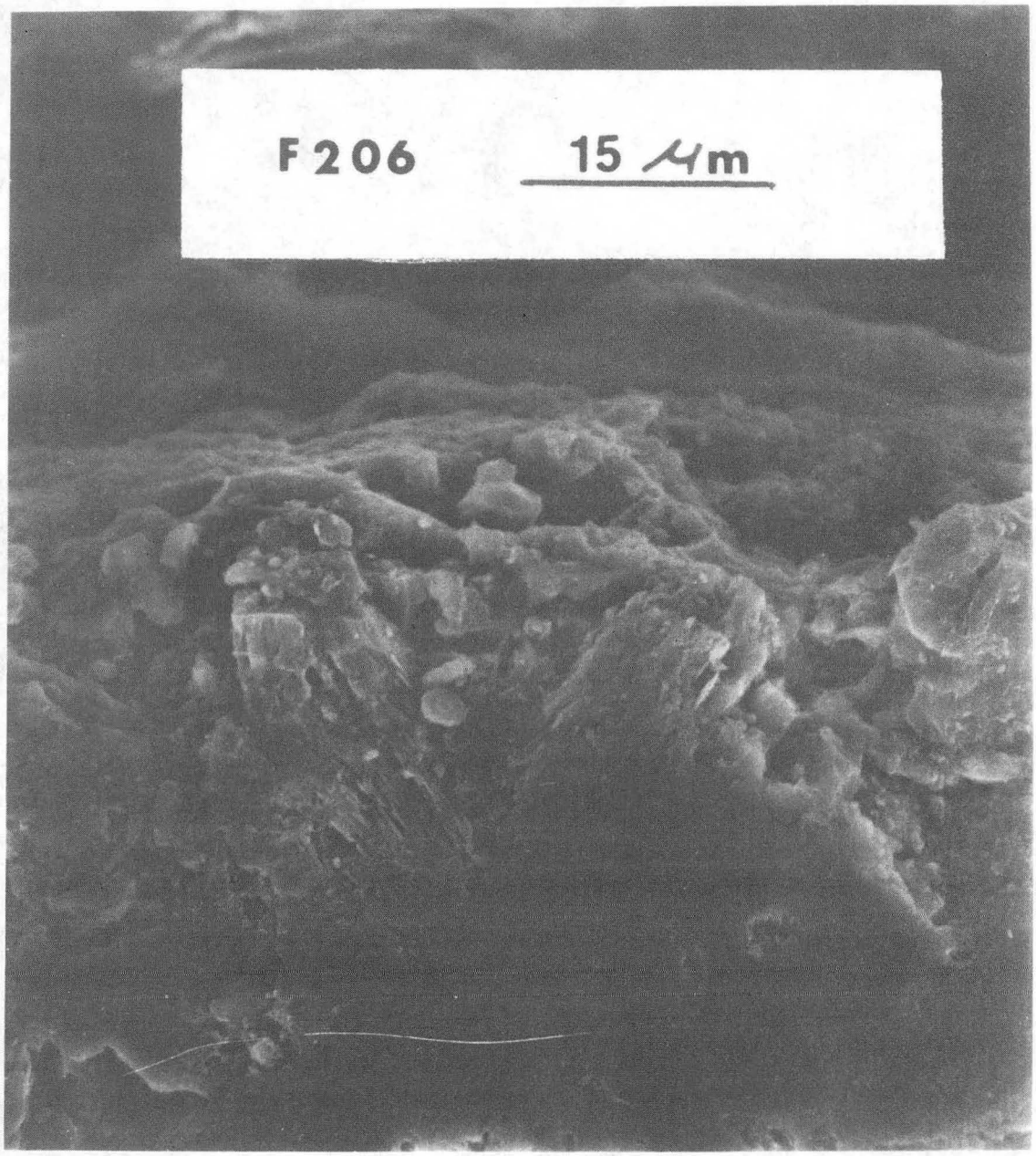

XBB 843-2048

Fig. 3.32

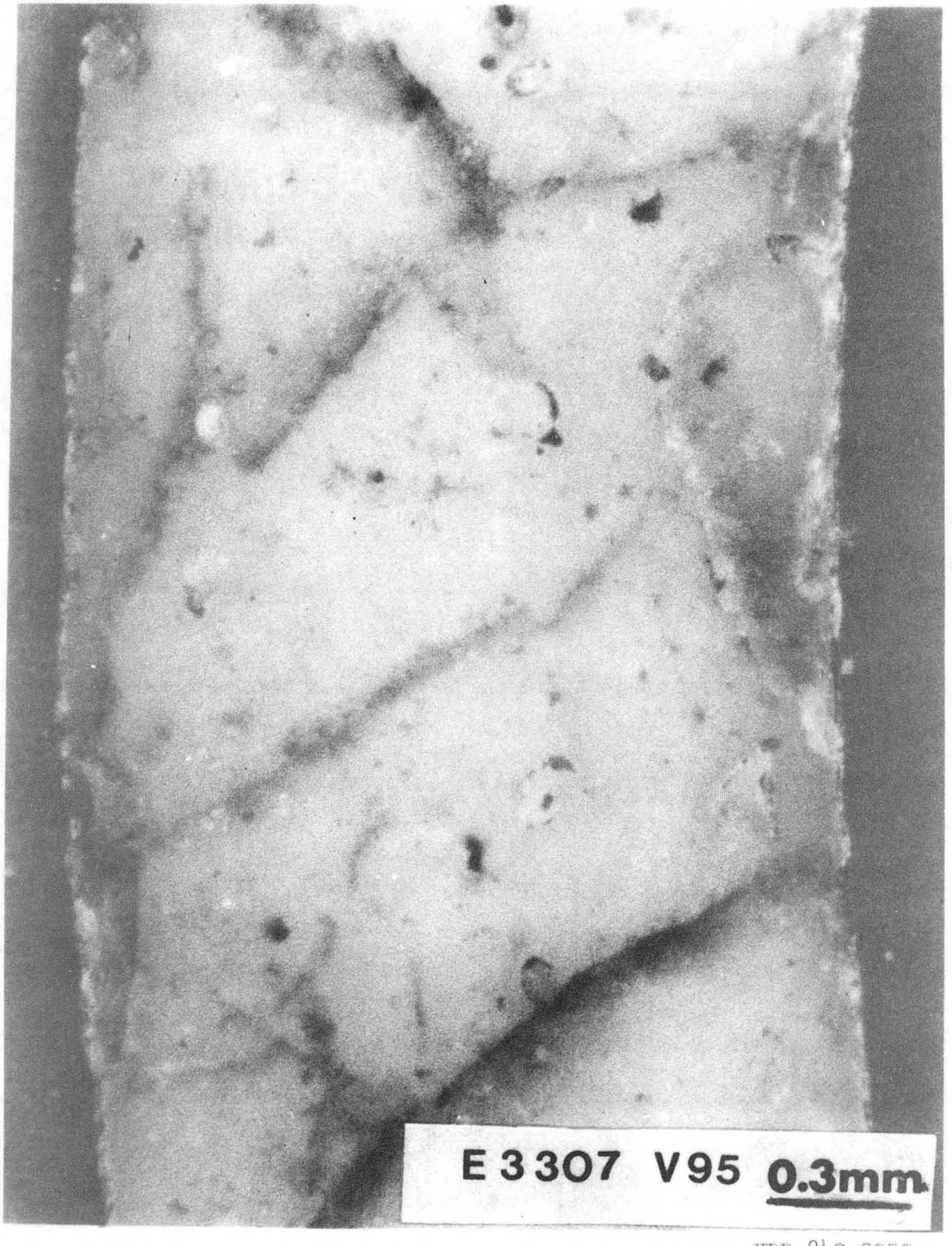

XBB 843-2050

Fig. 3.33

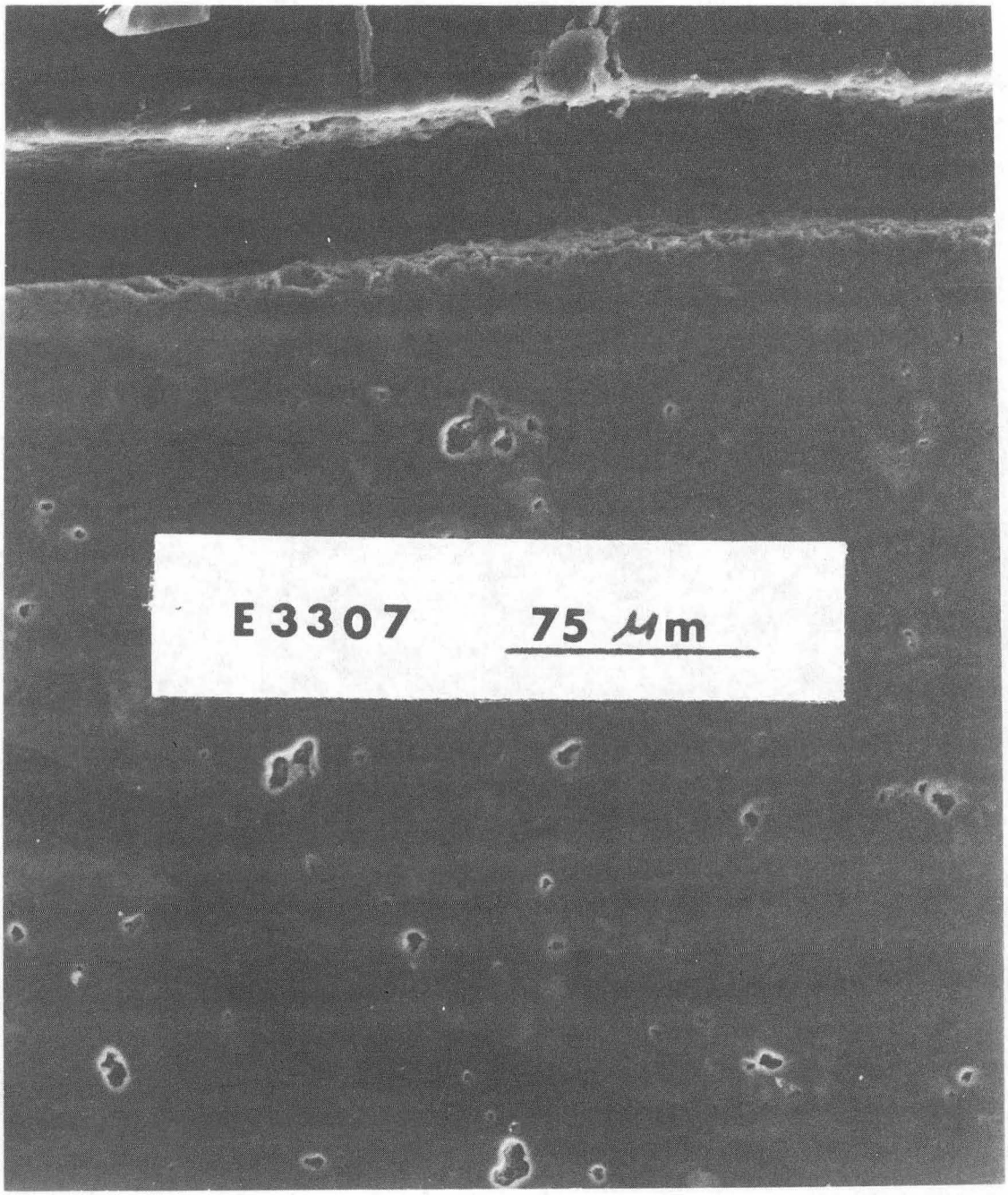

XBB 843-2046

Fig. 3.34

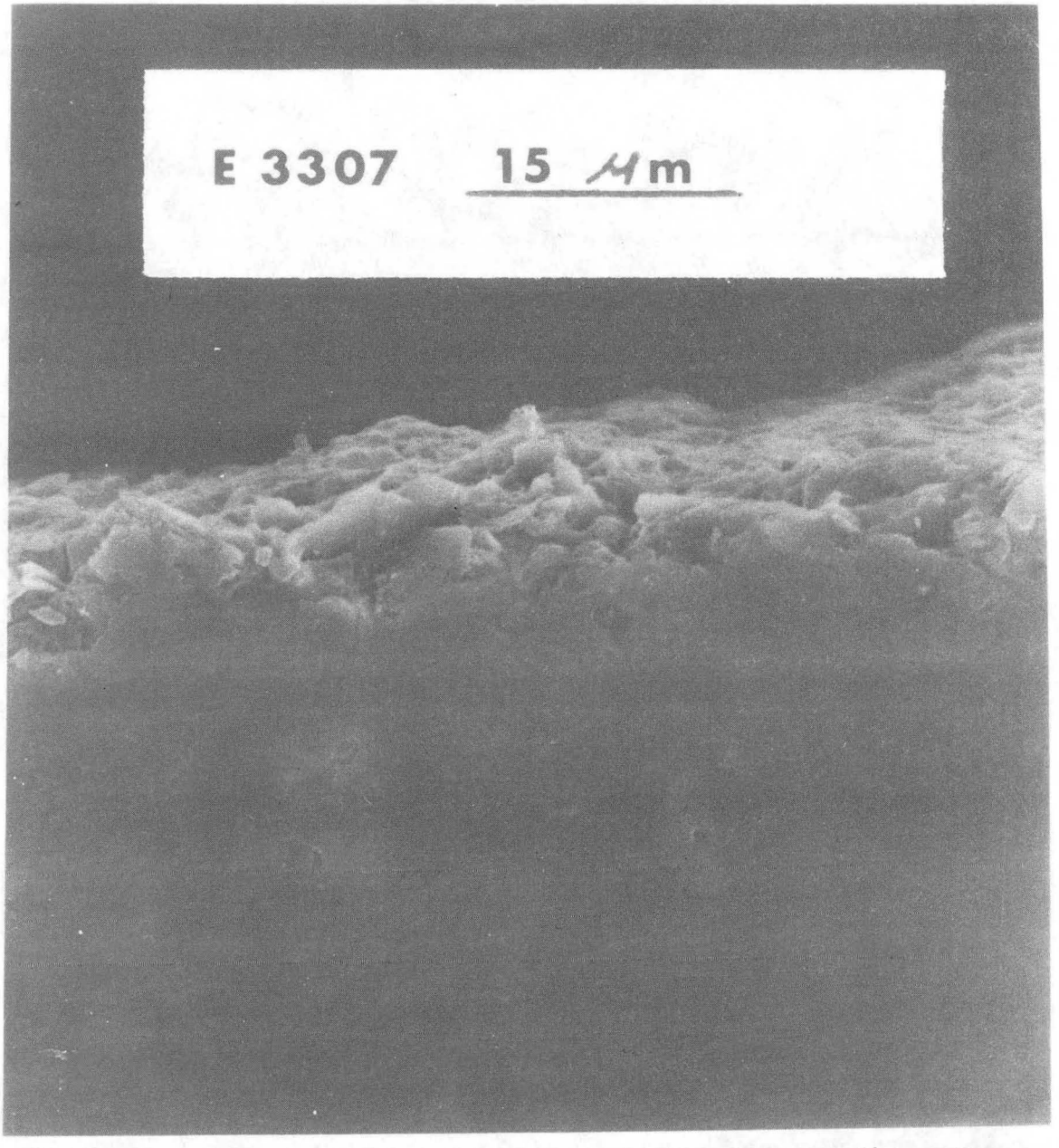

XBB 843-2039

Fig. 3.35

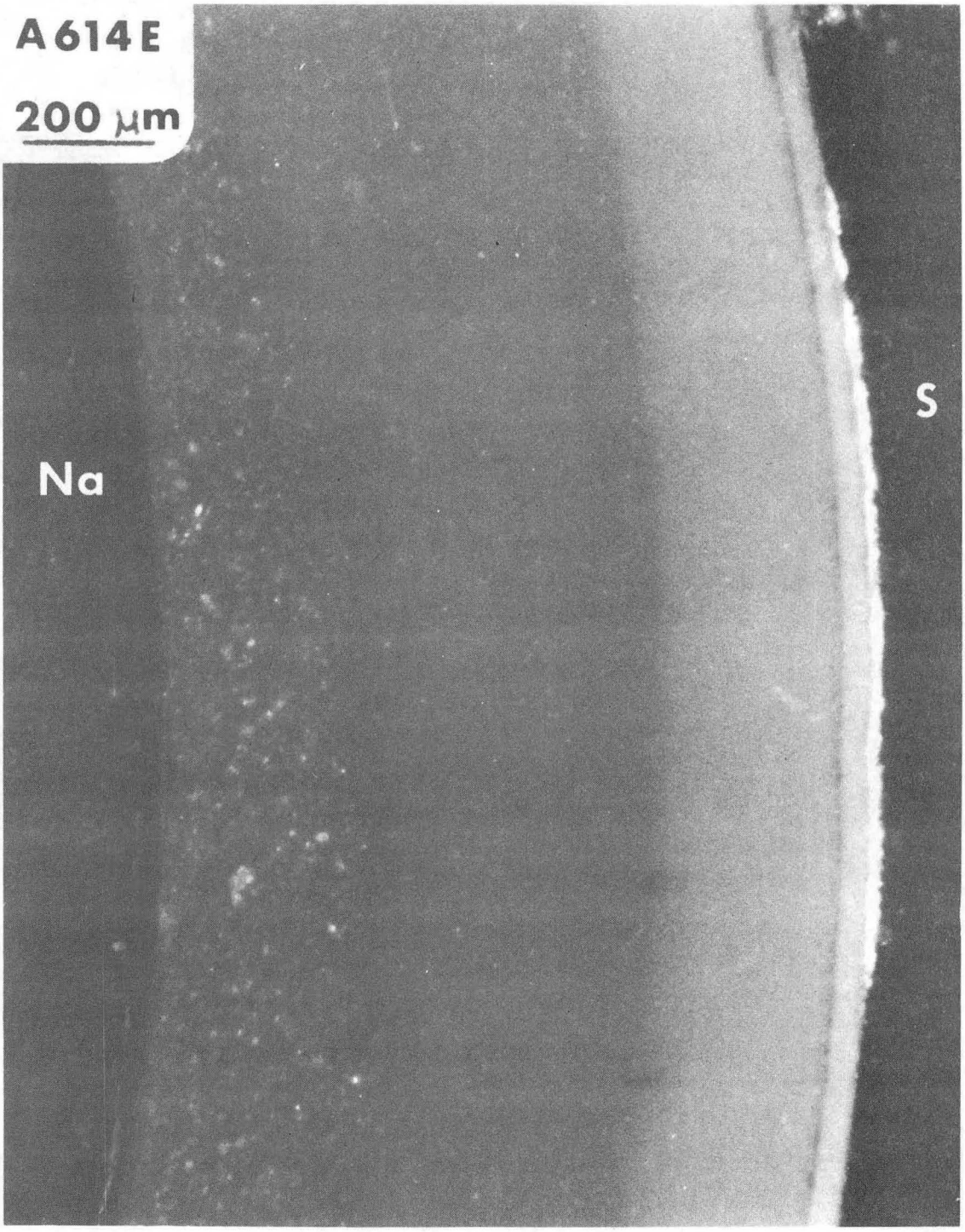

XBB 841-166

Fig. 3.36

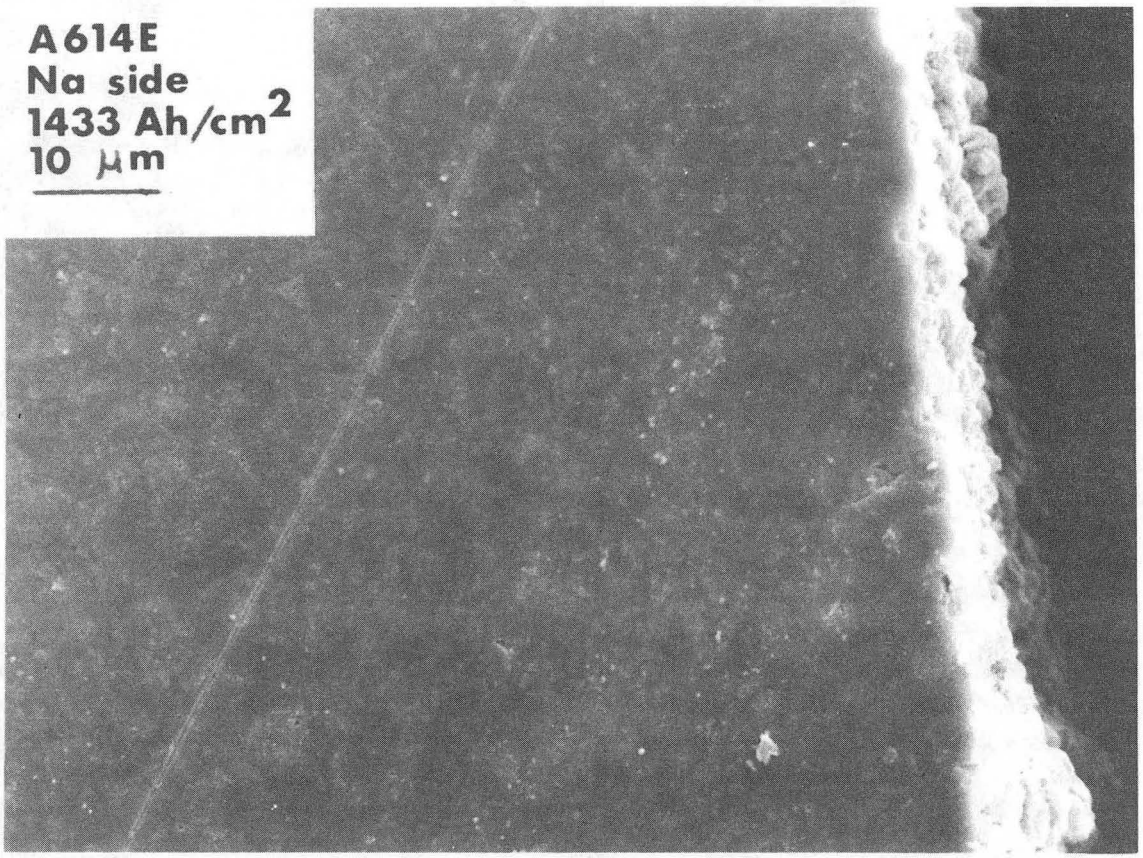

XBB 841-167

Fig. 3.37

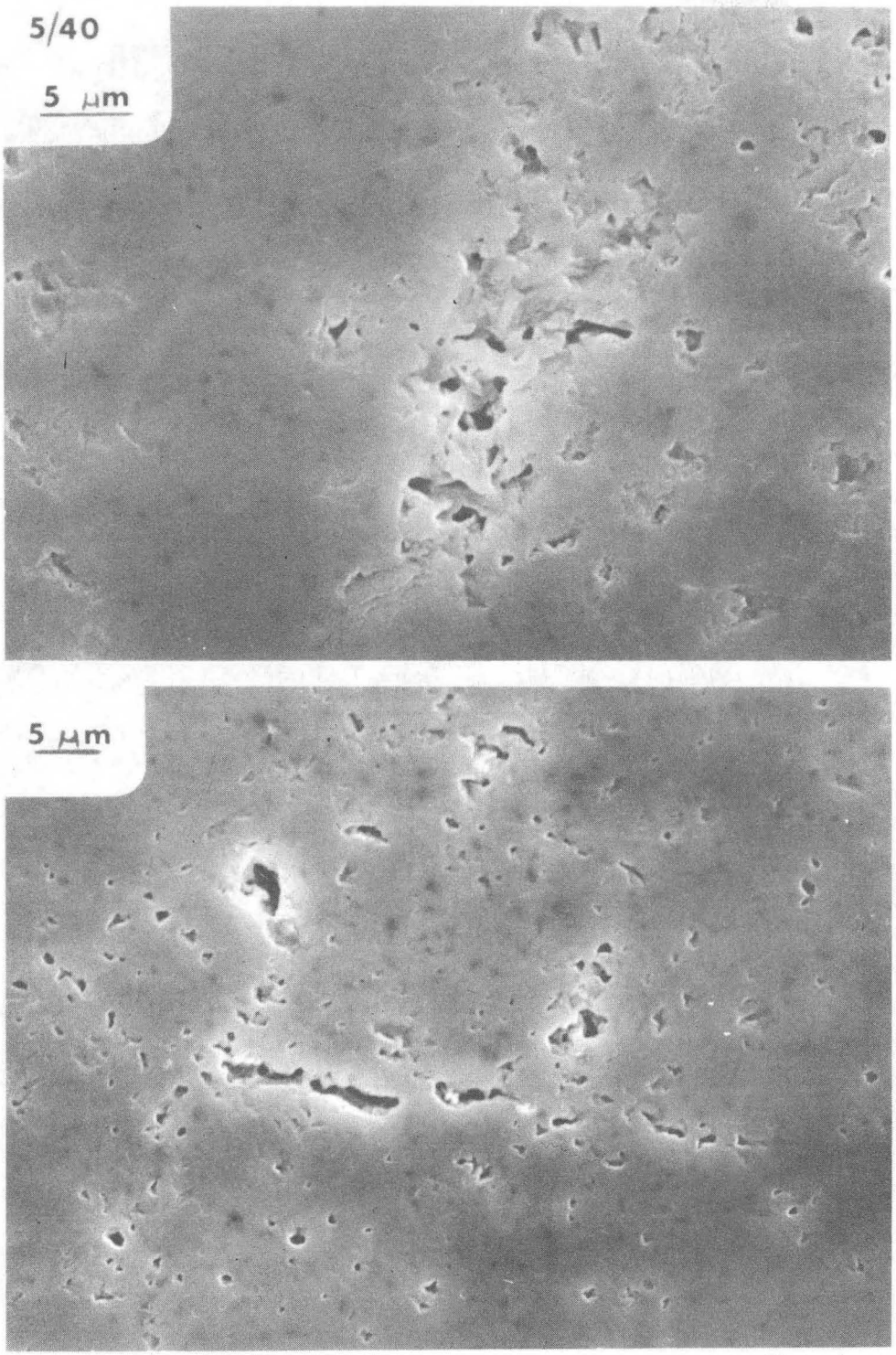

XBB 842-1415

Fig. 3.38

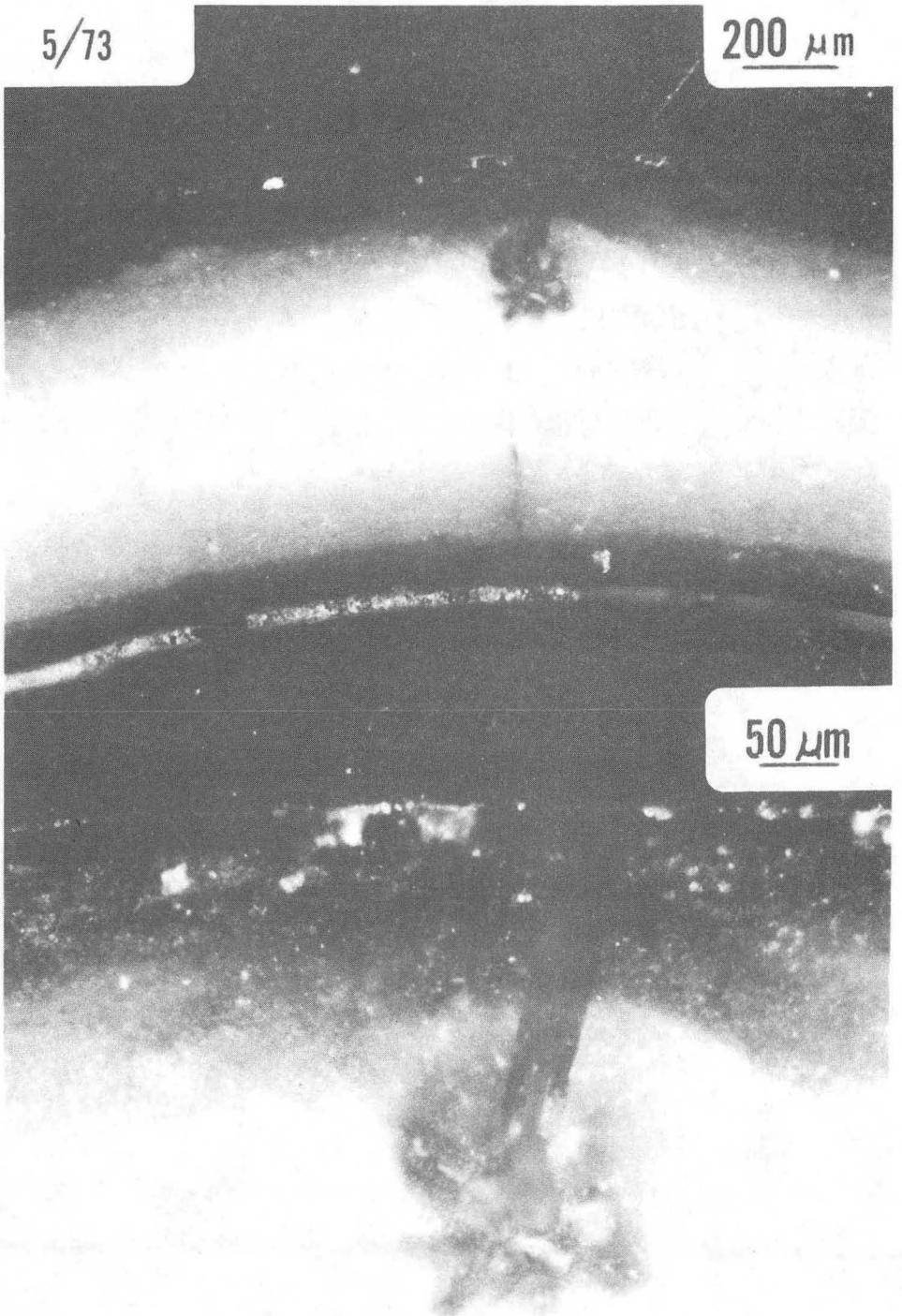

XBB 847-5136

Fig. 3.39

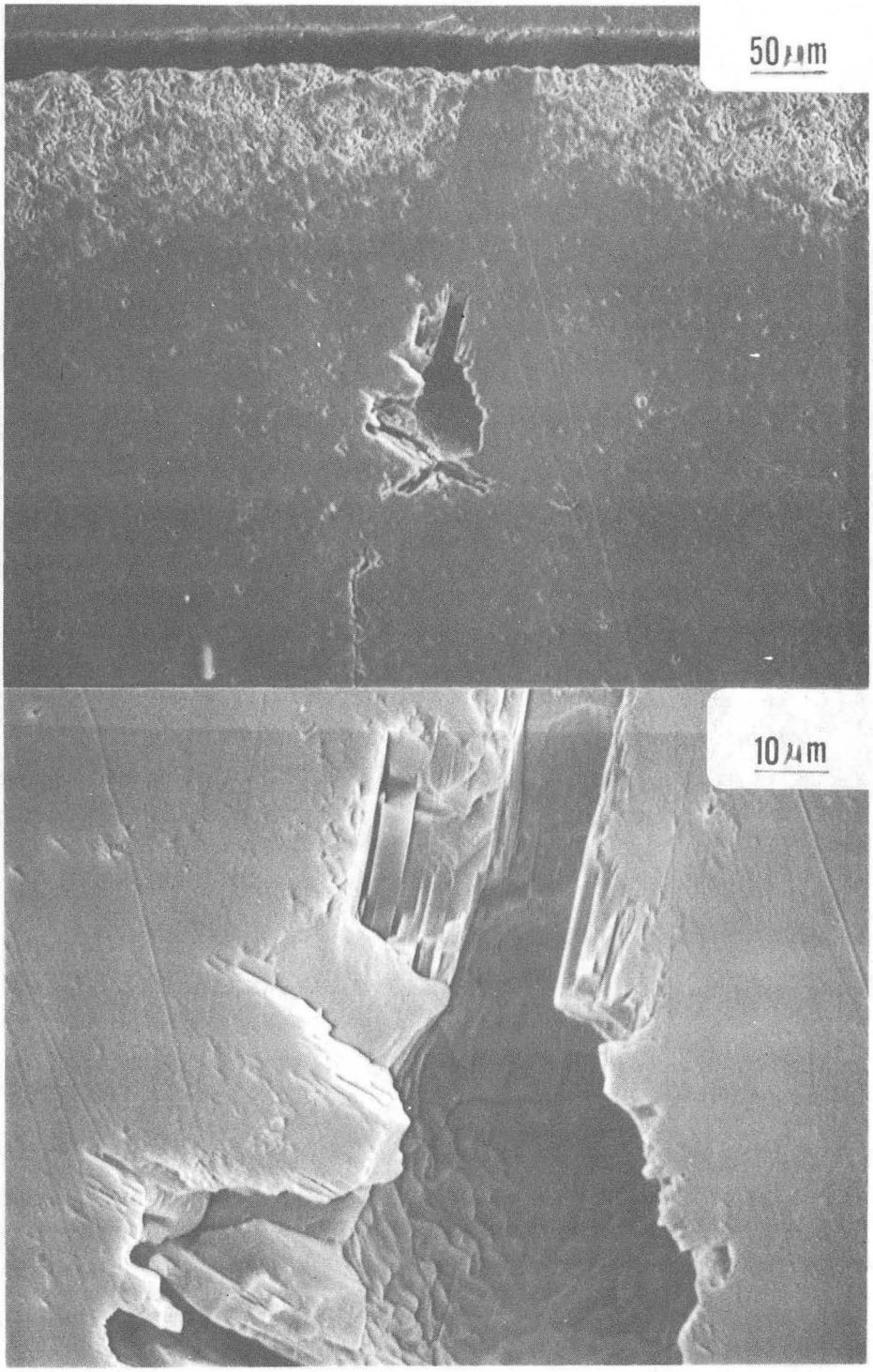

XBB 847-5138

Fig. 3.40

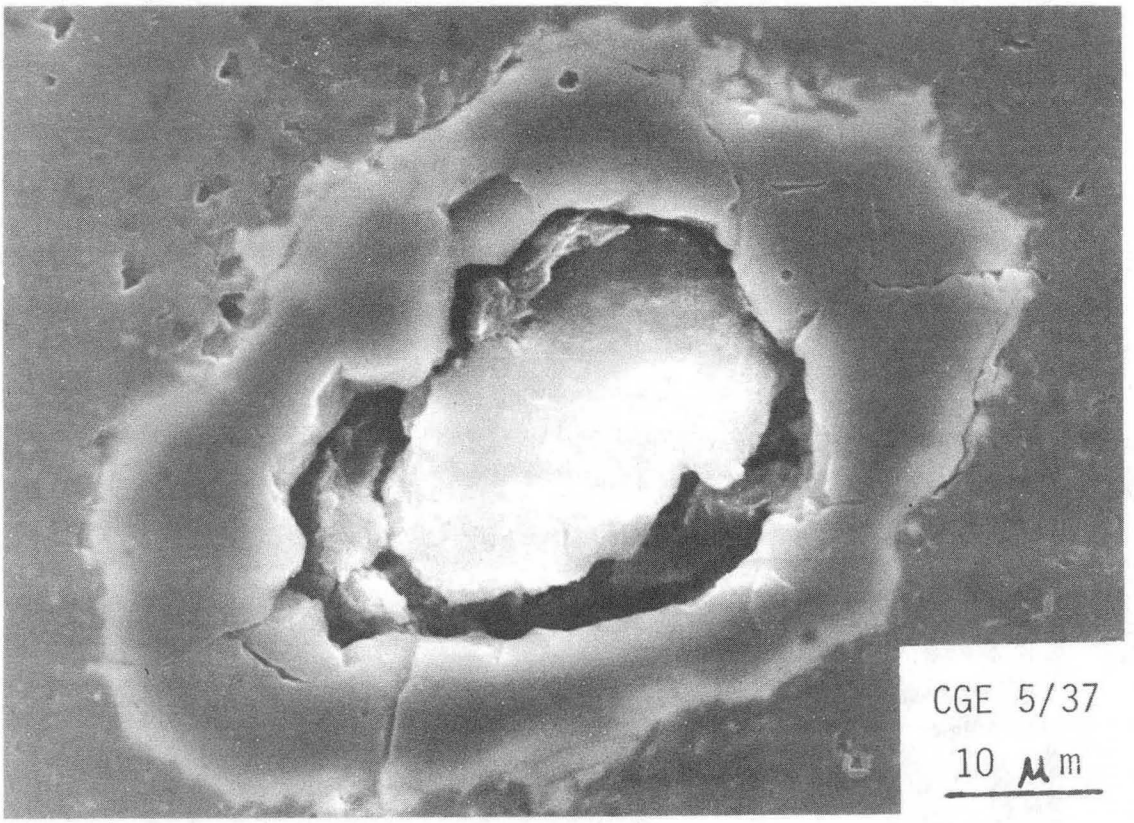

XBB 836-5179

Fig. 3.41

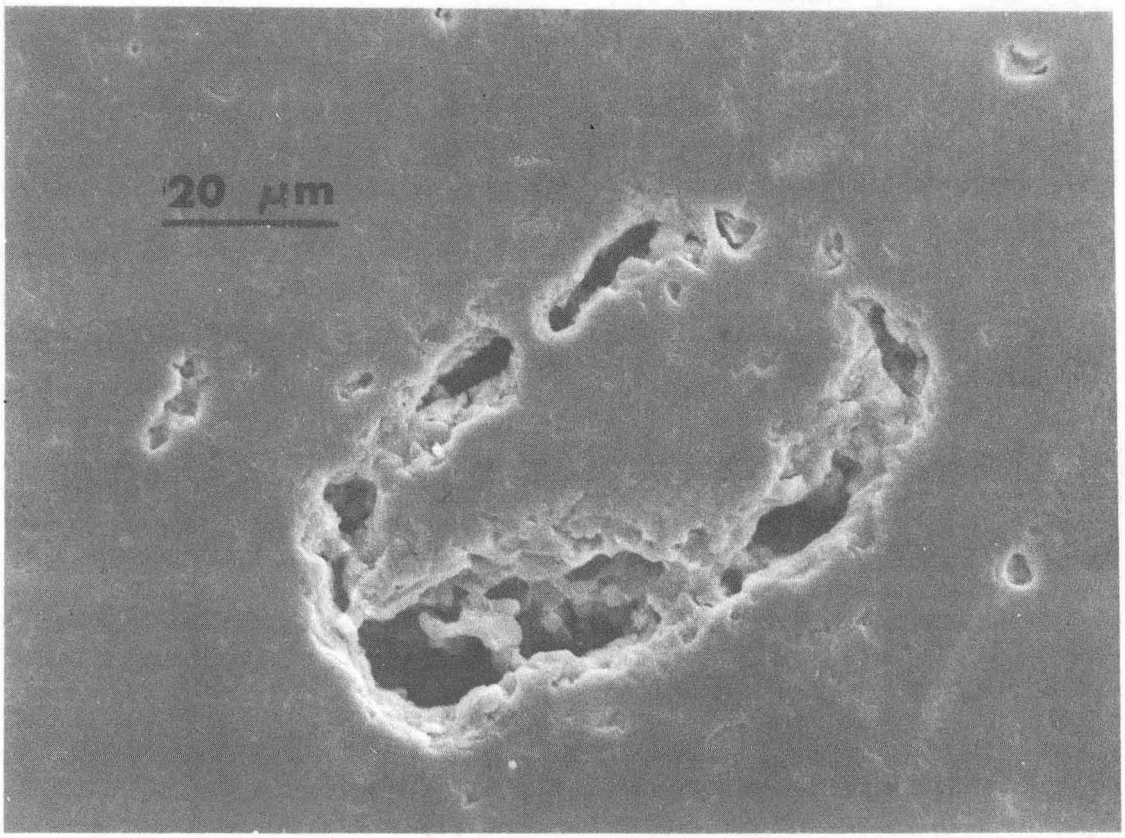

XBB 844-2825

Fig. 3.42

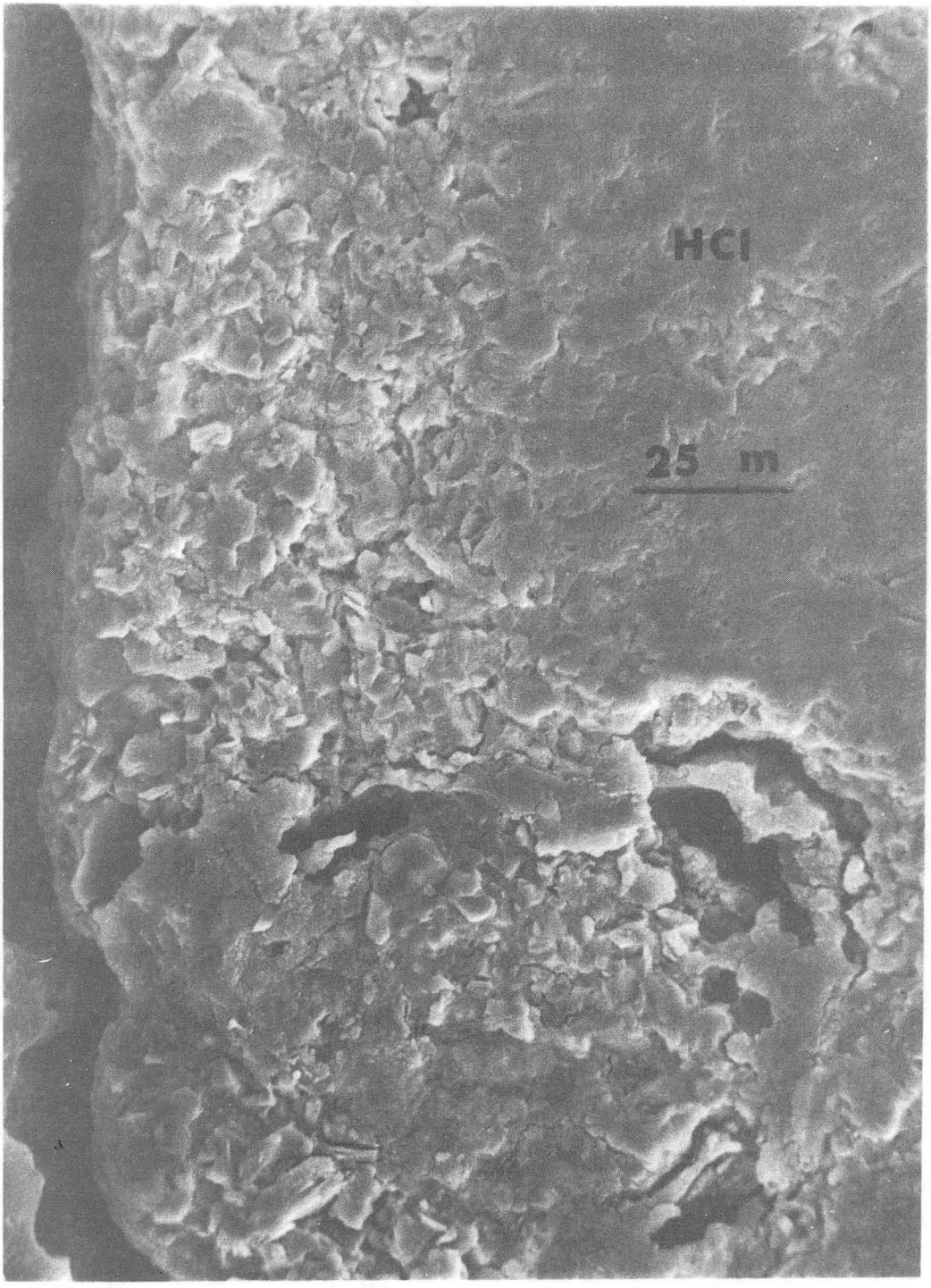

XBB 844-2835

Fig. 3.43

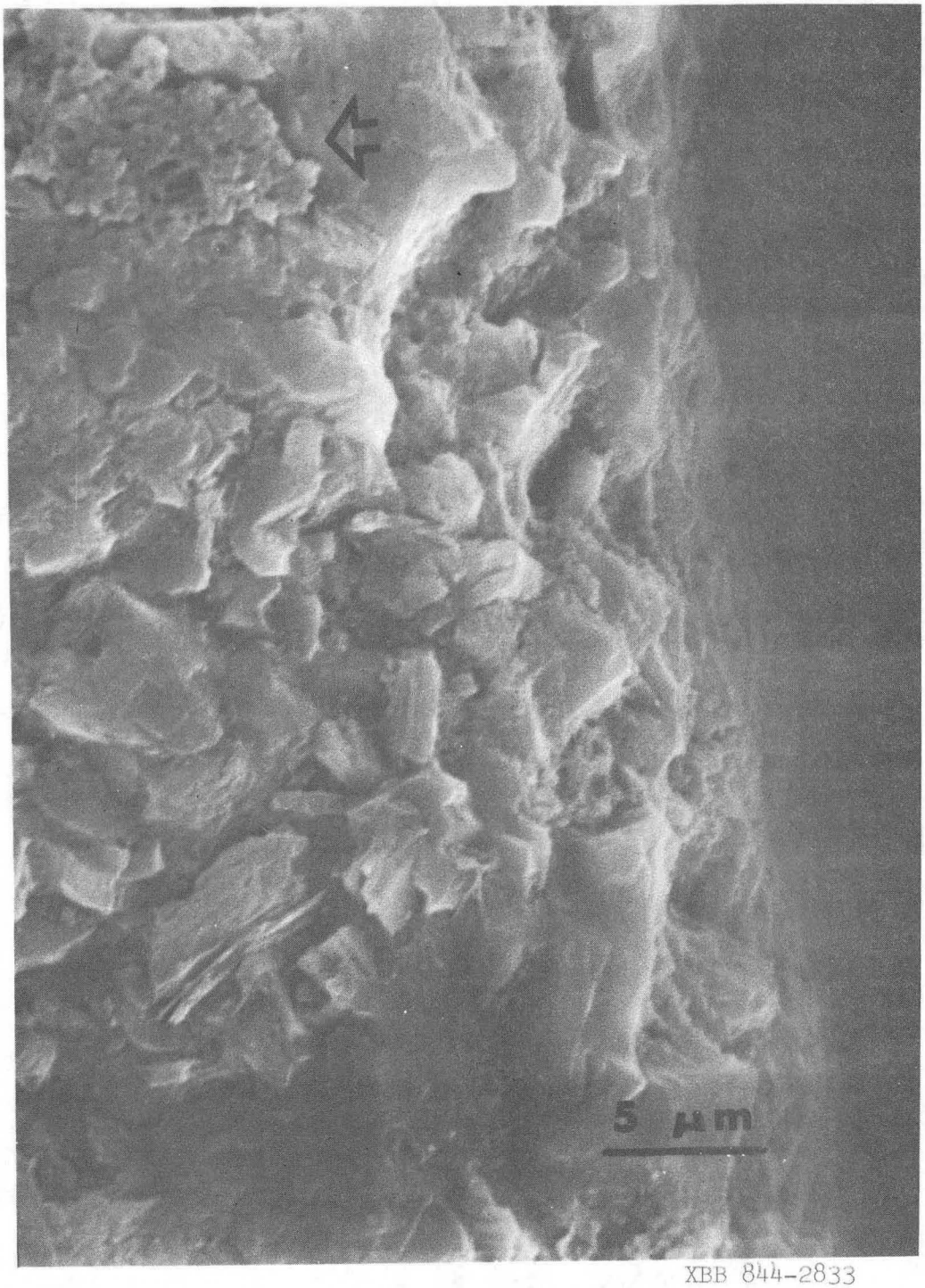

XBB 844-2833

Fig. 3.44

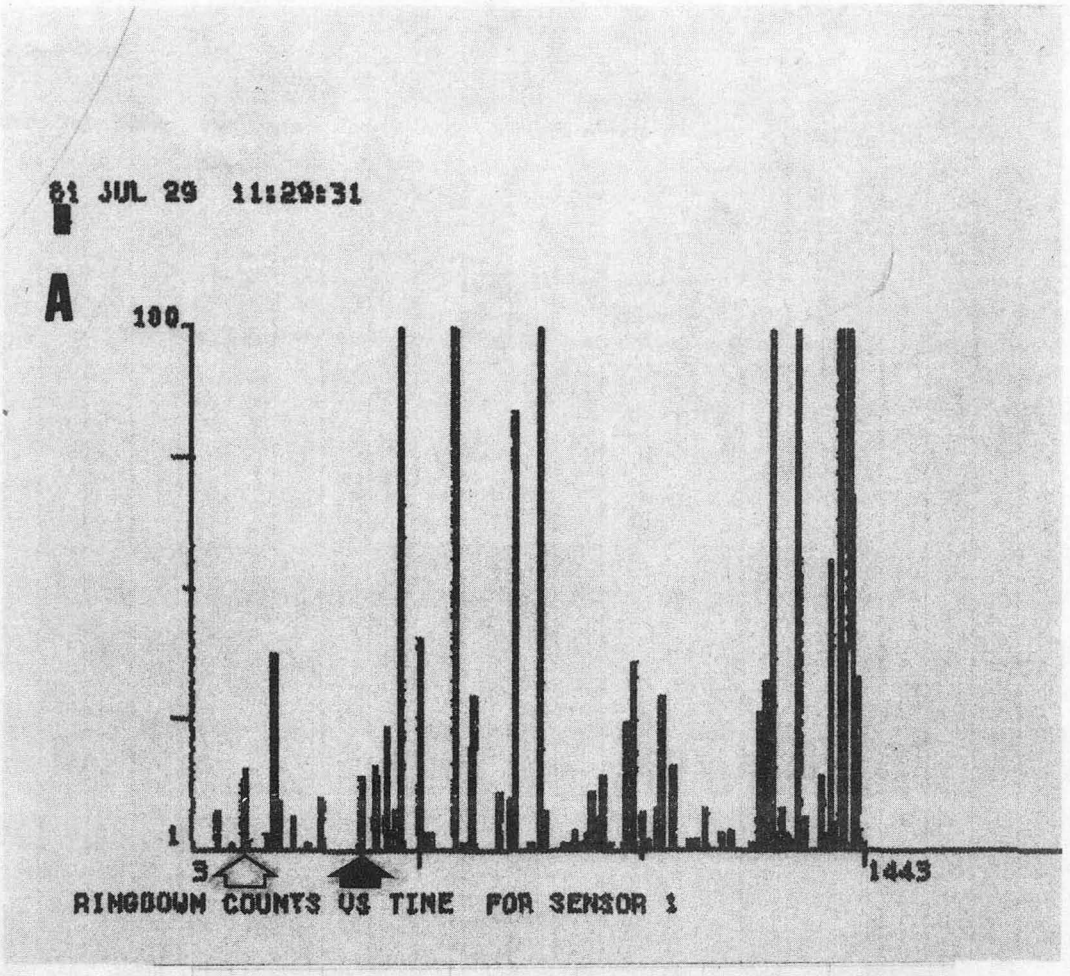

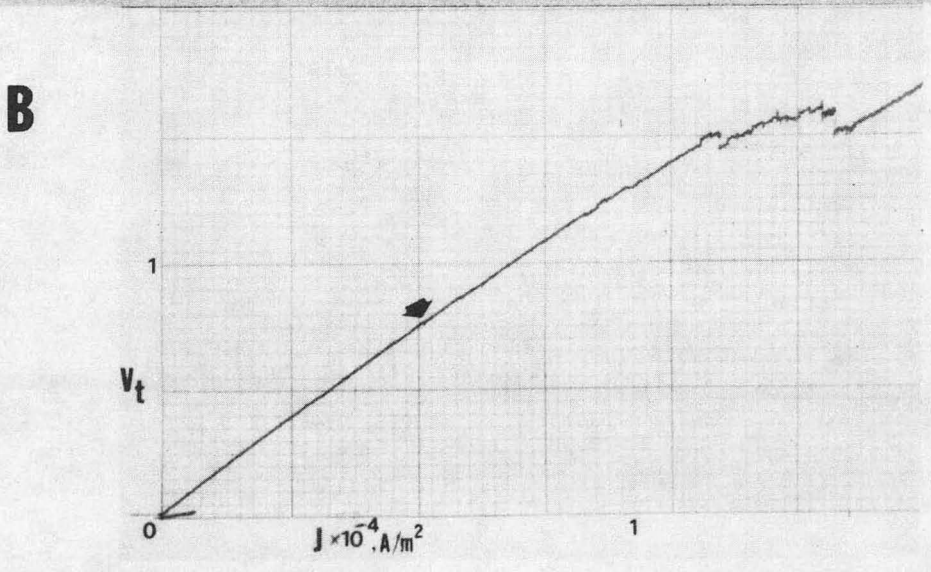

XBB 840-7762

Fig. 4.1

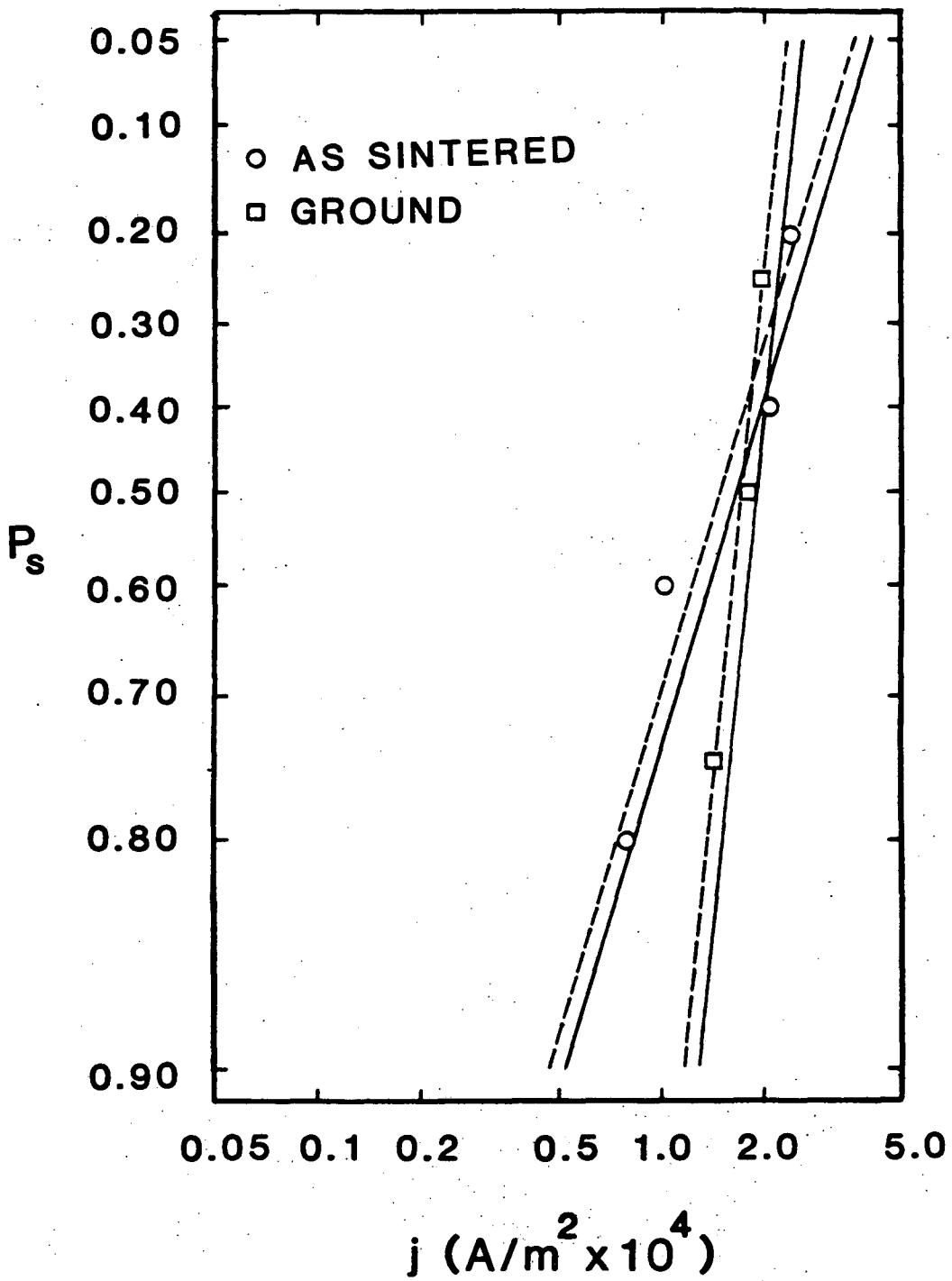

XBL 8411-4846

Fig. 4.2

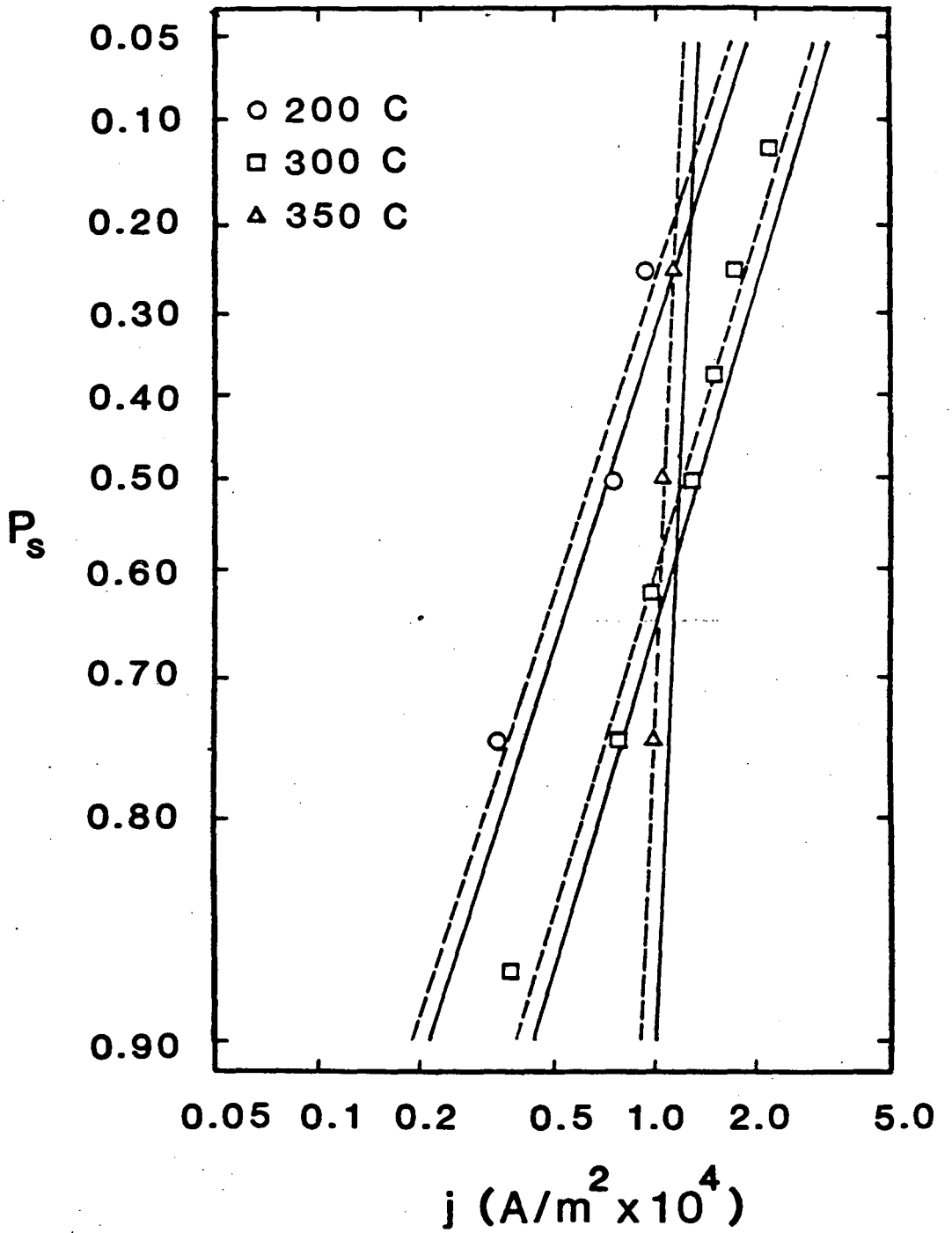

XBL 8411-4845

Fig. 4.3

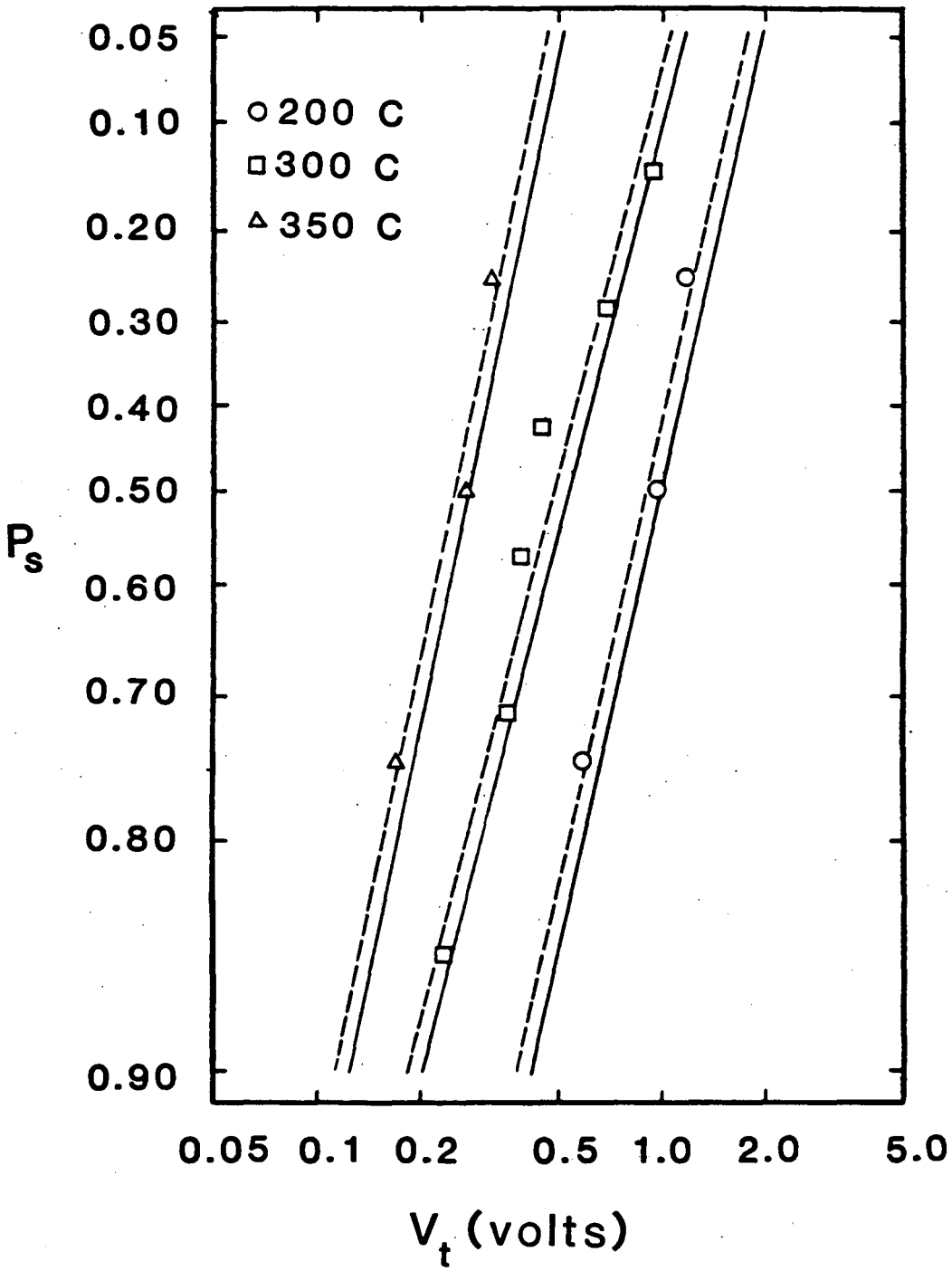

XBL 8411-4850

Fig. 4.4

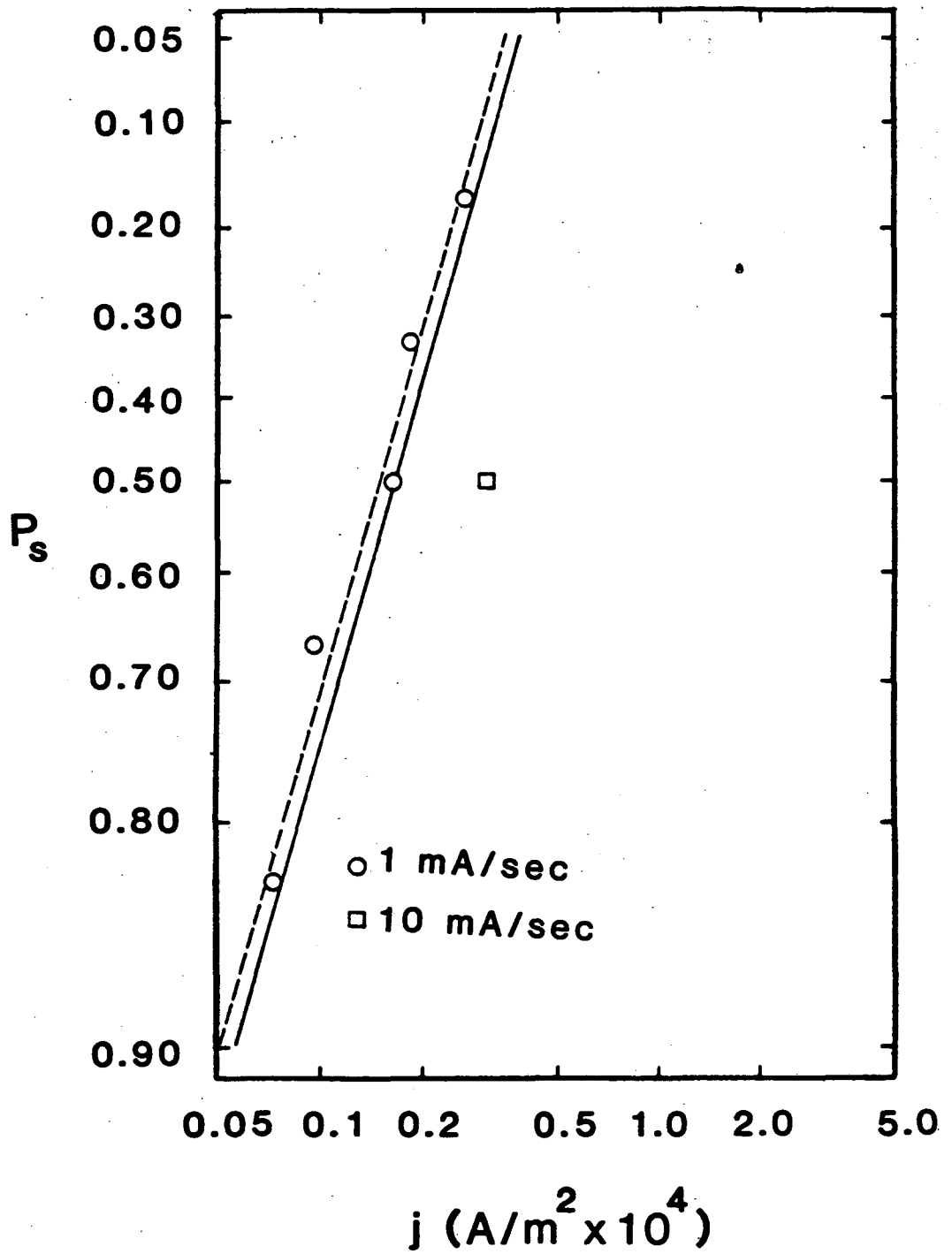

XBL 8411-4849

Fig. 4.5

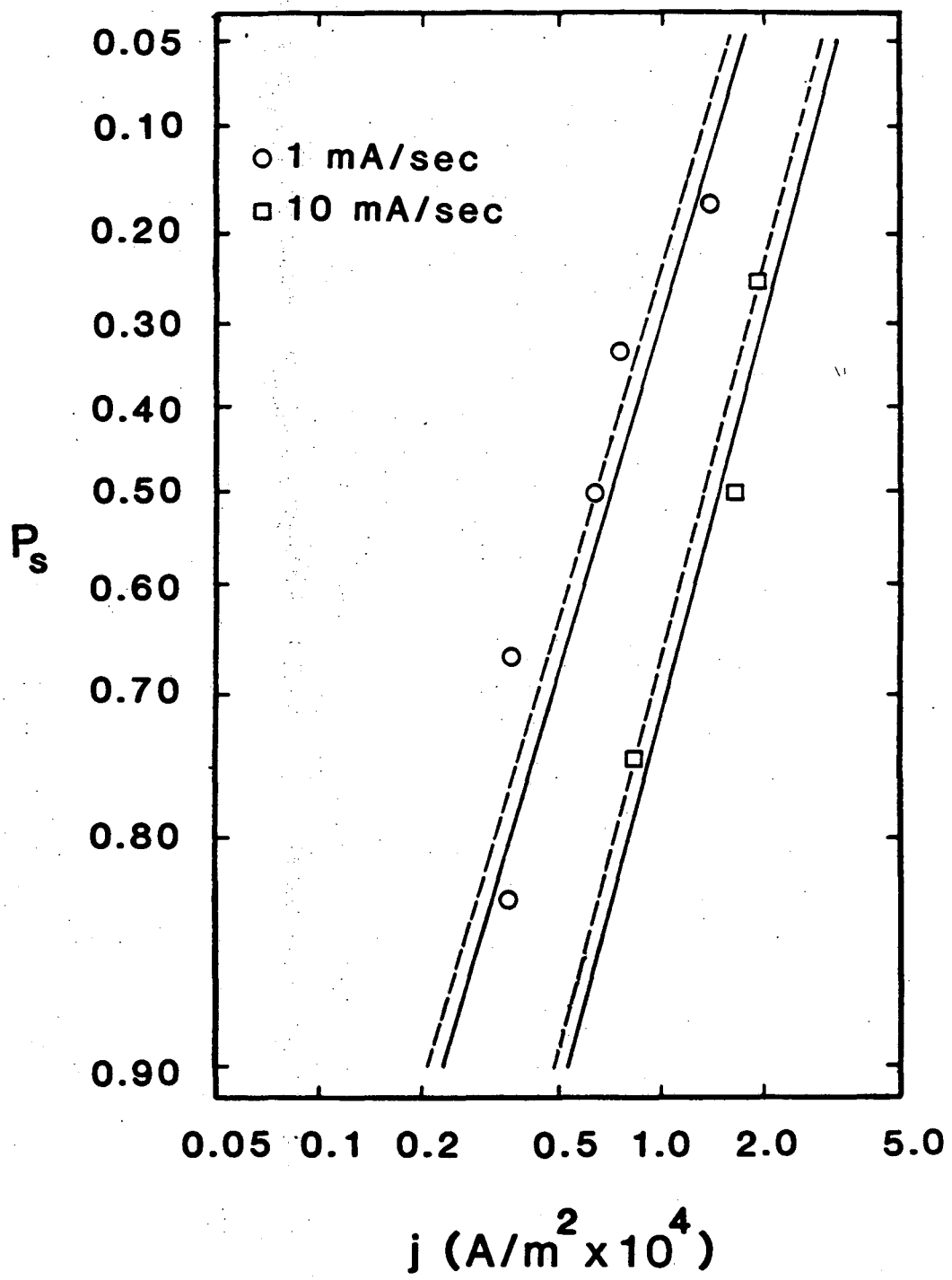

XBL 8411-4848

Fig. 4.6

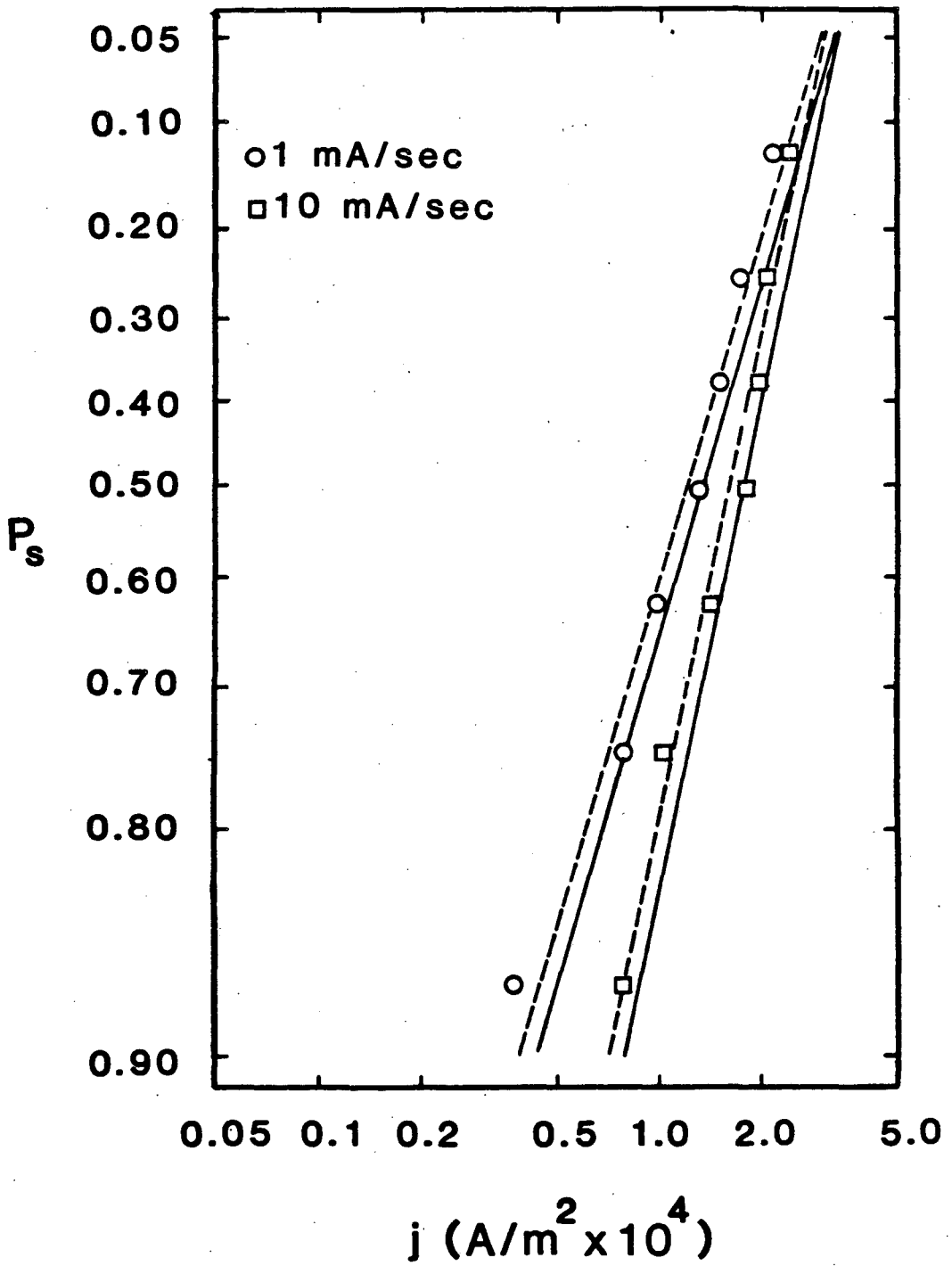

XBL 8411-4847

Fig. 4.7

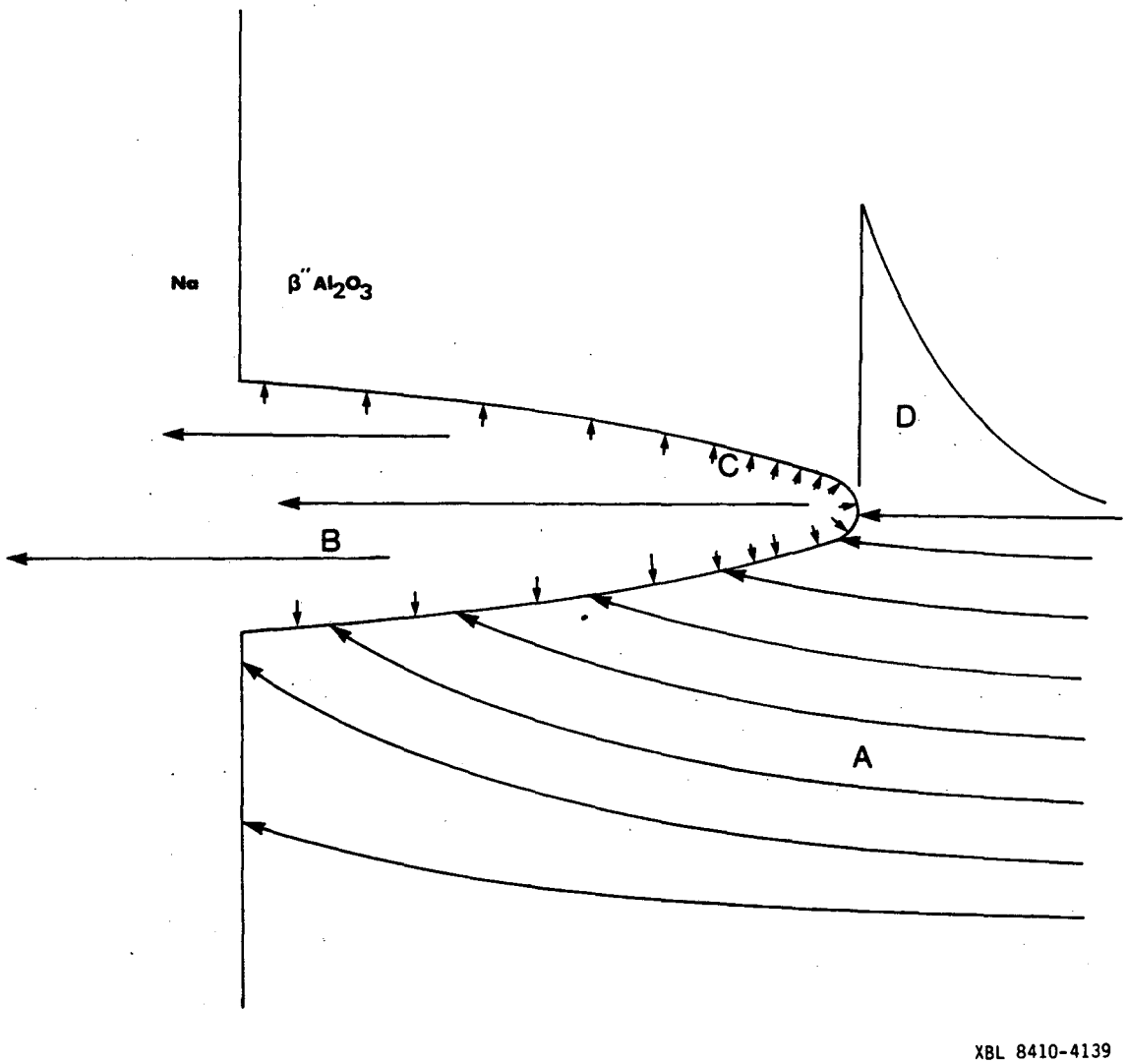

Fig. 5.1

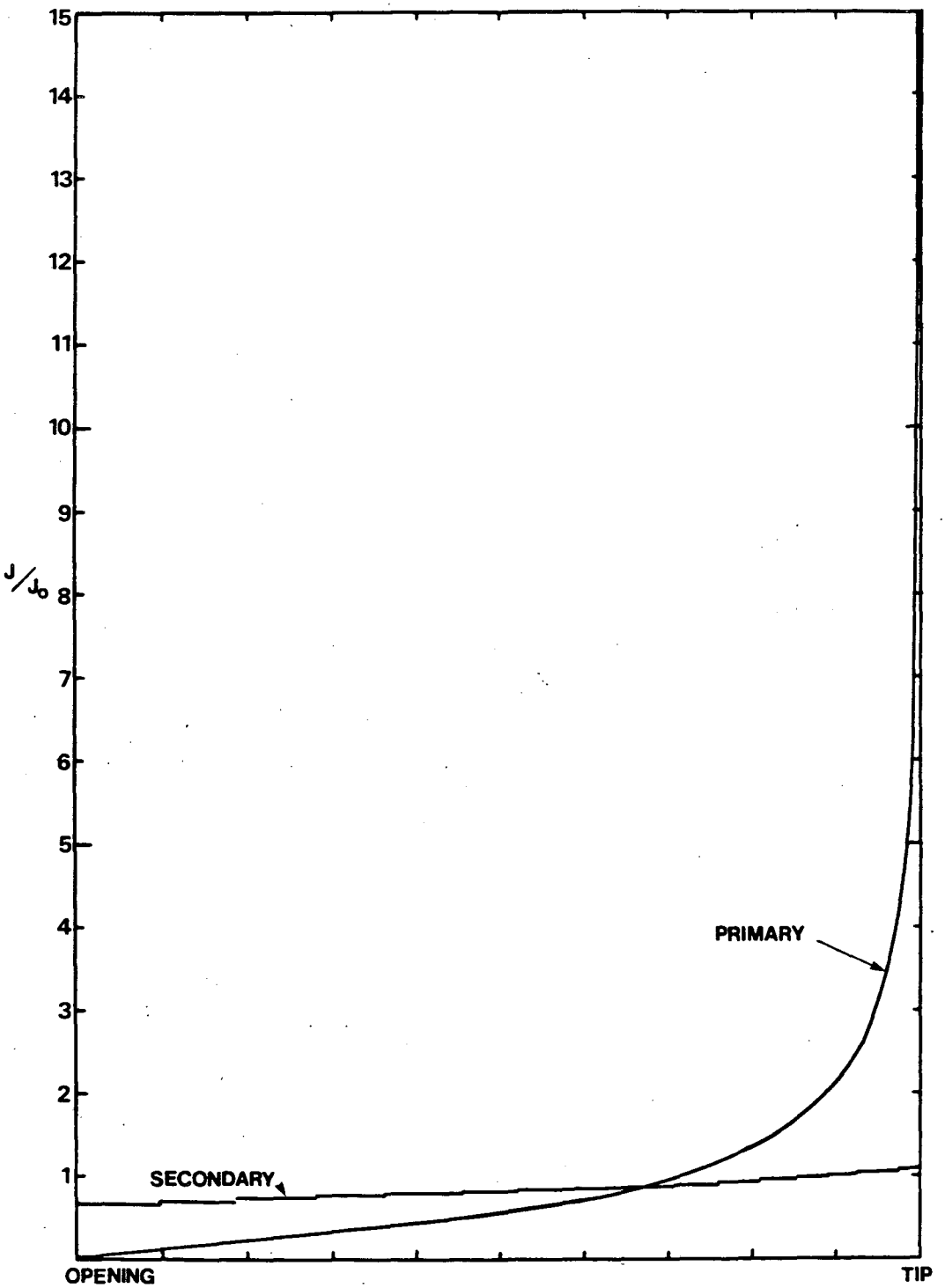
15
14
13
12
11
10
9
8
7
6
5
4
3
2
1
J/J0
PRIMARY
SECONDARY
OPENING
TIP
XBL 8411-4778

Fig. 5.2

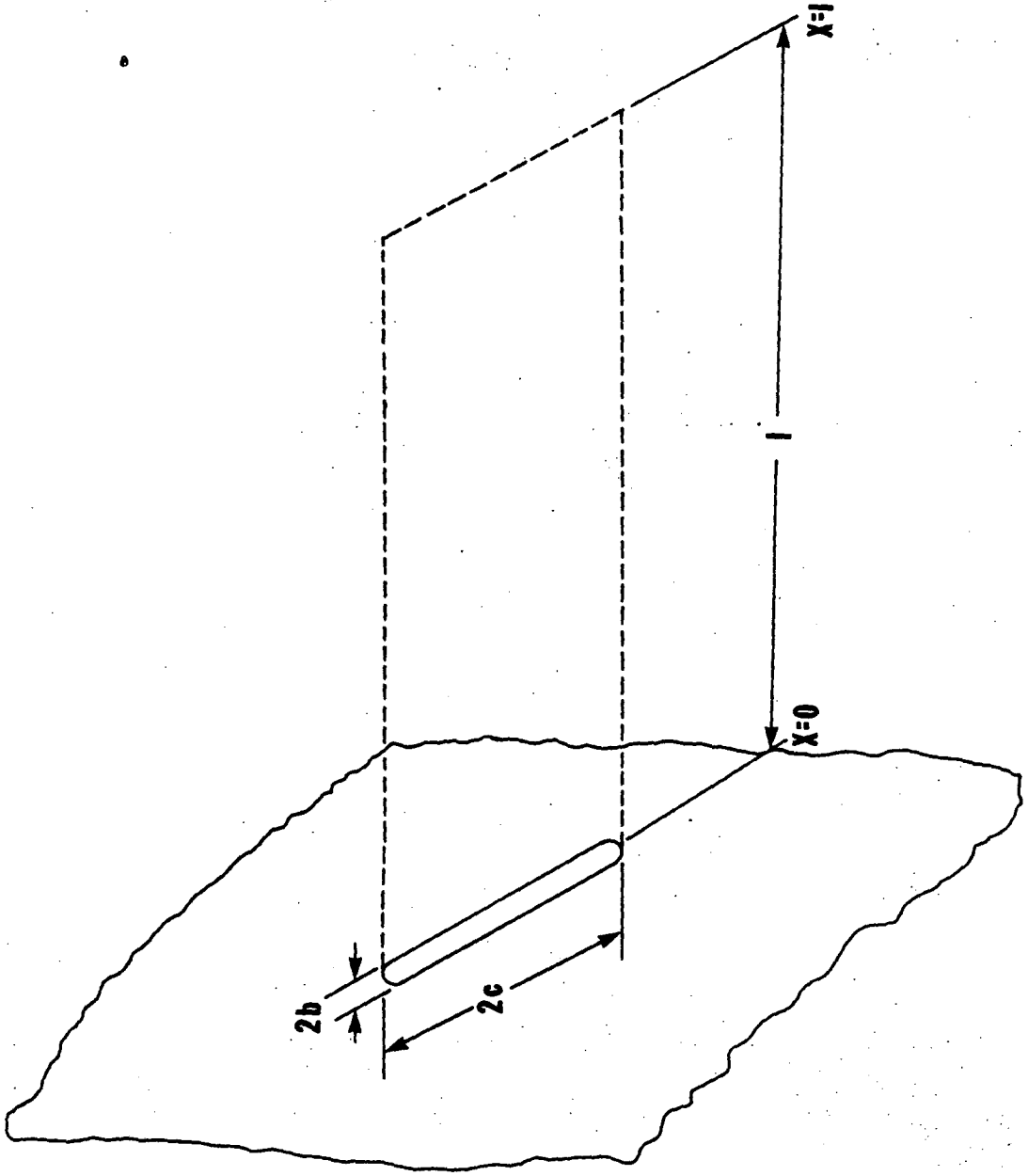

XBL 8410-4141

Fig. 5.3

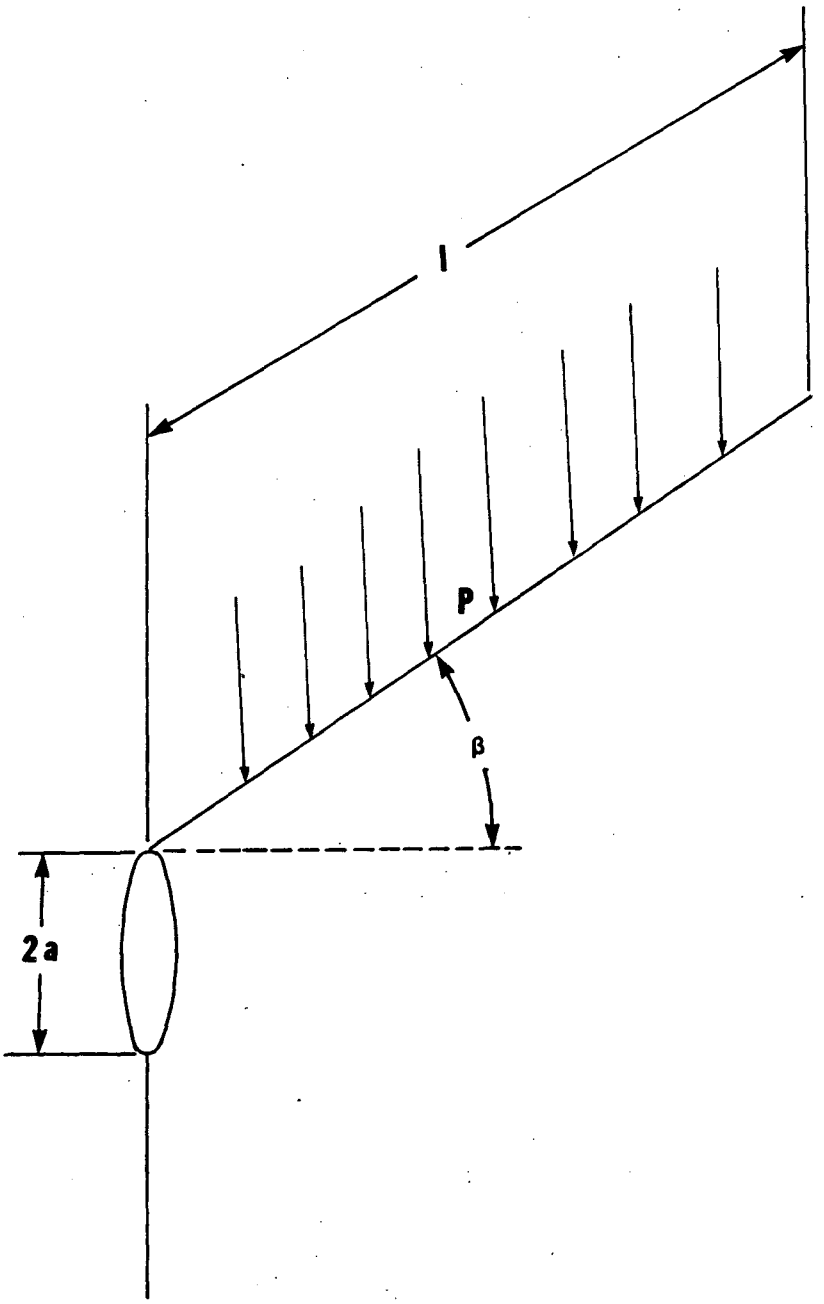

XBL 8410-4138

Fig. 5.4

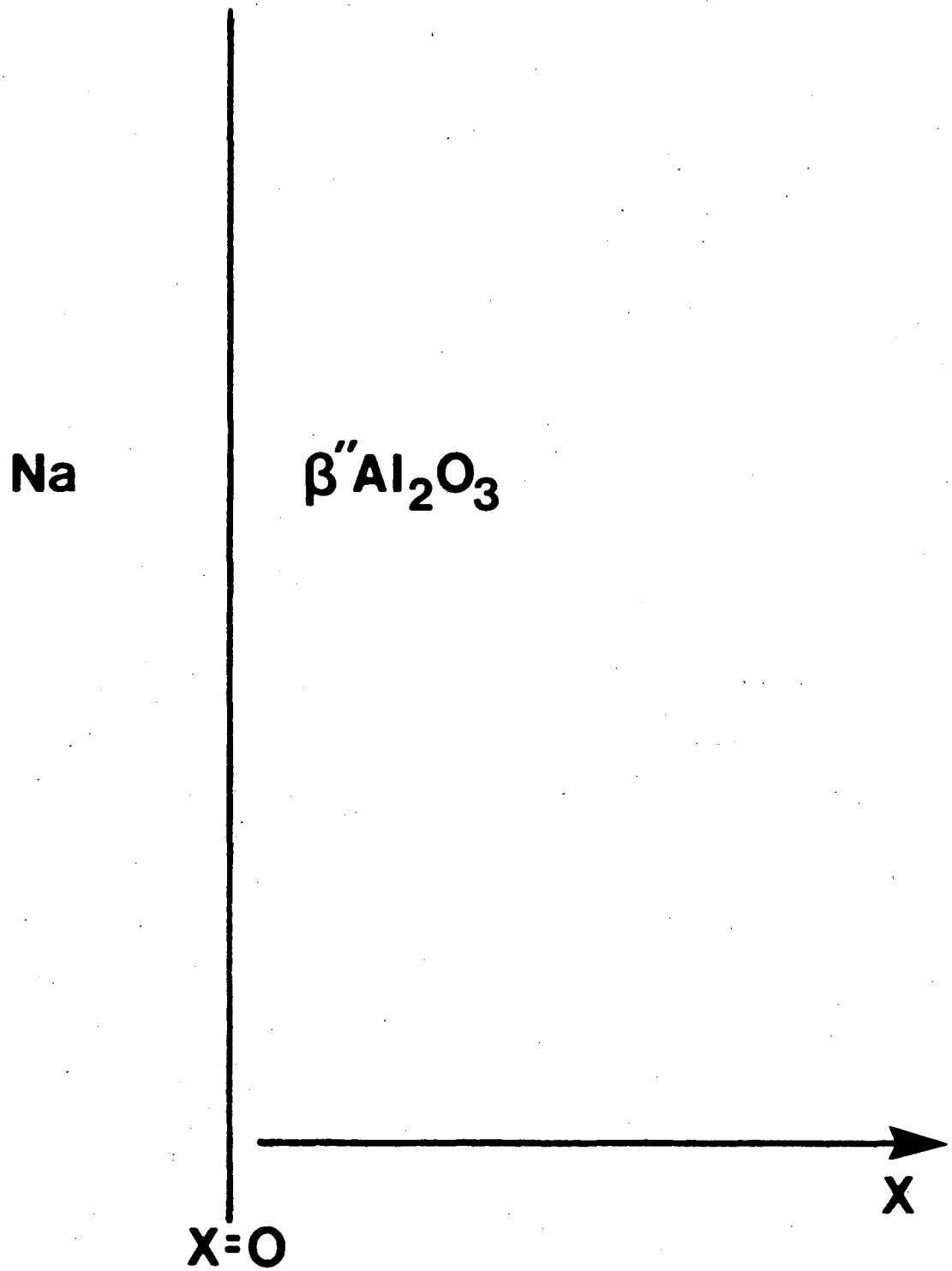

XBL 8411-4775

Fig. 6.1

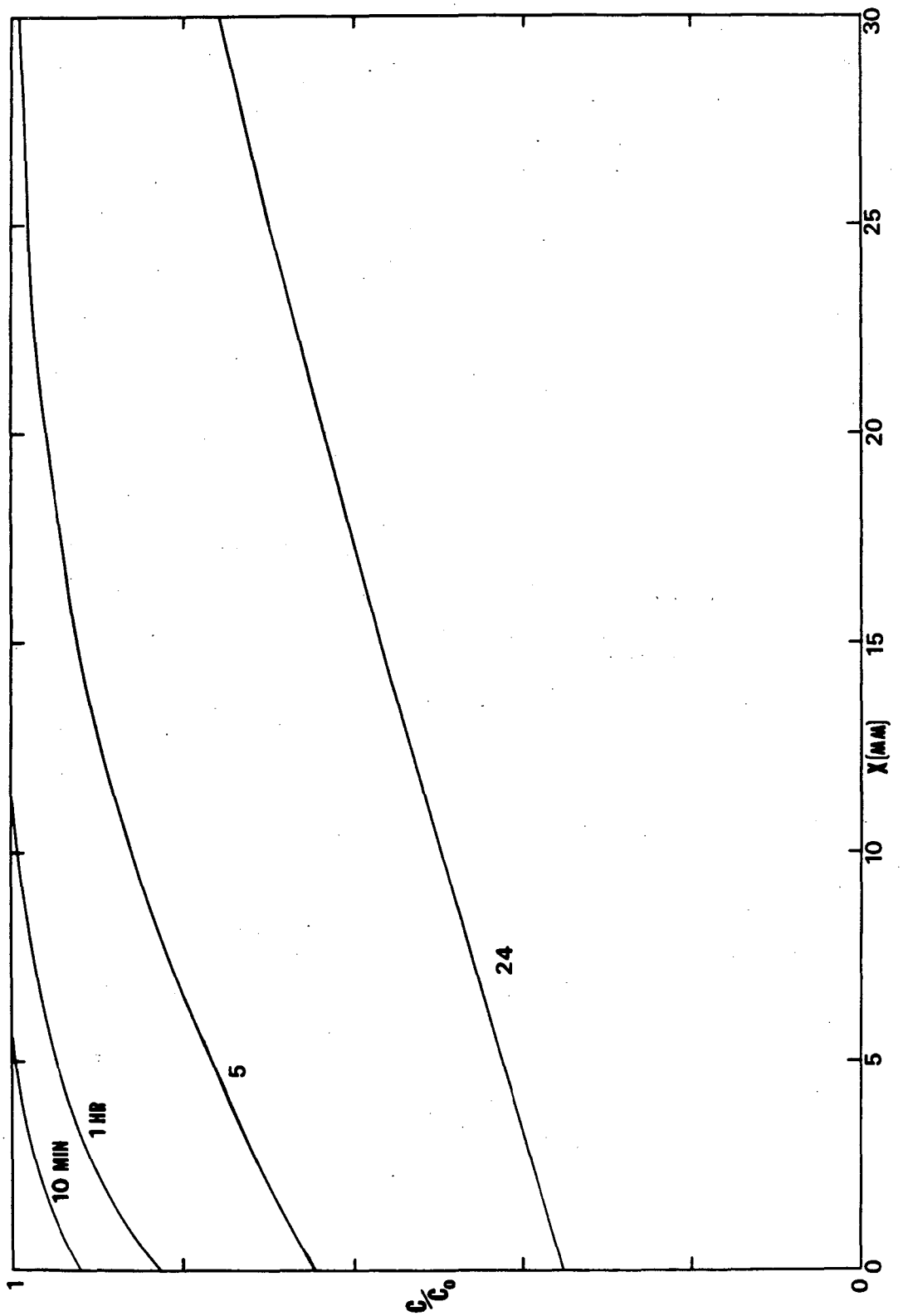

XBL 8411-4782

Fig. 6.2

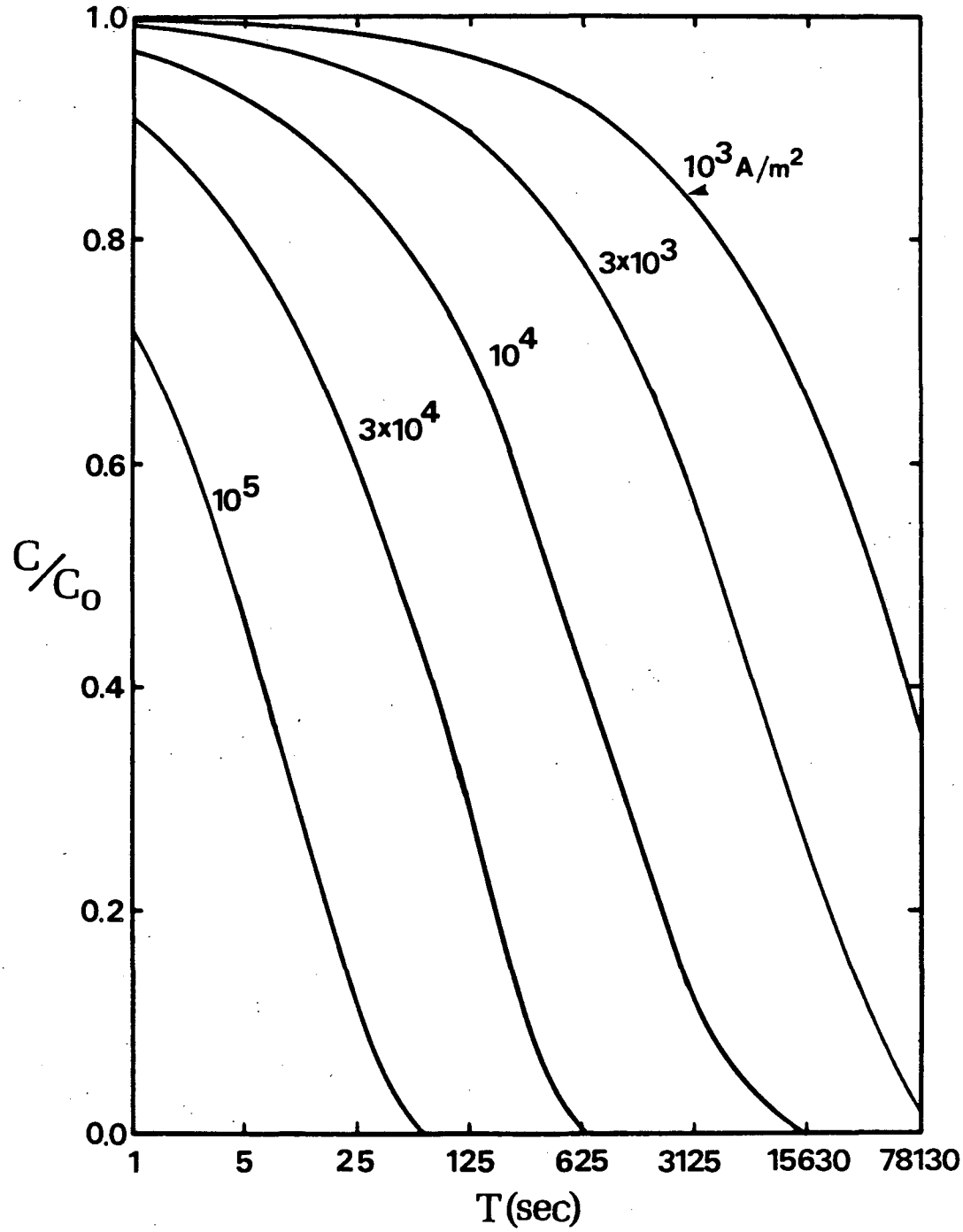

XBL 8411-4780

Fig. 6.3

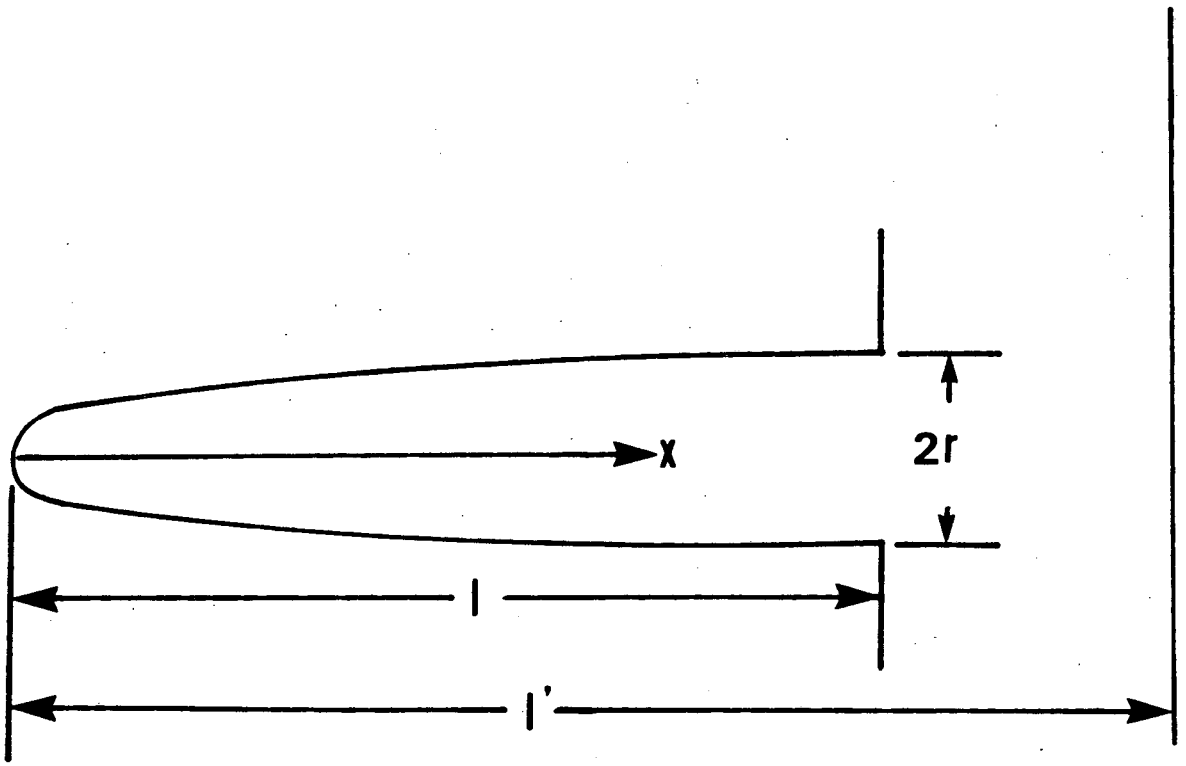

XBL 8411-4776

Fig. 6.4

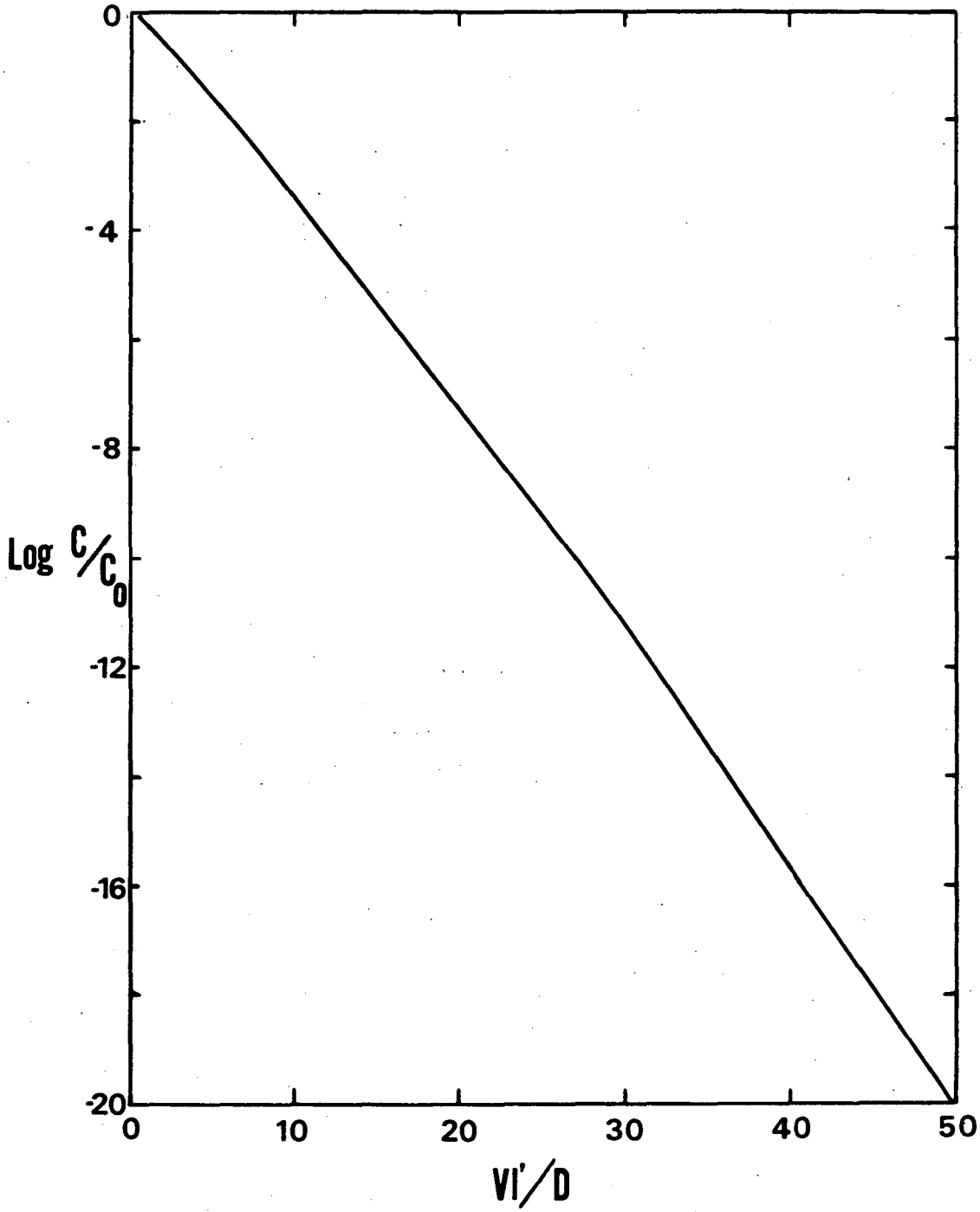

XBL 8411-4779

Fig. 6.5

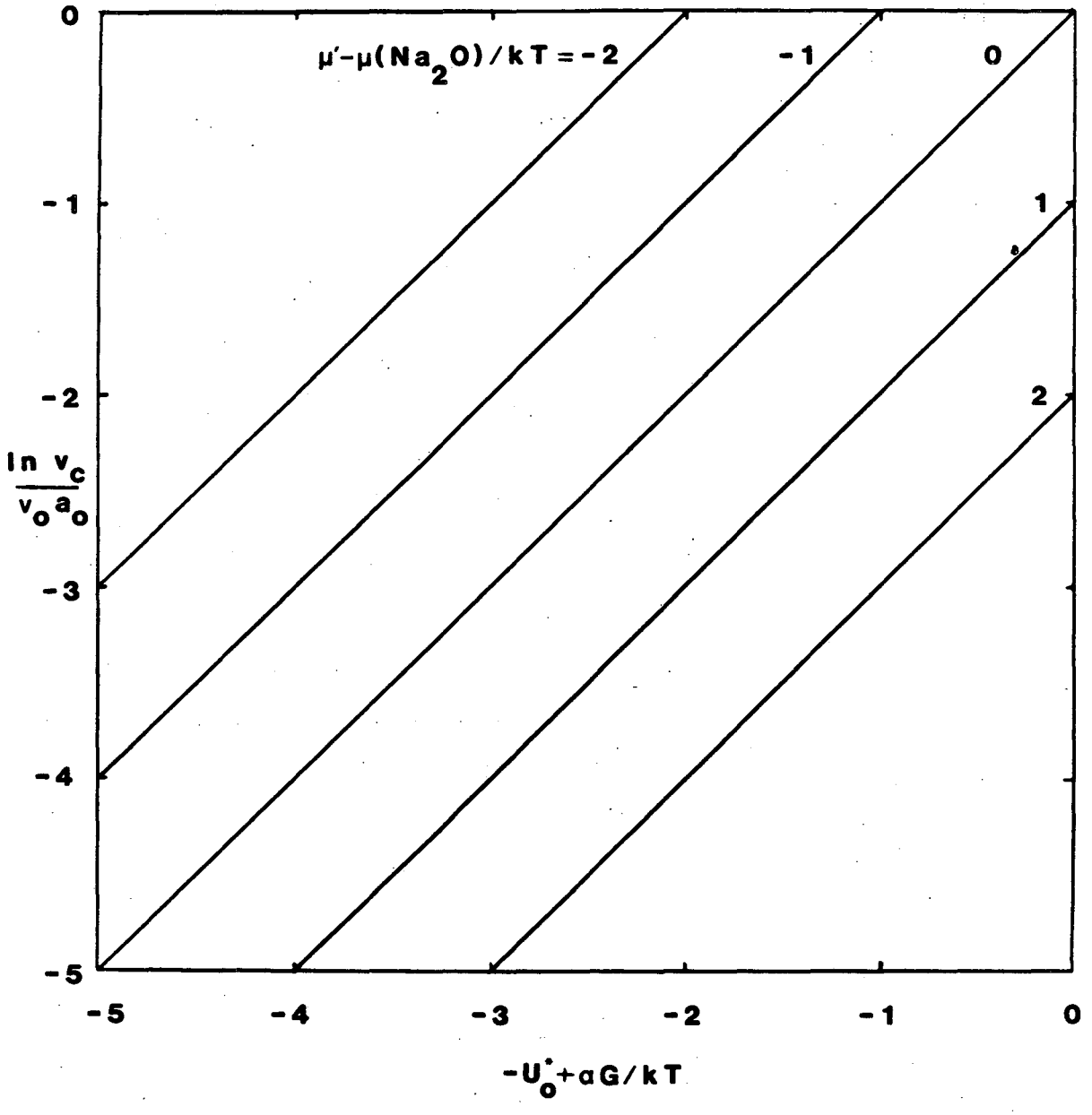

XBL 8411-4863

Fig. 6.6

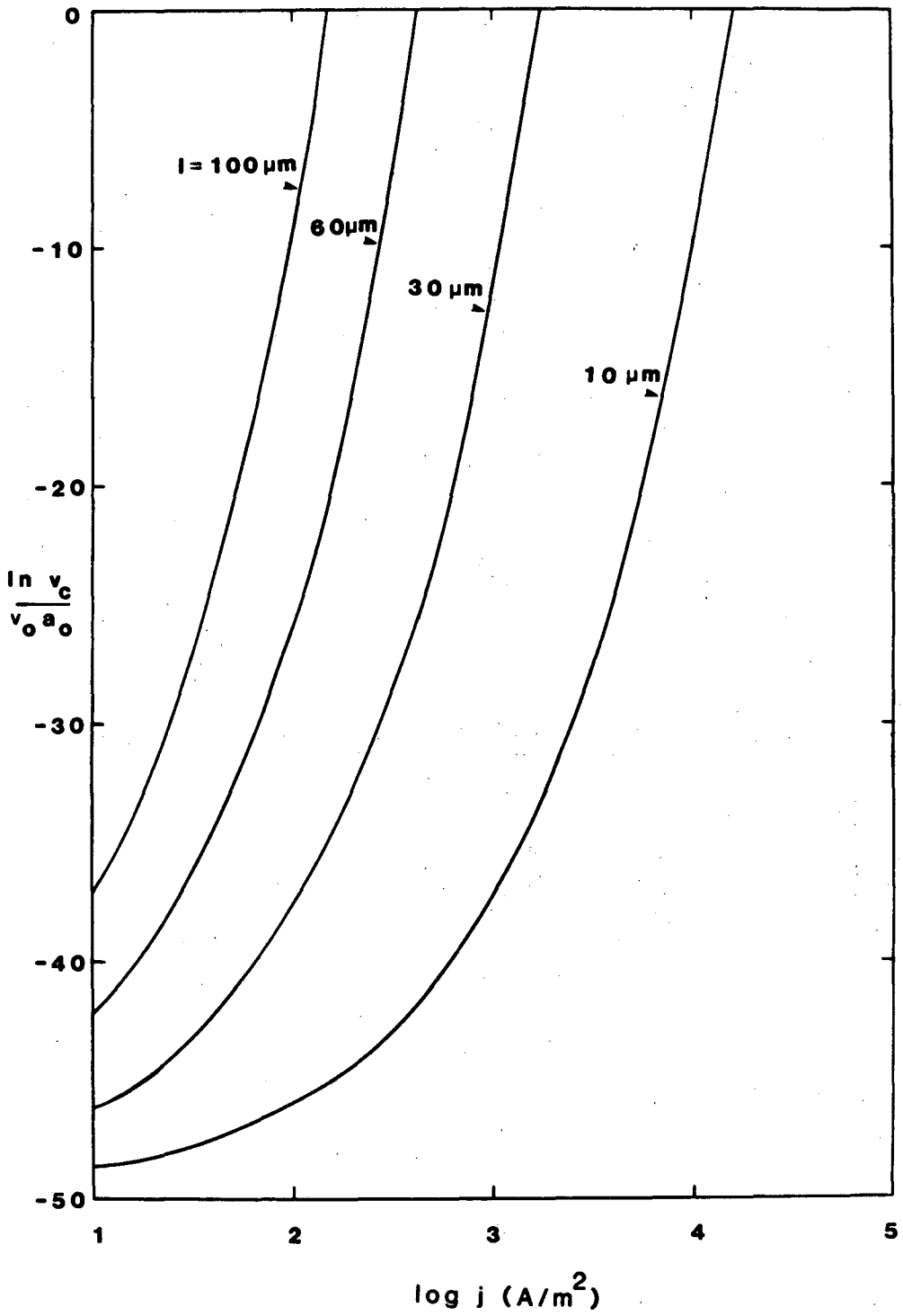

XBL 8411-4864

Fig. 6.7

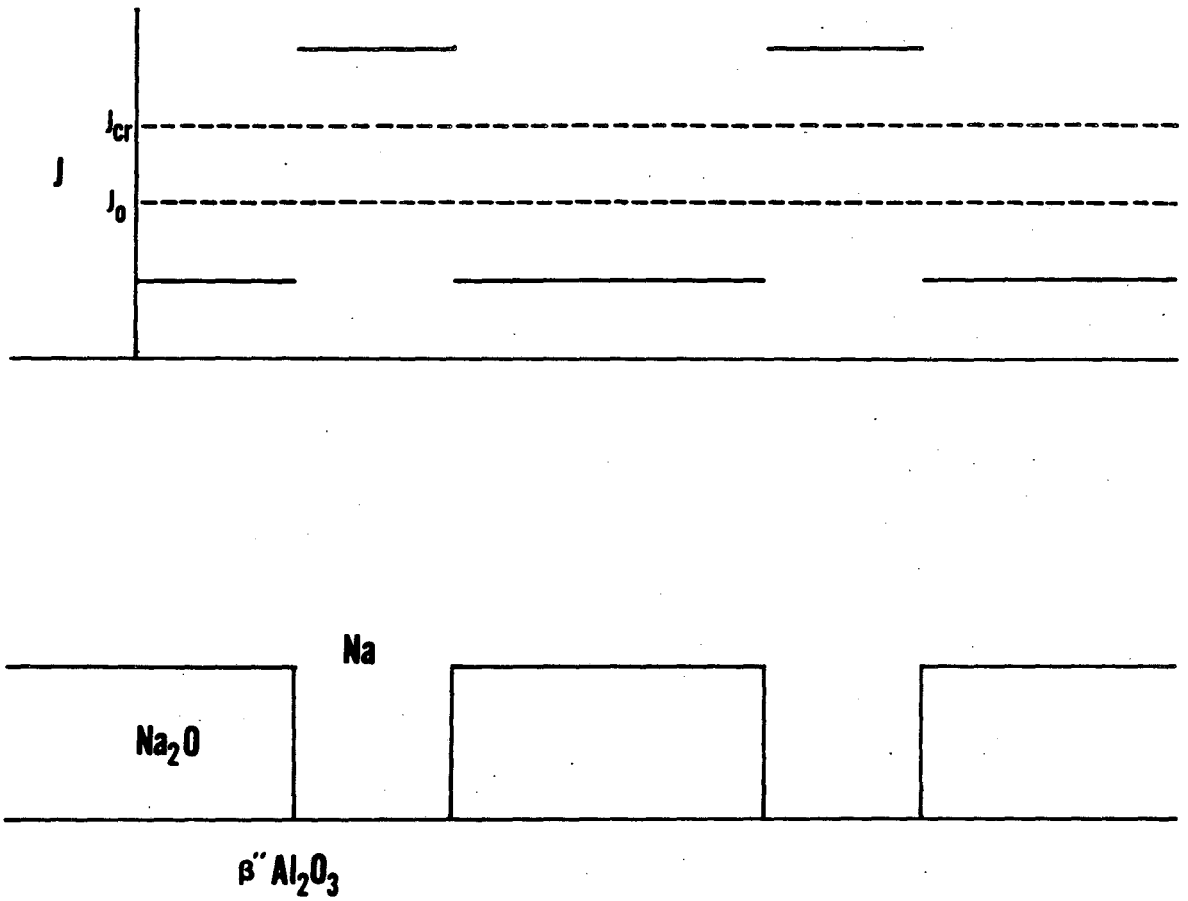

Fig. 6.8

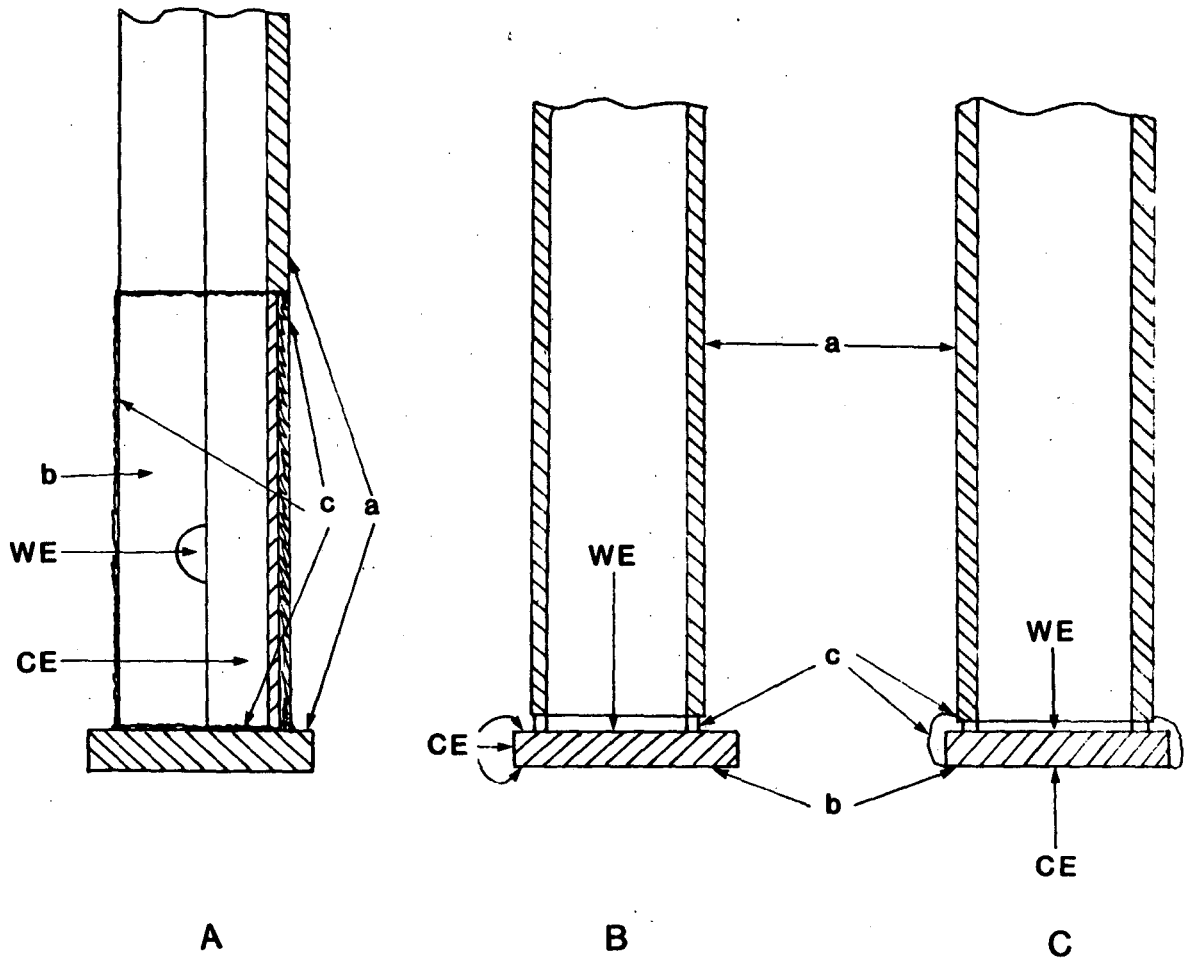

a Alpha Alumina
b Beta" Alumina
c Sealing Glass

CE Counter Electrode
WE Working Electrode

XBL 8411-4851

Fig. A.1

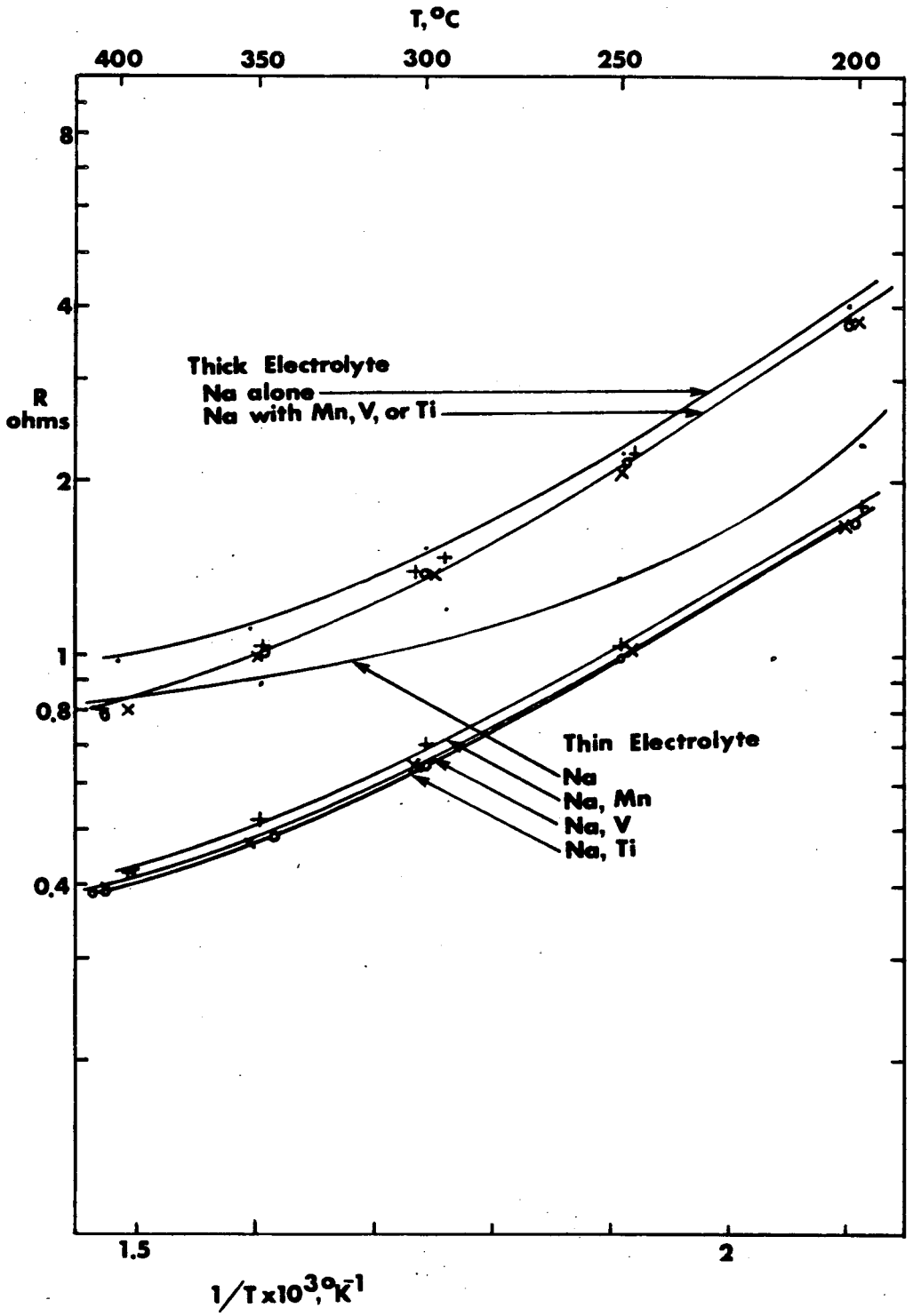

XBL 8411-4781

Fig. A.2

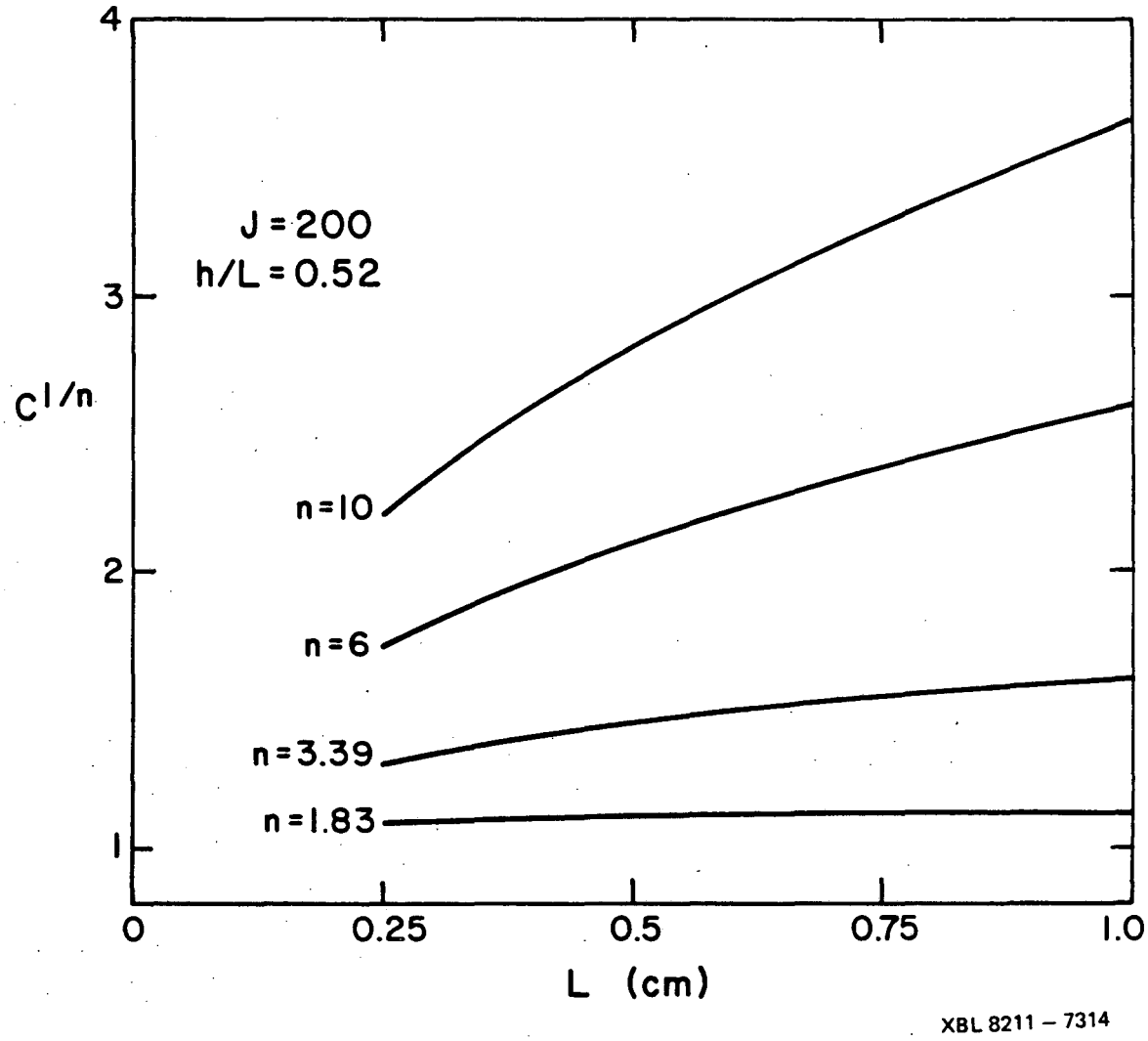
4
3
2
1
J = 200
h/L = 0.52
C 1/n
n=10
n=6
n=3.39
n=1.83
0
0.25
0.5
0.75
1.0
L (cm)
XBL 8211 – 7314

Fig. A.3

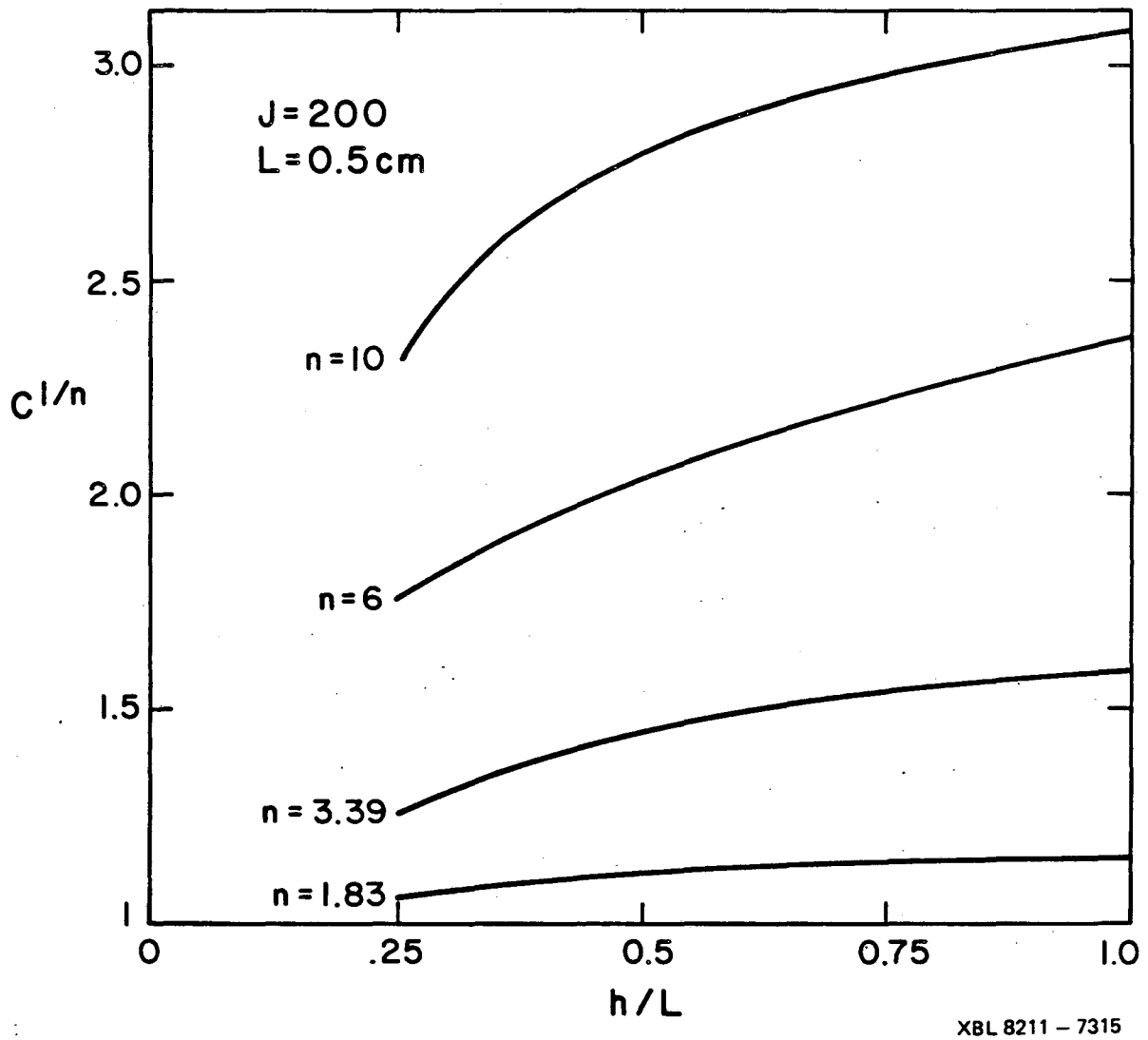
3.0
2.5
2.0
1.5
1
J=200
L=0.5cm
n=10
n=6
n=3.39
n=1.83
C^1/n
0
.25
0.5
0.75
1.0
h/L
XBL 8211 – 7315

Fig. A.4

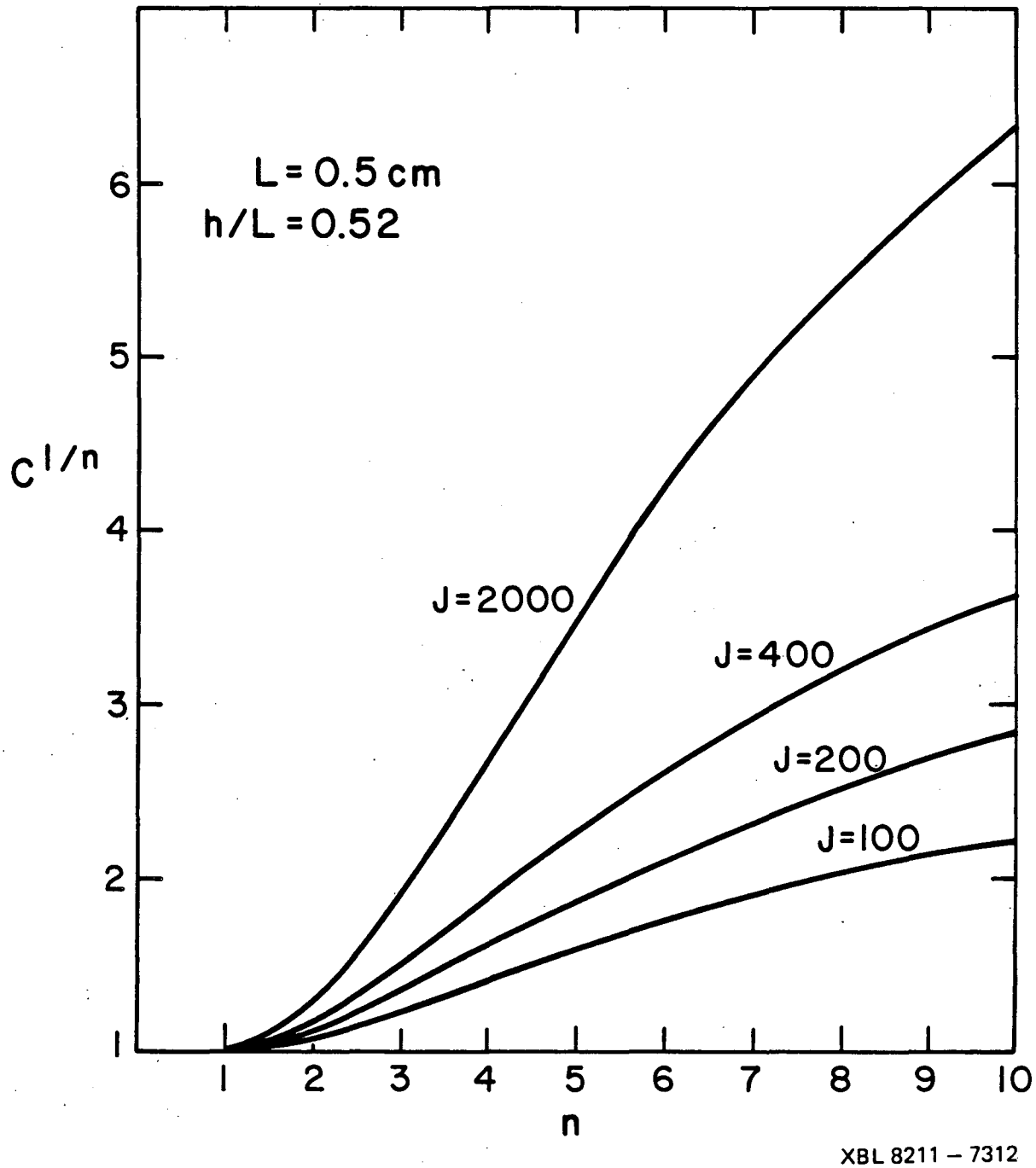
L = 0.5 cm
h/L = 0.52
J=2000
J=400
J=200
J=100
$C^{1/n}$
n
1
2
3
4
5
6
7
8
9
10
XBL 8211 – 7312

Fig. A.5

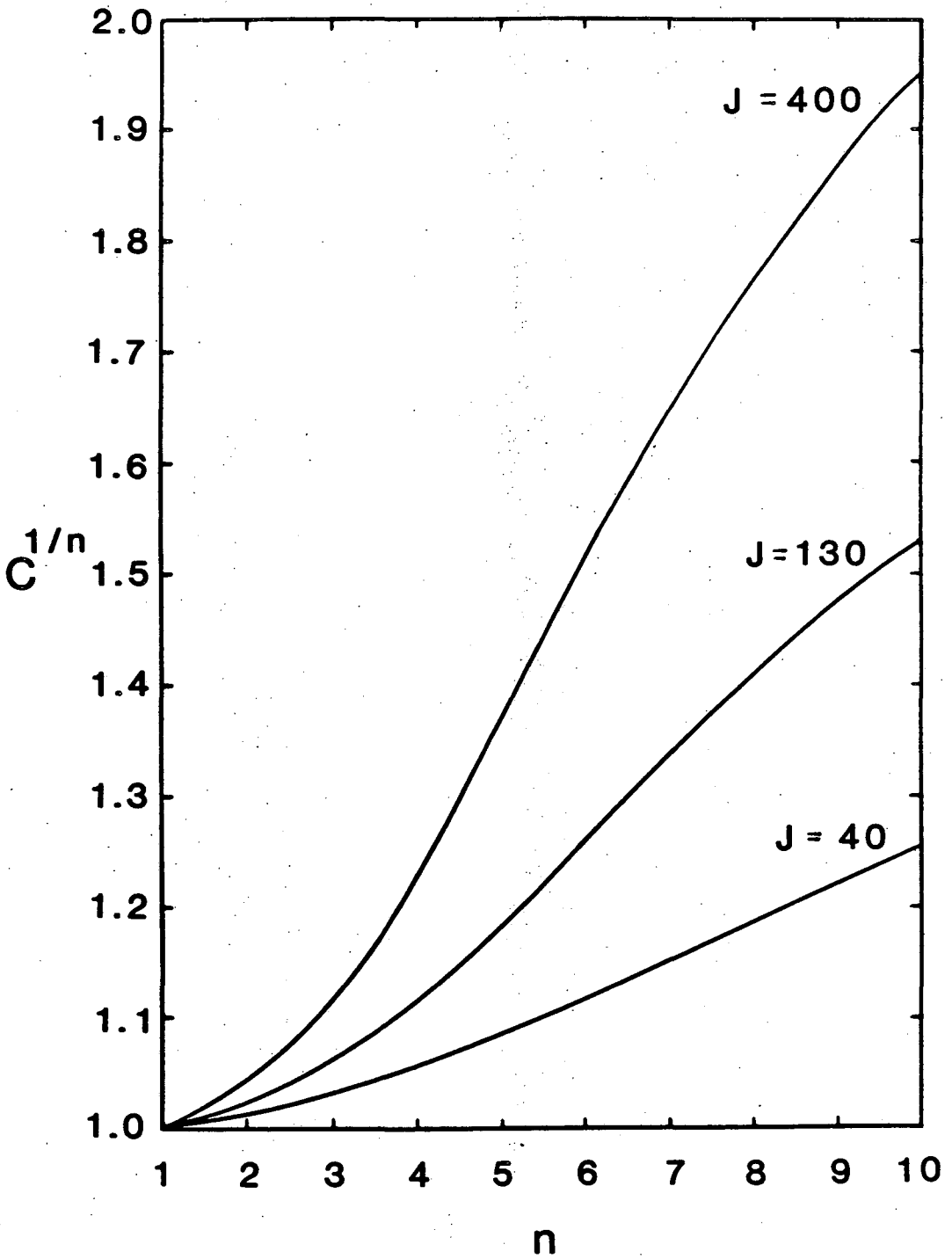

XBL 8411-4861

Fig. A.6

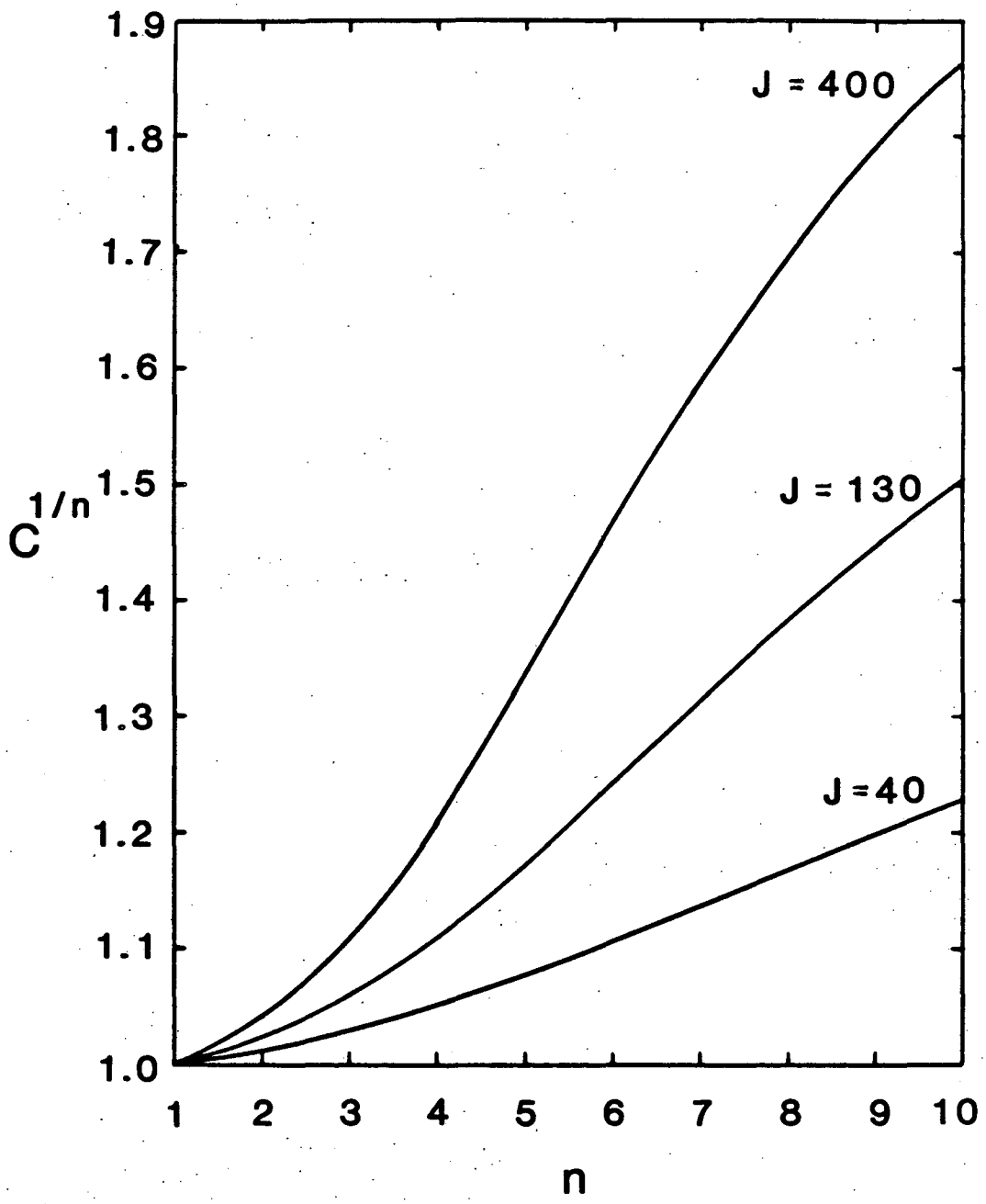

XBL 8411-4862

Fig. A.7

This report was done with support from the Department of Energy. Any conclusions or opinions expressed in this report represent solely those of the author(s) and not necessarily those of The Regents of the University of California, the Lawrence Berkeley Laboratory or the Department of Energy.

Reference to a company or product name does not imply approval or recommendation of the product by the University of California or the U.S. Department of Energy to the exclusion of others that may be suitable.

TECHNICAL INFORMATION DEPARTMENT
LAWRENCE BERKELEY LABORATORY
UNIVERSITY OF CALIFORNIA
BERKELEY, CALIFORNIA 94720